Tribological and morphological aspects of the femoro-tibial joint of weevils

Zur Erlangung des akademischen Grades einer

DOKTORIN DER INGENIEURWISSENSCHAFTEN (Dr.-Ing.)

von der KIT-Fakultät für
Maschinenbau
des Karlsruher Instituts für Technologie (KIT)

genehmigte

DISSERTATION

von

Dipl.-Ing. Cornelia Friederike Pichler Bsc.
geb. in Wien, Österreich

Tag der mündlichen Prüfung:	24.09.2025
Hauptreferent:	Prof. Dr. Hendrik Hölscher
Korreferent:	Prof. Dr. Christian Greiner
Vorsitzender der Prüfungskommission:	Prof. Dr. Veit Hagenmeyer

Abstract

With the rise of green energy a green lubricant is needed to comply with the global sustainability goals. I aim to find an environmentally beneficial solution to replace the outdated standards in the lubrication industry. In my quest to find an inspiration for this in living nature, the similarities between the joints of arthropods – especially insects – and the joints and bearings used in robotics and machines convinced me to not only focus on the lubrication inside these joints but to broaden my research aim to include the complete system. The openness of the joints in insects share the challenges that bearings and joints in technology experience as well, making them an intriguing research object to find inspiration for improved frictional systems. In this study, I examined the femoro-tibial joint of three beetle species (*Otiorhynchus sulcatus*, *Otiorhynchus salicicola* and *Coelorrhina aurata*). Beetles have been chosen as research focus because of their tight form closure around their joints due to their armored body. In order to obtain a deep insight into the complex system of the joints of these beetles, I used a multitude of methods. I focused on the lubricant found in their joints, its origin and its transport. Hence, I characterized the tribological properties of the lubricant and microstructures with the atomic force microscope and managed to obtain a first insight into the complex network supplying the lubricant with the help of novel methods like nanoCT complemented by FIB and synchrotron μCT. The lubricant of the small beetles *O. sulcatus* and *salicicola* evaporates quickly and leaves – if at all – sticky lubricant patches behind with an increased coefficient of friction, while the lubricant in *C. aurata* hardly changes with time. The majority of microstructures in the joints are aligned in an imbricate fashion forming sawtooth steps. Assuming frictional anisotropy for these asymmetric structures, an autonomous cleaning of the joints can be predicted, with the structures all leading outwards to expel possible contaminants. Here the lubricant might play an assisting roll, engulving sharp contaminants for a damage-free expulsion, while also being spread evenly on the frictional surfaces by the movement of the beetle. Utilizing the favorable geometry of the joints of *O. sulcatus*, I focus on those for the time-consuming tomography techniques. With the help of these measurements, I discovered that the lubricant supplying network hiding in the chitin-matrix beneath the frictional surface consists of two different types of canals: one narrow long continuous canal where the origin is unknown and one divided canal changing in diameter and originating in the haemocoel on the inside of the beetle being supplied by haemolymph. The canal supplying the lubricant, the purpose of the other canal, as well as the composition of the lubricant are not yet fully understood. The new findings in this work expand the limited knowledge existing in the field of joints in insects and aim to inspire new improved systems in technology. These should reduce the impact on the environment by reducing the energy lost to friction as well as reducing the pollinators used in existing systems by inspiring a new green lubricant. This work might guide biologists in examining more complex systems found in arthropods. Furthermore, it might encourage engineers to develop tribological systems inspired by nature.

Abstrakt

Mit dem Aufkommen grüner Energie entsteht der Bedarf an einem grünen Schmiermittel, um die globalen Nachhaltigkeitsziele zu erreichen. Mein Ziel ist es, eine umweltfreundliche Lösung zu finden, die die veralteten Standards in der Schmierstoffindustrie ersetzt. Auf der Suche nach einer Inspiration in der lebenden Natur haben mich die Ähnlichkeiten zwischen den Gelenken von Gliederfüßern – insbesondere Insekten – und den Gelenken und Lagern in der Robotik und in Maschinen davon überzeugt, mich nicht nur auf die Schmierung innerhalb dieser Gelenke zu konzentrieren, sondern mein Forschungsziel auf das gesamte System auszuweiten. Die Offenheit der Gelenke von Insekten teilt die Herausforderungen, denen auch Lager und Gelenke in der Technik ausgesetzt sind, was sie zu einem interessanten Forschungsobjekt macht, um Anregungen für verbesserte Reibungssysteme zu finden. In dieser Studie habe ich das Femorotibialgelenk von drei Käferarten (*Otiorhynchus sulcatus*, *Otiorhynchus salicicola* und *Coelorrhina aurata*) untersucht. Die Käfer wurden als Forschungsschwerpunkt ausgewählt, weil sie aufgrund ihres gepanzerten Körpers einen engen Formschluss um ihre Gelenke haben. Um einen tiefen Einblick in das komplexe System der Gelenke dieser Käfer zu erhalten, habe ich eine Vielzahl von Methoden angewandt. Ich konzentrierte mich auf den Schmierstoff in ihren Gelenken, seine Herkunft und seinen Transport. Daher habe ich die tribologischen Eigenschaften des Schmiermittels und der Mikrostrukturen mit dem Rasterkraftmikroskop charakterisiert und konnte mit Hilfe neuartiger Methoden wie nanoCT, ergänzt durch FIB und Synchrotron μCT, einen ersten Einblick in das komplexe Netzwerk, das das Gelenk mit Schmiermittel versorgt, gewinnen. Der Schmierstoff der kleinen Käfer *O. sulcatus* und *salicicola* verdunstet schnell und hinterlässt – wenn überhaupt – klebrige Schmierstoffflecken mit erhöhtem Reibungskoeffizienten, während sich der Schmierstoff bei *C. aurata* mit der Zeit kaum verändert. Die meisten Mikrostrukturen in den Gelenken sind schuppenförmig angeordnet und bilden Sägezahnstufen. Geht man von einer Reibungsanisotropie für diese asymmetrischen Strukturen aus, kann man eine autonome Reinigung der Gelenke vorhersagen. Dieser Prozess wird ermöglicht durch die Strukturen, die alle nach außen führen, um mögliche Verunreinigungen auszuscheiden. Dabei könnte der Schmierstoff eine unterstützende Rolle spielen, indem er scharfkantige Verunreinigungen einschließt, um sie schonend abzutransportieren, während das Schmiermittel gleichzeitig durch die Bewegung des Käfers gleichmäßig auf den Reibungsflächen verteilt wird. Unter Ausnutzung der günstigen Geometrie der Gelenke von *O. sulcatus* konzentriere ich mich auf diese für die zeitaufwendigen tomographischen Verfahren. Mit Hilfe dieser Messungen entdeckte ich, dass das in der Chitin-Matrix unter der Reibungsfläche verborgene Netzwerk zur Versorgung mit Schmiermittel aus zwei verschiedenen Arten von Kanälen besteht: einem schmalen, langen, durchgehenden Kanal, dessen Ursprung unbekannt ist, und einem geteilten Kanal, dessen Durchmesser sich ändert und der seinen Ursprung im Hämocoel im Inneren des Käfers hat und von der Hämolymphe versorgt wird. Der Kanal, der das Schmiermittel liefert, der Zweck des anderen Kanals sowie die Zusammensetzung

des Schmiermittels sind noch nicht vollständig geklärt. Die neuen Erkenntnisse in dieser Arbeit erweitern das begrenzte Wissen auf dem Gebiet der Gelenke bei Insekten und zielen darauf ab, neue verbesserte Systeme zu inspirieren. Diese sollten die Auswirkungen auf die Umwelt verringern, indem sie die durch Reibung verlorene Energie reduzieren und die Umweltverschmutzer, die in den bestehenden Systemen eingesetzt werden, durch die Entwicklung eines neuen grünen Schmiermittels verringern. Diese Arbeit soll Biologen bei der Untersuchung komplexerer Systeme, wie sie bei Gliederfüßern vorkommen, anleiten. Außerdem soll sie Ingenieure dazu inspirieren, tribologische Systeme nach dem Vorbild der Natur zu entwickeln.

I would like to dedicate this work to the 53 beetles I had to sacrifice to make this thesis possible.

Contents

1 Introduction

Climate change is a topic, which cannot be ignored. In just the amount of time it took me to complete this thesis, the temperature increases constantly – with 2024 finally cracking the 1.5° C mark [1] [2] – , drastic climate events happen more frequently, with major floods, droughts, forest fires of entire cities burning down, snow storms, cyclones, typhoons etc. Even if you have not been directly affected by any of those catastrophes, you still might have observed hotter summers, missing snow in the winter, less bird sightings but unusual amounts of birds not flying into the warmer climates over the winter or returning earlier, with similar observations for insects. As scientists it is our goal and responsibility to find solutions for problems of humankind. With climate change and our linked demise being the most pressing matters, it is our duty to use our capacities – at least in part – for the research of fighting climate change. Of course there is not one clear culprit for climate change and therefore not one clear field of research responsible to find a solution, therefore we all have to work together with interdisciplinary collaboration being the key for a successful conservation of our world as we know and love it.

I picked the field of tribology as my contribution for a small step towards a green future needed to fight climate change. Tribology is dominated by two opposite shortcomings, the failure to move without resistance and the failure to resist without movement, both leading to unwanted energy loss. Friction being the evil of both, can lead to heat buildup and wear additionally damaging the moving surfaces in contact. The common solution to minimize the energy loss of the hard earned energy in moving machinery is the use of lubricants [3] [4]. Unfortunately, the commonly used lubricants are still based on fossil resources, hindering the development of sustainable alternatives to successfully fight climate change [5] [6] [7]. The extent of the energy loss due to friction becomes apparent in a study from 2017 by Holmberg and Erdemir [8]. According to their calculations friction alone constitutes to 20 % of the global energy consumption, while related wear and the subsequent reproduction of damaged parts adds additional 3 %. One crucial part in the fight of climate change is the reduction of CO_2, which could be achieved according to Holmbergs and Erdemirs predictions by the implication of advanced tribological technologies leading to the reduction of 3,140 Mt CO_2 of global emissions in the long term. The advanced tribological technologies include green lubrication on which I focus in this study.

As a great starting point for a new green invention it is worthwhile to take a closer look into living nature [9] [10]. The inspiration for tribological advancements in nature is numerous with a wide spread of geometries, environments and specific cases tailored to every engineers needs. The first incline of a mechanical engineer tasked with the goal to reduce friction, would be to search for the system with the lowest coefficient of friction (COF). In nature, this system would be the synovial joint found in mammals with an unrivaled COF being reported to be as low as 0.002 [11] [12] [13]. Unfortunately, a closer look reveals, that this system is hard to be transferred in technological systems, due to its sheltered and

closed nature. The synovial joint is a pressurized complex system being separate from the environment. Most technological joints and bearings do not allow for such a difficult and intricate setup. Therefore, a deeper dive into nature is needed to find a suitable inspiration.

Despite the enormous number of 5.5 million estimated different species in the group of insects [14], they are often overlooked in biomimetics. Nevertheless, the similarity of insects' joints and mechanical joints and bearings is enticing. The use of an exoskeleton and its advantages forfeits the use of a closed system for moving parts. This means the joints of insects are open to the environment, similar to their technological counterparts. The soiling of joints and bearings as well as lubricant loss is a challenge to both, with lubricant loss of fossil-based lubricant in technology being another risk and challenge to the environment in turn. The lubricant loss causes the need for constant resupply of the substance to reduce the friction of the system, while particles entering the system can lead to destruction of the system. The morphology of insects' joints is supposedly as diverse as the group of insects themselves with simple systems like hinge-joints [15] but also curious geometries like cog-wheels in nymphs of froghoppers [16] and screw and nut systems in weevils [17]. Insects also feature a wide margin of tasks for different joints from jumping to flying. All of these similarities and opportunities make insects' joints ideal models for technological joints and bearings. Nonetheless, the analysis of systems of insects is challenging due to the reduced size, while also opening up the possibility to use an unconventional methodological approach. This leaves me with the difficult task to pick my research subject out of the numerous group of insects with the choices being endless and finding appropriate methods can pose a challenge.

Beetles showcase a compact structural shape not leaving much wiggling room. Being intrigued by the unique design of the screw and nut system of the weevils, I opted for these as my main research focus, with an additional rose beetle as a mode of comparison to older studies [18] [19]. Many weevils showcase the compact shape of the beetles I strive for, featuring heavily sclerotized exoskeletons and tight form closures increasing my hope to find lubricant [20].

After first being mentioned in 2001 (page 90 in [9]), lubricant in the joints of insects has experienced a resurgence in 2021, with eight studies published in just four years. Nadein *et al.* published their first study in 2021 describing the lubricant found in the joints of *Zophobas morio* [18]. The study includes scanning electron microscopy (SEM) images of the lubricant, a rudimentary analysis of the lubricant, a first tribological measurement of the COF of the lubricant and a hypothesized mode of operation of the semi-solid lubricant acting as a rolling bearing. A subsequent study adds eight different insect species hosting lubricant in their pores to *Z. morio* [21]. Further studies research the tribological properties of insects' joints [19], wear inside the joints of beetles [22] and cleaning of the joints

[23]. In addition the behavior of the lubricant has been simulated in three numerical studies [24] [25] [26] with mixed results. A detailed review of the studies mentioned here can be found in Section 2.2.

In this thesis, mainly a simple joint system of one beetle shall be described. The weevil *Otiorhynchus sulcatus* is joined in some sections by two other beetles *Otiorhynchus salicicola* and *Coelorrhina aurata*. With these beetles' joints being formerly undescribed concerning the lubricant, the first order of operation was the need to locate the lubricant, if there is one. Therefore the first study conducted on all beetles was an inspection with the SEM to discover the lubricant and its behavior. After this successful study the tribological behavior of the two different lubricants of *O. sulcatus* and *C. aurata* was characterized with the atomic force microscope (AFM) allowing for friction force measurements (FFM) in silicone oil to preserve the natural state of the samples and allow for comparable measurement environments and conditions. During these measurements, structures of the frictional surfaces have been discovered. The microstructures of *O. sulcatus* have been researched with FFM and synchrotron micro-computed tomography (μCT) discovering a frictional anisotropy leading to particle transport and therefore cleaning of the joints. One of the structures discovered in the measurements are the pores supplying the lubricant to the frictional surface. With the help of μCT, nano-computed tomography (nanoCT) and focused ion beam (FIB) tomography the network of pore canals below the frictional surface has been depicted for the first time. Last but not least an analysis of the lubricant found in *O. salicicola* has been strived for, comparing it to the sucessfully analyzed haemolymph traversing the beetle.

2 Theoretical background

2.1 Tribology and tribological methodology

Despite the fact, that friction is one of the most common forces in technology, it is not well understood. With adhesion and superlubricity existing, the span for tribology is quite complex. In contrast to other forces, we have to decide from situation to situation if we want to increase the friction or minimize it. The cases of both extremes often occur in close proximity, e.g. a tire, moving with as little friction as possible around an axle to preserve energy and reduce heat, would not fulfill its purpose if the friction between the tire and the ground would be minimized as well. With the human aspiration for smaller machines in MEMS/NEMS and technology in general, the energy losses and heat build-ups attributed to friction become a serious problem and increase on a manifold compared to the difficulties encountered in macroscopic machines [3] [9] [27] [28] [29] [30].

The basics for unlubricated friction are divided into three sub-frictions: static friction, kinetic friction and rolling friction. Static friction has to be overcome to get a body at rest moving, kinetic friction has to be overcome to keep a moving body moving and rolling friction has to be overcome to roll a body. Usually friction decreases from static friction to kinetic friction and again from kinetic friction to rolling friction [3] [28] [31].

Lubricated contacts experiencing friction can also be divided into three sub-sections depending on the distance between the two surfaces corresponding to the lubricant film thickness. The Stribeck-curve of the COF or friction force over the combined lubricant properties, which is the ratio of velocity and viscosity over the load can be seen in Figure 2.1. It can be divided in three different regimes. Regime I. is the boundary lubrication regime with molecular levels of lubrication and the contacts having a minimal distance between them, leading to wear and deformation of the surfaces, which increases the COF. Regime II. is the mixed lubrication regime increasing the lubricant film between the two surfaces without removing contact between the two surfaces entirely. This leads to a mixing of the worn off particles from the contact between the surfaces and the lubricant, hence the name. Regime III. is the last regime of full film lubrication preventing contact between the two surfaces with a thick film of lubricant between the two surfaces [4] [28] [29] [32].

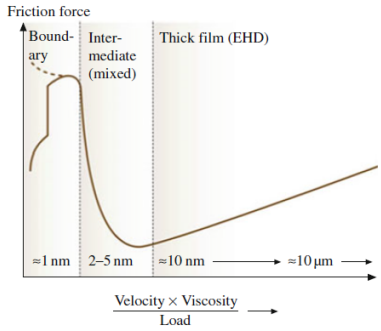

Figure 2.1: Stribeck-curve explaining the friction force in relation to the specific film thickness of the lubricant between two surfaces. The curve can be divided in three regimes: I. Boundary lubrication II. Mixed lubrication III. Full film lubrication. Image adapted from [30]

The atomic force microscope (AFM) is a versatile instrument for structure analysis in the micro and nano-range. It is one of the most used techniques in the family of scanning probe microscopy. The probe, which is known as cantilever, has many different shapes as well as tip geometries. The most used cantilever type is rectangular with a sharp tip. By glueing a glass sphere to a rectangular tipless cantilever one can obtain a colloidal probe with known radius. The glueing can be done with a pulled capillary and a micromanipulator or the AFM directly. This results in a bigger contact area between the probe and the surface [3] [9] [33] [34] [35] [36].

In most instruments, the movement of the cantilever is tracked with the help of a laser. The laser's light is reflected off the flat base directly above the tip and onto a four-quadrant photodiode (see Fig. 2.2). The position of the reflected laser spot on the four-quadrant photodiode allows for a measurement of the bending and torsion of the cantilever [3] [9] [33] [34] [35] [36].

The AFM has two different modes: the tapping mode and the contact mode. In tapping mode, the cantilever oscillates near its resonance frequency above the surface and only taps the surface. The distance between the cantilever and the surface is kept constant by the piezo scanner, which reacts to the amplitude decrease caused by the forces between the sample and the tip. The change of the piezo scanner is recorded and provides an image of the surface topography. The tapping mode can also give insight into the material properties, like adhesion or elasticity with the help of phase imaging, which records the phase shift triggered by a different tip-sample interaction. In the contact mode the tip of the cantilever is – as the name suggests – in direct contact with the surface. Here the applied force is monitored and kept constant via the piezo scanner controlling and recording the cantilever-sample distance [9] [33] [34] [35] [36].

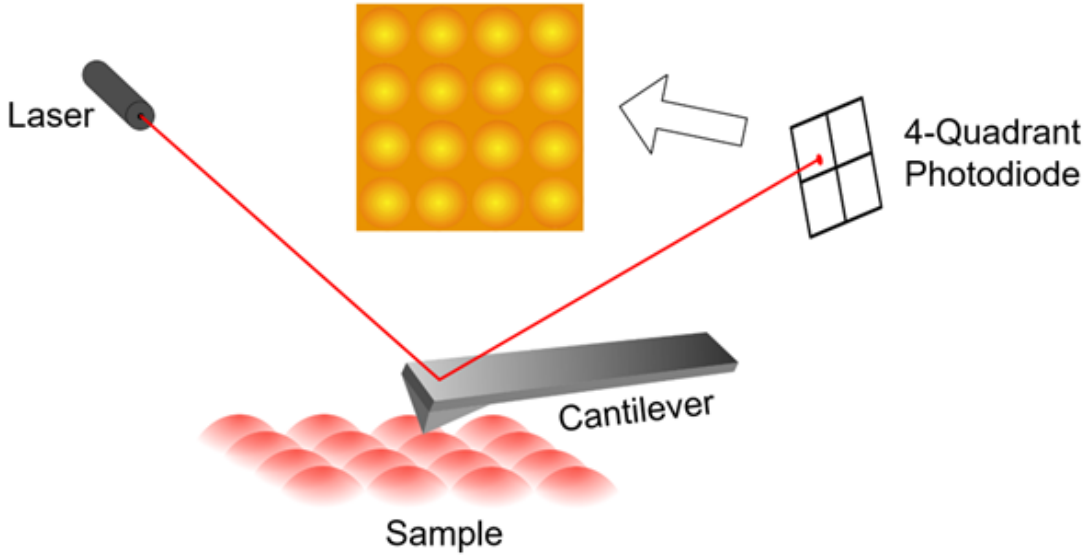

Figure 2.2: Sketch of the mode of operation of the atomic force microscope (AFM). The cantilever scans over the surface following the topography closely with the tip of the cantilever. The movement of the tip and cantilever is tracked with a laser reflected from the cantilever onto a four-quadrant photodiode, leading to a depiction of the surface.

Friction force microscopy or (FFM) is an alteration of the contact mode. Instead of scanning the surface parallel to the cantilever long axis, you scan the surface normal to the cantilever long axis, which leads to a torsional movement of the cantilever additionally to the bending as a result of the height. This torsional movement is connected to the friction between the surface and the cantilever tip. The higher the COF of the surface the higher the torsional movement. This movement is recorded in volts and can be transformed to a force in newton by calibrating the system [9] [27] [30] [33] [34] [35] [36].

During friction measurements both the trace as well as the retrace is recorded in a so-called friction-loop. The difference of trace and retrace is proportional to $2\mu F_{load}$. With μ being the conventional COF and F_{load} the applied loading force [33] [34].

Figure 2.3 shows an exemplary theoretical curve as it can be recorded with an AFM. The start of the curve to the left shows a linear increase in the frictional force in the trace (movement over the sample from left to right) before reaching a constant level. This occurs again mirrored on the end of the curve for the retrace, where the cantilever changes direction. This increase and higher force is the cantilever overcoming the static friction of its contact with the sample. The constant force following this increase is the kinetic friction of the cantilever moving in a constant motion over the sample. The friction force recorded in the AFM comes from the tilting of the cantilever upon friction between the cantilever tip and sample. This means the cantilever tilts from its relaxed original position to a specific

angle measured with the four-quadrant photodiode until the static friction is overcome and the tip starts moving over the surface in a constant motion keeping the angle corresponding to the kinetic friction between the tip and the sample.[1]

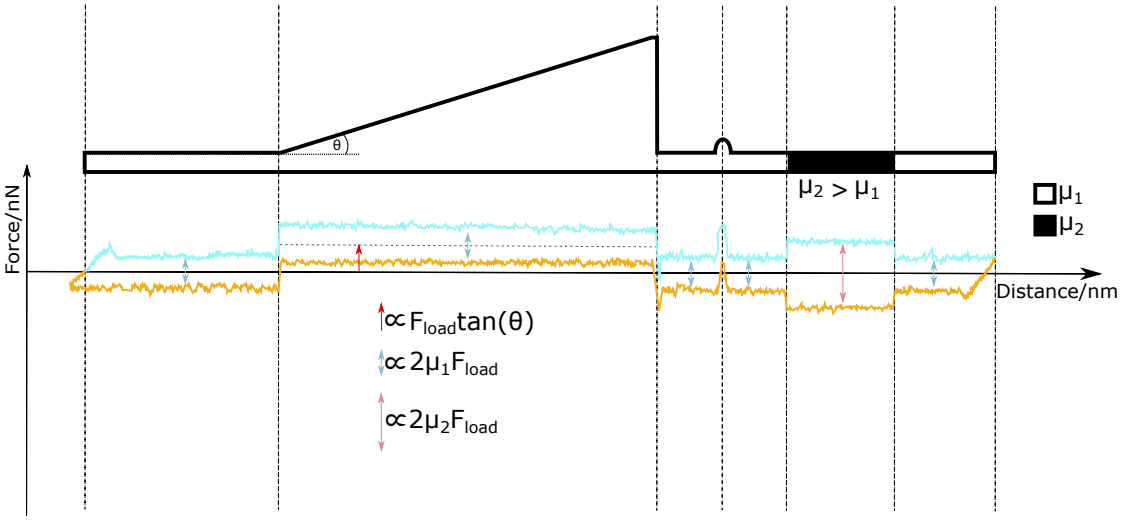

Figure 2.3: Theoretical friction-loop for the surface depicted at the top of the schematics. The blue line is the trace recorded while moving the cantilever from the left to the right and retrace in orange is recorded in the other direction. Due to the switch of the tilt of the cantilever, trace and retrace switch sign. The trace starts with overcoming the static friction before the tip moves with a constant angle over the surface. At the sloped surface with an angle of θ of identical material the trace and retrace experience a shift in the same direction proportional to $tan(\theta)F_{load}$, while the difference of trace and retrace stays the same as from the flat surface proportional to $2\mu_1 F_{load}$. A similar shift happens at the little protrusion in the surface leading to a spike in trace and retrace. At the encounter of a different material without a change in topography, following still a flat surface, the difference between trace and retrace increases according to the increase of the coefficient of friction, when $\mu_2 > \mu_1$. At the switch from trace to retrace the cantilever needs to change direction and therefore decreases the angle before needing to overcome the static friction again, repeating the journey of the trace in reverse order and angle.

Important to consider during the friction measurements is the influence of the topography. If the cantilever encounters a wedge with angle θ, the friction measurements shift proportional to $tan(\theta)$. Small bumps in the surface result in a spike in the same direction of both trace and retrace, while a higher COF results in an expansion of the difference be-

[1] For readers requiring a visual and audible explanation of the FFM for a complete understanding, I recommend the comprehensive guide, which can be found on YouTube (https://www.youtube.com/watch?v=n-ZFfQwecSg).

tween trace and retrace. Therefore to minimize possible topography crosstalk in the friction measurements, one can subtract the trace from the retrace. At the beginning of trace and retrace the cantilever has to overcome the static friction. This phenomena is visible in a linear rise, before the kinetic friction takes over and is most of the times excluded from the friction analysis [30].

Wear is an important topic in tribology, but incredibly hard to quantify [3] [28]. However, it is of no immediate interest for this thesis and will be skipped. It is controversial how the material roughness plays the primary roll for friction and I therefore will not enforce this concept [3] [28]. A discussion would go beyond the scope of this thesis.

Tribology has been mastered in many different aspects in nature. The synovial joint in humans is unrivaled in its low COF, snakes and sandfish use frictional anisotropy for an effective movement without legs and on or in difficult terrain next to the reduction of wear and abrasive particles, pitcher plants use a slippery lubricant infused surface to catch and trap their prey, while insects use fluids and specialized structures on their feet to enable walking upside down even on polished surfaces [9] [27]. These inspirations from nature can advance and enforce the development of green lubricants, because the development of such has been quite slow and tenacious [9] [32] [37].

2.2 Short introduction to entomology

2.2.1 Review of previous studies on lubricants found in insects

This chapter summarizes the so-far limited research on the lubricated system of insect's joints, highlighting important discoveries and missing stepping stones for a comprehensive description of the full system.

The existence of lubricant and pores supplying lubricant in the joints of insects was first mentioned in 2001 and 2019 in two different books [9] [38]. Unfortunately, there was no further information or references given supporting this claim. Another study [39] on the tribology of jumping insects make the assumption of additional lubricating lipids on the frictional surface of microstructured joints of katydids. Nevertheless the study itself focuses mostly on the tribometer measurements of the joint partners and the absent wear, attributed to the microstructures and complimenting hardness of the joint partners. The first study exploring the concept of an actual lubricant in the joints of insects in 2021 [18] was joined shortly after by a successive study [21]. The first study focuses on the darkling beetle *Zophobas morio*. It presents the found lubricant, hypothesizes the mode of operation of the lubricant and does a rudimentary analysis of the components. The lubricant can be found extruding from pores in the joints of the beetle. Under the Cryo-SEM, the lubricant forms cylindrical accumulations, so that Nadein and his colleagues hypothesized that these cylinders separate the two frictional surfaces as a kind of roller bearing. The semi-solid cylindrical accumulations are protein-based, which was found with an attenuated total reflection

Fourier transform infrared spectroscopy (ATR-FTIR) system. Tribometer measurements show a COF of the lubricant of 0.13, which is comparable to the COF of Teflon in the performed measurements. These tribometer measurements have been complemented by a subsequent study [19] adding another beetle species, *Pachnoda marginata* and detailed tribometer measurements. For this subsequent study, the interest lies more in the tribological properties of the joint system than the lubricant itself. Next to the complete hinge-joint system, parts of it were examined as well as easily accessible surfaces like elytra and abdomen, which are of no significance in this work and are therefore not discussed. The complex system of the femoro-tibial joint showed very low COF of 0.00474 ± 0.00007 (*Z. morio*) and 0.1055 ± 0.0011 (*P. marginata*) in the tribometer measurements, where the joint was attached without change of the natural system. The tribological systems femoral condyle/glass (*Z. morio*: 0.0167 ± 0.007; *P. marginata*: 0.0215 ± 0.007) and tibial condyle/glass (*Z. morio*: n.a.; *P. marginata*: 0.0229 ± 0.010) were measured after opening and dislocation of the joint. The low COF of the complete system is attributed to the lubricant presumably inhabiting the system and reducing the COF due to the rolling bearing nature.

The second study [21] presents lubricant in different insects with the help of an SEM. A species of interest for this thesis is only mentioned in the supplemental material with a single picture: the femur of the femoro-tibial joint of a weevil showing pores and a thin lubricant trace.

A study [22] focusing on wear in the joints of beetles claims a new function of the lubricant. Lubricant presumably clumps together with sharp particles, engulfing the same to protect the frictional cuticle surface from wear. The study presents different wear traces as seen with the SEM in the joint of beetles for different substrates and different life times. For a control of unworn surfaces, they are preventing movement of the beetles.

Taking the wear idea to the next level, a study [23] was published, exploring the self-cleaning abilities of the joints of beetles. The study is using a μCT system to follow the path of a metallic powder distributed on a fresh joint of a beetle. The movement of the leg is transporting the particles out of the joint and prevents particles to enter the joint with hairs and bristles. A small portion is focusing on a special bristle like microstructure transporting particles out of the joint and preventing a backflow of particles.

Filippov *et al.* studied the concept of the lubricating properties and functionality with numerous numerical studies all published in the year 2024. The first study [24] still shows the firm conviction, that the semi-solid lubricant forms into cylinders and cylindrical fragments to act as a rolling bearing between opposing surfaces. The second and third study [25] [26] acknowledges the clumping together of the lubricant fragments facilitating the distribution of the lubricant in combination with the help of grooved microstructures and the transport and engulfing of wear-inducing particles with the lubricant.

As of now, the field of research of the tribological systems in arthropods is in its infancy and only has an incomplete description of the system and the separate parts. The complete and deeper understanding of the interconnected system is still missing, which this thesis is aiming to expand.

2.2.2 Description of the basic anatomy and nomenclature of a single leg as found commonly in beetles

As a visual aid for the reader, a depiction of a beetle leg (Fig. 2.4) including the scientific labels for the different parts is included here. For better understanding of the location of the scientific labels, the composition of the beetle's leg is set in relation to the widely comprehensive names in a human leg or arm. The image used in Figure 2.4 is a 3D-reconstruction of the surface of the segmentations of the different parts of the legs, segmented from a lower resolution μCT scan. The different parts have been colored and the image has been rendered with blender. All methods used to obtain this image are described in their respective section in Section 3.

In its simplest form, the leg of a beetle is comprised by five parts leading to four connections and therefore joints in the leg itself and an additional connection and joint between the leg and the body of the beetle. The part of the leg in contact with the ground is the tarsus, here shown in blue, which might be compared to a human foot or hand, consisting of many parts not further explained here. It is connected to the tibia, which is depicted in red, which might be compared to the shin or forearm. The joint connecting the tibia to the femur is the femoro-tibial joint, comparable to a knee or an elbow and the focus of this thesis. The femur is shown in green and is comparable to the upper arm or thigh. The trochanter in yellow is the link between the femur and the connection to the beetles body, the coxa in pink. The coxa-trochanteral joint linking the trochanter to the coxa can be compared to a human hip or shoulder. For weevils this joint has a very special morphology reminiscent of a screw and nut system [17] being further explained later in this thesis.

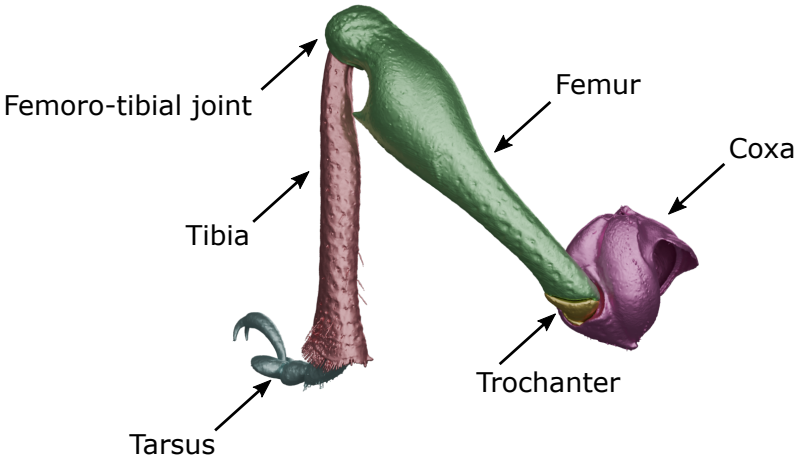

Figure 2.4: The five different parts of a beetle leg. At the end of the leg is the foot of the beetle colored in blue called tarsus. The part connecting to the tarsus is the tibia colored in red. Over the femoro-tibial joint the tibia is connected to the femur colored in green. The trochanter colored in yellow is the link between the femur and the coxa colored in pink, which is the part of the leg connecting it to the body of the beetle. The femoro-tibial joint is the focus of this thesis. For this image the 3D-representation of a lower resolution μCT scan of the beetle *O. sulcatus* was used. The different parts of the leg were segmented and colored and rendered with blender. Details to this process can be found in Sections 3.5 and 3.8.

3 Materials and methods

3.1 Examined beetles

For this work the order of beetles (*Coleoptera*) was chosen, due to their compact and armored design, which results from their limited speed and maneuverability. Without the ability to jump and the cumbersome flight – if at all – beetles have to sustain higher pressure by sturdier design. This leads to a reduced mobility in the joints, less air cushioning and increased contact surfaces, leading naturally to higher friction. This makes the group of beetles a promising candidate for lubricant in their joints to reduce friction.

Three different kind of beetles were cultivated for this project. The green metallic rose beetle *Coelorrhina aurata* (Fig. 3.1 a)) is native to the African continent but is wildly kept in captivity for their easy breeding and striking colors. The beetle spends most of its life in the larval state with a generation time of five to seven months. The beetle was chosen for the comparability to the studies preceding this work described in Section 2.2. Four living imagines (adult beetles) (two males, two females) were purchased from thePetCompany (thepetcompany.com, Germany) and bred for one generation resulting in five further imagines (four males, one female). So in total nine imagines of *C. aurata* were used in this thesis. The beetles were kept in a terrarium of 5.5 l on a mixture of Beetlefix 1 & 2 and fed with beetle jellies (all purchased from thePetCompany).

The black vine weevil *Otiorhynchus sulcatus* (Fig. 3.1 b)) is a pest common in Germany and Central Europe, where they infest many different host plants. The imagines only damage the leaves of the host plant, while the larva damage the roots of the plants, which can lead to decay. The imagines can live up to three years and hibernate in the earth during winter. The beetles used in this study were found on the host plants hops (*Humulus*) and cabbage (*Brassica*) (22 imagines collected in Karlsruhe in August 2022, June 2023 and June 2024). They were kept in a terrarium of 25 l on cocos substrate and fed with their hostplants, additionally to leaves of the small leaved linden (*Tillia parvifolia*) and silver-inch plant (*Tradescantia zebrina*).

A second weevil *Otiorhynchus salicicola* (Fig. 3.1 c)) was found on cherry laurel (*Prunus laurocerasus*) (22 imagines collected in Linkenheim in April and May 2024) and kept in a terrarium of 25 l on cocos substrate and fed with their hostplants. Looking similar to the black vine weevil, these differ in size as well as slight differences in the geometry of the joint.

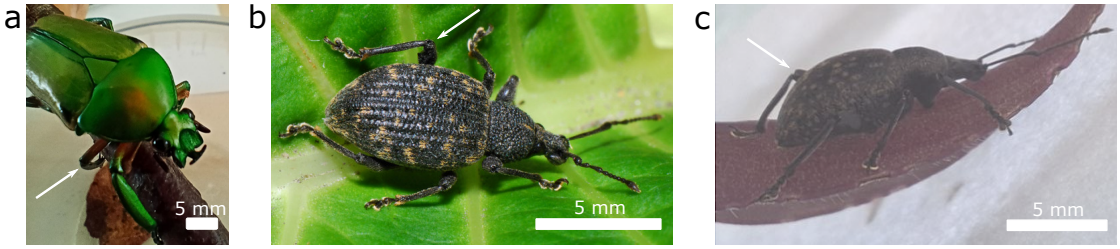

Figure 3.1: The beetles examined in this thesis: (a) Green metallic rose beetle *Coelorrhina aurata* (b) black vine weevil *Otiorhynchus sulcatus* (c) another weevil *Otiorhynchus salicicola*. The white arrows point exemplary to one of the femoro-tibial joint analysed in this thesis.

The joints of *C. aurata* and *O. sulcatus* were analysed by friction force measurements to compare the COF evolution of the lubricant during air-drying. *C. aurata* was chosen to enable a comparison with previous studies. The weevils were originally chosen because of their unique geometry of the coxa-trochanteral joint, which is formed like a technical system consisting of a screw and a nut. Unfortunately, the convex geometry of the screw is impeding the AFM measurements leading to an incomplete picture of the frictional properties, while the nut-geometry makes AFM measurements entirely impossible. During the research on the other leg joints, the very fortunate geometry of the femoro-tibial joint was discovered. This opens up many possibilities, which are not possible with the rose beetle and its complicated geometries. The research on the lubricant extruding pores, was therefore conducted on the weevils *O. sulcatus* and *O. salicicola*.

Microstructures researched and described in a latter chapter can be found in different variations in all the researched beetles. Nevertheless I focus on the microstructures found in the joints of *O. sulcatus*, supplying me with the largest amount of data obtained with different methods.

The beetles for the friction force measurements died of natural causes before being rushed to the lab for analysis or stored in a closed container until needed. The beetles used for the measurements of the pore channels, haemolymph analysis, and lubricant evaporation measurements were anesthetized with CO_2 before further preparation. The further preparation changed depending on the method and is described in each method chapter respectively.

3.2 3D-printing in nanoscale

Biological systems are not always easy to measure, due to their difficult geometries. Some of the examined microstructures are found on convex and concave surfaces, influencing the friction force measurements in an unexpected way and complicating the interpretation of the results. In order to isolate the tribological properties of the microstructures from the

underlying geometries, a method was needed to replicate the microstructures on a flat surface with submicrometer resolution. This was accomplished with a microfabrication system based on two-photon-polymerization.

The microstructures were designed with the software Fusion 360 (AutoDesk, USA) as closely as possible to the structures found in the beetles and slightly changed for some comparable measurements and evolution testing. The microstructured samples were printed with the kind support of Stefan Hengsbach (KIT) und Celine Deutschbein (KIT) utilizing a 3D direct laser writing system 3D-DLW Photonic Professional PPGT2 (Nanoscribe GmbH, Germany) using IP-Dip resin (Nanoscribe GmbH, Germany).

3.3 Scanning electron microscopy

The well established method to observe the surface topography is the scanning electron microscope (SEM). This method is very useful for quality control and a quick overview of geometries and surfaces in sub-micron resolution, while also being virtually destructionfree. Samples examined by the SEM have to fulfill certain criteria or have to be prepared accordingly. Due to the use of electrons, samples have to be stable in vacuum and isolators, like biological samples, have to be coated in a thin metallic layer to avoid charging effects [40].

In this thesis the SEM system SUPRA V60 (Zeiss, Germany) was used at 3 keV to prevent excessive damage to the sample, while still obtaining images with sufficient detail. The working distance varied depending on the samples. Flat samples like the test structures printed with the Nanoscribe system as well as *O. sulcatus* and *O. salicicola* samples had a working distance between 3 mm and 6 mm, while tilted samples and *C. aurata* samples needed a bigger working distance of up to 15 mm to prevent any accidental contact between the samples and the SEM electronics. In order to perform SEM measurements on nonconducting samples, which include all samples in this thesis, a thin conducting layer of silver was added. For the biological samples the layer was limited to around 7 nm, while the 3D-printed test structure samples were covered in a thicker layer of around 20 nm. The reason for the drastic difference between biological samples and the 3D-printed test structure samples lies in the size of the features we can expect on the samples. For the the 3D-printed test structure samples, the fabrication method limits the details we can expect and we can therefore apply a thicker layer of silver without risking the disappearance of details in the silver layer. The biological samples show features in the nanometer scale and therefore the need for a thinner silver layer arises. Due to the lack of a cryo stage at my institute, the thin silver layer on the fresh beetle samples serves another purpose. My hope is to stop or at least slow down the evaporation process of the sample for the duration of the SEM measurements in order to obtain images of the fresh lubricant without a cryo stage.

3.4 Atomic force microscopy

The many benefits of an atomic force microscope (AFM) have been highlighted above in Section 2.1. The versatile tool allowed for a detailed insight of tribological properties of both lubricant and microstructures of the examined biological systems, while providing insight at the same time in the topography of the system. The wide variety of measurement modes as well as the ability to perform measurements both in liquid and in air has been fully utilized in this thesis.

The AFM systems used in this thesis were a Dimension Icon (Bruker Cooperation, USA) and a FlexFM (NanoSurf, Switzerland). Two devices of the first one were used in different labs with one of them located in a clean room with controlled temperature and humidity. The Dimension Icon was used for the beetle joint measurements, while the FlexFM was used for the the 3D-printed test structure samples (see Sec. 3.2). The probes used in this thesis were All-in-One-Al Cantilevers B and C type (spring constants of 2.7 N/m and 7.4 N/m, respectively) with a sharp tip (BudgetSensors, Bulgaria). For the measurements with colloidal probes a All-in-One Tipless Cantilever B was functionalized by attaching a glass sphere with a diameter of around 20 μm with two component glue (Plus Endfest, Uhu, Germany). Before each measurement session and between measurements the cantilever's deflection error sensitivity was tested on a hard surface (sapphire or glass) and the force constant deduced with thermal tune.

The measurements to obtain the COF for different drying stages of the beetle joints require an intricate setup. To prevent the lubricant and biological samples to evaporate and undergo possible physical change during the measurements, these were conducted with samples submerged in silicone oil as shown in Figure 3.2. The measurements of the samples in silicone oil were made possible with a special cantilever holder, dedicated to measurements in fluids keeping the electrical parts of the AFM safe from contact with fluids.

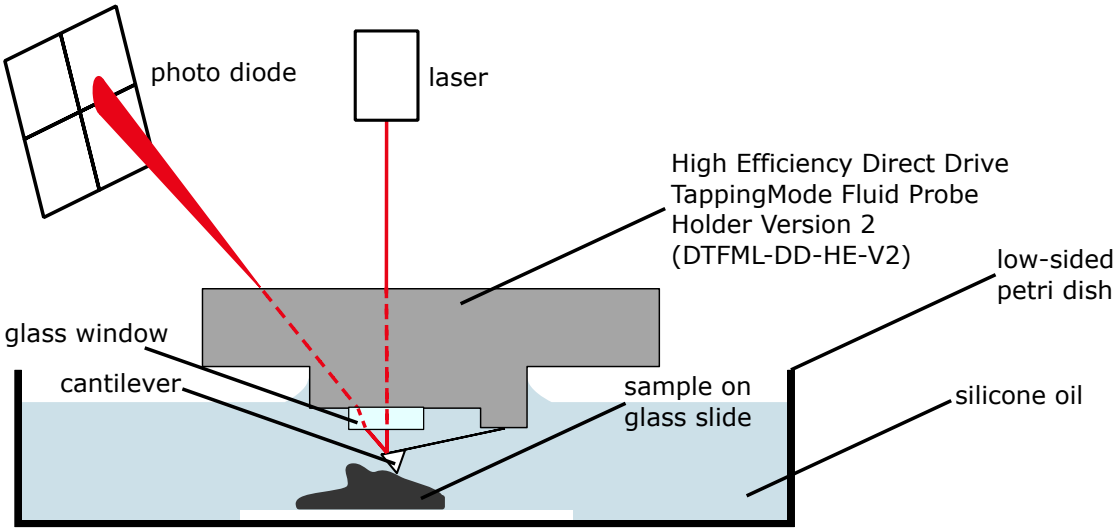

Figure 3.2: The friction force measurements of the beetle joints in their different drying stages were measured in the depicted setup (not to scale). The sample was submersed together with the cantilever in silicone oil, conducting the measurement and calibration inside the medium. This prevents changes in the sample and measurement conditions.

The use of silicone oil as suitable measurement liquid was tested with a similar lubricating biological material in the lab (see Fig. 3.3), before applying it in the AFM setup. For that, the colored mucilage of chia and quince seeds was covered with silicone oil in test tubes and left untouched for two weeks next to an uncovered setup. While the mucilage in the test tube without the silicone oil evaporated, the mucilage in the test tube with the silicone oil was unchanged. The silicone oil and mucilage also withstood mixing and diffusion, which was apparent due to the coloring of the mucilage with the water soluble colorant Eosin B. Eosin B itself is insoluble in silicone oil which was tested as well.

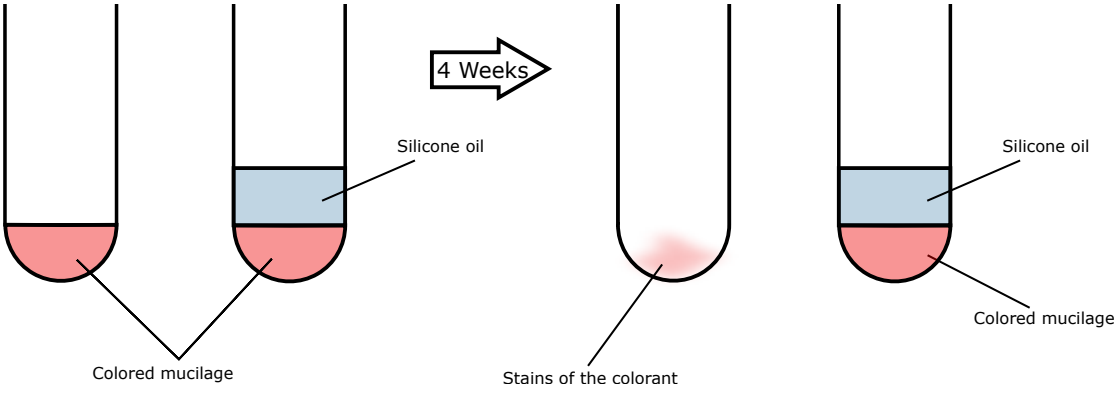

Figure 3.3: The depicted setup was used for the testing of the compatibility of the silicone oil with a biological water-based fluid, namely the mucilage, which forms, when seeds like chia or quince seeds get submersed in water. The distilled water was colored with Eosin B, before being fed to the seeds. The mucilage formed after a few hours, was separated from the seeds and covered with silicone oil or left uncovered. The setup stayed untouched in a fume hood for four weeks, after that, the mucilage had evaporated completely for the uncovered test tube, while the mucilage covered with silicone oil appeared unchanged. There was no mixing and evaporation of the components apparent.

3.4.1 Calibration of friction measurements with the AFM

To get results comparable with other experiments one needs to calibrate the friction measurements. Each change of the cantilever, each change of the laser point position, intensity and dilation have an influence on the friction force measured. Many options of friction force calibration are proposed, the most common being the so called *Wedge method* [41], which has been improved, simplified and complicated multiple times, making it even possible to use a commercial TGF11 grating [42] [43]. Unfortunately, the TGF11 grating has valleys of very limited distance (5 μm), making it impossible to use it with colloidal probes with bigger diameters. A comprehensive review of calibration methods can be found in the publication by Munz *et al.* [44] with a detailed list of numerous methods including advantages and drawbacks. Unfortunately, most of the commonly used methods for friction force calibration are not applicable for the entirety of this thesis, due to the special requirements for experiments conducted in air and liquid as well as the use of cantilevers with sharp and colloidal tips. The most promising technique for these needs was the one from Anderson *et al.* [45]. Therefore, I adapted this method for a consistent application.

The original calibration technique utilizes pulled glass pipettes as their calibration substrate. During my first measurements, however, it became quickly apparent, even though the glass pipettes are inexpensive, that the composition of the glass can lead to the formation of a thin film in contact with a cantilever. This can be detected by scanning a bigger area after the scan of a smaller contained area, where the friction loop shows a clear difference and even the thin layer can be detected in the topography. To circumvent this problem, I use sapphire half spheres with a diameter of 0.4 mm (Edmund Optics, UK) (see a sketch for that process in Fig. 3.4). This allows for a constant and unaffected calibration with both sharp tip and colloidal probe as well as measurements in air and liquid. For the acquirement of the calibration factor the method was switched from manual user input to an automatic iterative process to speed up the calibration process. The full python code for the analysis of the calibration factors including all modules to read data from the instrument files can be found here: https://doi.org/10.35097/8zdzrbcgxyu4417s

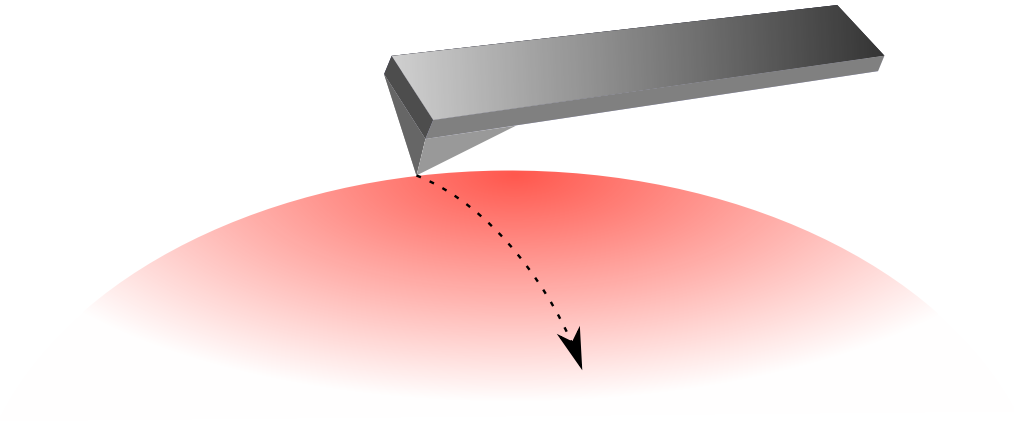

Figure 3.4: For the calibration a half sphere with a diameter of 400 μm was used, where the cantilever scanned the top of the sphere with a scansize of 50 μm x 50 μm as a basis for the calibration algorithm

As described in Section 2.1, for surfaces with an inclination the friction measurements get offsetted proportional to the tangens of the slope. In the case of a spherical surface this results in a negative slope for the friction loops if the scans direction and sign is as described in Figure 2.3. For the NanoSurf Instrument the sign of trace and retrace is recorded inverted by the system leading to a positive slope. This has to be accounted for in the code to guarantee positive calibration coefficients. Some instruments like the Dimension Icon have an unaccounted tilt in the friction loops even for flat samples and measurements without any contact to the surface. We assume that this tilt is a result from the bending of the piezotube, tilting the cantilever without sample contact (see Fig. 3.5). This unwanted effect interferes with the calibration of the friction force. In order to receive correct results for the calibration,

the system specific tilt of the instrument can be obtained by scanning the friction loop of a flat sample and subtracting the mean of the friction loops from the calibrating scans. For this reason the calibration has to be conducted for each chosen deflection setpoint, making the calibration more time-consuming but also more accurate.

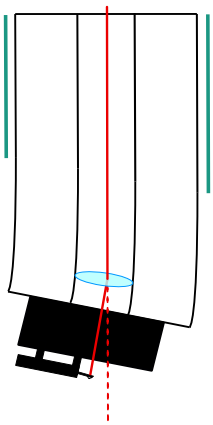

Figure 3.5: Bending of the piezotube leading to the cantilever moving away from the laser beam. The Bruker instrument corrects this error with a correcting lens, but this is apparently still not enough to eliminate the error completely, resulting in a tilt of the friction loop. The bending of the tube is greatly exaggerated in this graphic.

Below the pseudocode (see Algorithm 1) is written down, including the formula from [45], which have been adapted slightly for the new geometry of the sapphire half sphere. For the successful determination of the calibration factor β the AFM data must include the topography and the friction loop (if necessary the friction loop is tilt corrected as described above). Furthermore, the loading force (requiring deflection setpoint and spring constant), adhesion force between sapphire half sphere and cantilever tip, the cantilever angle of repose ϕ, which is in most commercially available cantilevers about 10°, the test slope μ and the pixelsize are needed as input for a successful calibration. In the original publication the test slope μ of effective normal force to the lateral difference has been adapted manually to acquire the best possible results. In order to save time and get reliable results a simple loop narrowing in on the most accurate slope with a tolerance of 10^{-5} was introduced. The function stats.mstats.linregress has been imported via the module scipy. For a more in-depth information about the formulas and the development of the calibration technique, I refer to the original publication by Anderson et al. [45] as I only highlight the changes with which I adapted the work.

Algorithm 1 The basic pseudocode to calculate the calibrationfactor β from the half sphere friction loops. Method and formula have been adapted from [45].

Require: data: $frictiontrace$, $frictionretrace$ and $topography$, loading force $load$, adhesion force f_{adh}, cantilever angle of repose ϕ, pixel size $pixel$

Ensure: tilt correction of trace and retrace if necessary, remove static friction

Require: test slope: μ_t ▷ Usually $\mu_t = 1$ is a good start here

$lfm_{average} = (trace + retrace)/2$

$lfm_{diff} = trace - retrace$

$\theta = arctan(numpy.gradient(topography, axis = 0) \times pixel)$ ▷ Angle of the sphere at each point in x-direction

$\alpha = arctan(numpy.gradient(topography, axis = 1) \times pixel)$ ▷ Angle of the sphere at each point in y-direction

$tolerance = 10^{-5}$

$i = 0$

$maxiter$ ▷ maximum number of iterations to avoid neverending loops

while $i < maxiter$ **do**

    $part_1 = load \times tan(\theta) \times (cos(\phi) + \mu_t^2 \times cos(\alpha)^2 \times sin(\phi)/cos(\theta))$

    $part_2 = f_{adh} \times \mu_t^2 \times cos(\alpha) \times tan(\theta)/cos(\theta)$

    $lat_{average} = (part_1 + 2 \times part_2)/(1 - (\mu_t \times cos(alpha) \times tan(theta)) \times (\mu_t \times cos(\alpha) \times tan(\theta)))$

    calibration = stats.mstats.linregress($lfm_{average}, lat_{average}$)

    $f_{eff} = (load \times cos(\phi) \times cos(\alpha) \times (cos(\theta)^{-1} + tan(\phi) \times tan(\alpha)) + 2 \times f_{adh})/(1 - (\mu_t \times cos(\alpha) \times tan(\theta))^2)/cos(\theta)$

    $lat_{diff} = calibration.slope \times lfm_{diff}$

    $\mu = stats.mstats.linregress(2 \times f_{eff}, lat_{diff})$

    if $\mu.slope \leq \mu_t + tolerance$ and $\mu.slope \geq \mu_t - tolerance$ **then**

        Found calibration factors

        $\beta = calibration.slope$ ▷ β is the calibrationfactor in N/V

    else if $i == maxiter$ **then**

        Calibrationfactor could not be found with test μ ▷ Adapt test μ and try again. It is possible, that the test μ fluctuates between two close values, then the maxiter is exceeded, but the calibration factors are still applicable.

    else

        $\mu_t = \mu.slope$

        $i = i + 1$

    end if

end while

3.4.2 Friction coefficient analysis

After obtaining frictional data from the AFM scans an analysis is necessary to obtain the comprehensive results. For this purpose, I extracted the friction loops of interest and calculated the difference between the trace and the retrace and divided it with the factor 2 for each pixel. By averaging over these values, I obtain the uncalibrated mean lateral force of the region of interest in volts. For an usable data set, I multiply this value by the calibration factor as obtained from the calibration of the system as described in Section 3.4.1 to obtain the frictional force for the specific deflection setpoint corresponding to the specific loading force. As a comparable property, the classical coefficient of friction (COF) μ was chosen over more complicated microscopic laws [46] [47], as can be obtained with the following well-known linear friction law [48]: $F_{fric} = F_0 + \mu F_{load}$. Here F_{fric} is the measured frictional force, after calibration of the lateral force as measured with the AFM, F_0 is the possible offset, μ is the COF and F_{load} the loading force as applied by the cantilever on the sample. In theory, one scan with the AFM would be sufficient to obtain the COF, by simply dividing the obtained frictional force by the applied loading force. Nonetheless the COF is more accurate if the same position is scanned multiple times changing the deflection setpoint corresponding to the loading force. By plotting the values of the calibrated frictional force over the loading force, a linear fit will describe a more accurate picture of the COF as well as unveil a possible hysteresis or problems with the AFM scans (see plots in Fig. 3.6). This procedure has been applied to obtain all COFs presented in this thesis to ensure comparability.

The data used as the basis for the COF of the beetle joints has been obtained with the same cantilever in silicone oil. Scans with 512 x 512 data points (i.e. pixels) have been obtained at multiple positions. Each scan has been performed successively on the same position with increasing deflection setpoint until the lubricant was scratched off. The lowest possible deflection setpoint in silicone oil was 1 V, corresponding to about 500 nN loading force. Below this point the cantilever tip experienced a lift-off leading to a blurry topography and unreliable results. The deflection setpoint was increased by 0.5 to 1 V steps, limited by the ability of the AFM to retain the setpoint in a range of 0.5 V over the duration of the scan. The upper limit of 6 V was chosen to prevent destruction of the cantilever and samples. In most cases, the lubricant did not withstand the full force of these setpoints and the scans were stopped preemptively. The scanning speed and scan size was kept constant for most scans to reduce manipulation of the data due to different kinetic forces. For the COF at least three different frictional force values of three different applied loading forces have been used in a numerical linear fit.

Each scan used in the analysis for the COF of the beetle's joints includes different features, useful to the analysis. Apart from the analysis of the full scan, different regions of the scan have been extracted to obtain COF also for the "flat" surface, the "micro-structured" surface, "pores" if encountered and the "lubricant". The extraction of the data sets used for the analysis of these COF was done manually. I inspected each individual data set seperately

with the help of the topography data and deflection error data to visually assign the different areas. The specific data was extracted from the combined data set of the scans of the specific position in a rectangular fashion excluding features, which are not the required features. The assignment of the region of interest for the flat and microstructured surface was based on the first deflection setpoint, while the assignment of the region of interest of the lubricant was based on the last deflection setpoint still including lubricant. This is based on the fact, that the cantilever is removing material of the lubricant with each scan, shrinking the lubricant patches needed to assign the regions of interest. The COF of the different features of the scans have been obtained as described above. This procedure has been repeated for all collections of scans for different positions. The obtained COF of each feature of each position are then averaged for a COF of the feature of the beetle of the specific drying state. The error bars for these COF have been obtained by averaging the standard errors of the linear fit for the COF, after weighing them by the number of used data points to ensure a more accurate picture of the system. For a visual description of the extensive process see Figure 3.6.

Unfortunately, due to the difficult geometry of the beetle's joints and some internal problems of the AFM, sometimes negative COF have been recorded. Of course these data sets have been excluded from the analysis.

The data acquisition of the 3D-printed test structure samples is similar to the one described for the beetles' joints. Scans of the microstructures have been obtained with 512 x 512 pixels with two different cantilevers, one with a sharp tip and one with a glued glass sphere. The scans include a small area of the flat surface, the structures have been printed on, to preserve the same scan speed and size for all scans. Each microstructure has been scanned for ten deflection setpoints starting at 1 V increasing to 5 V by 1 V steps before reducing the deflection setpoint from 4.5 V to 0.5 V, corresponding to about 50 nN for the sharp tip and 100 nN for the colloidal tip, by the same step size. A small hysteresis of reduced COF on the decrease of the deflection setpoints can be observed. The analysis of the coefficients of friction of the 3D-printed test structure samples is straight-forward. The structured surface is extracted from the overall scan excluding the behavior of the static friction at the edges of the scans calculating the lateral forces, calibrating these to obtain the frictional force, which are plotted over the loading force to numerically approximate the slope to obtain the COF of the microstructured surface.

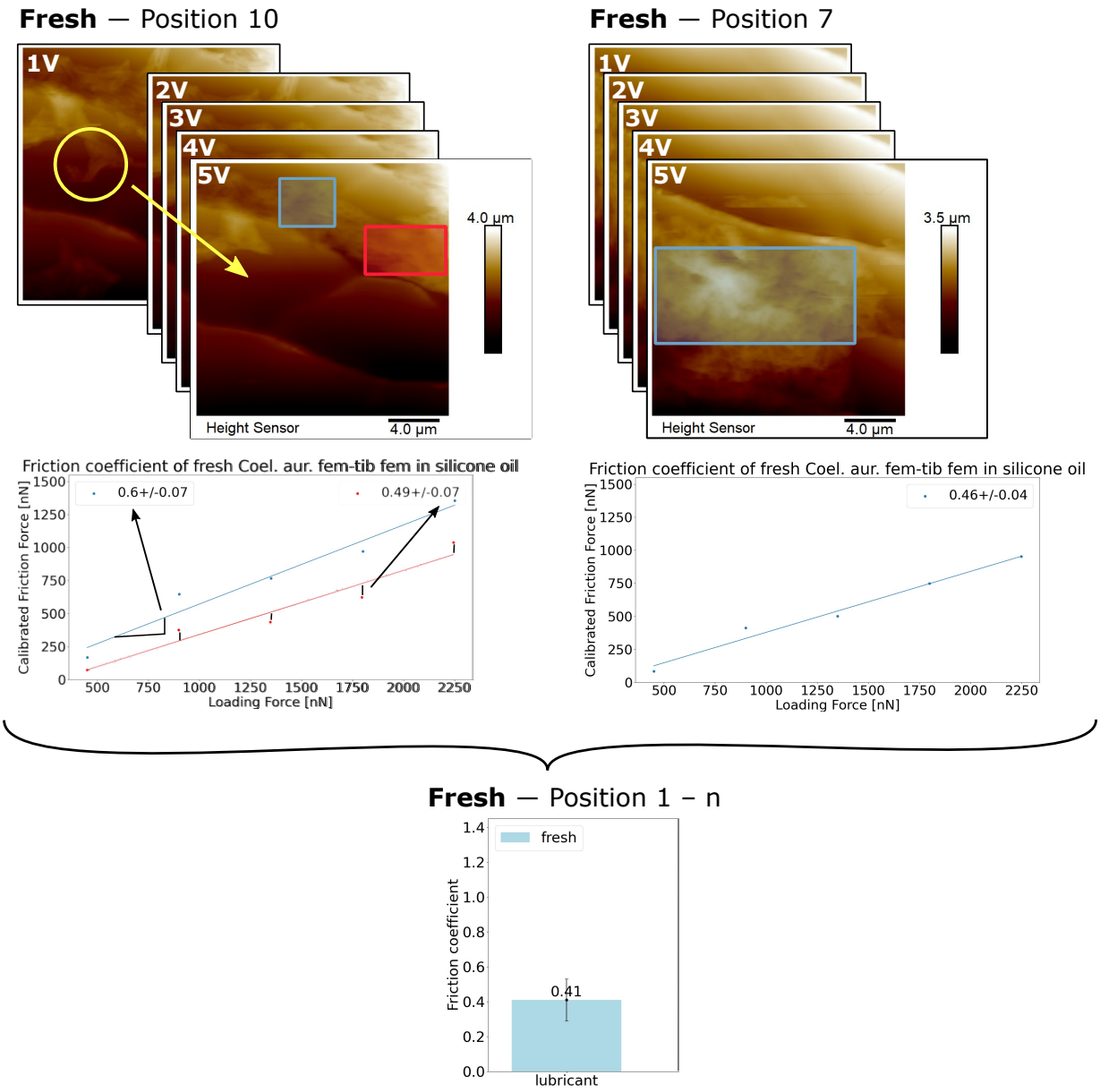

Figure 3.6: Schematic of the COF analysis for an exemplary data set of three positions of a fresh *C. aurata* joint.

3.5 Synchrotron X-ray microtomography

The synchrotron X-ray microtomography (μCT) allows for a 3D depiction of the specimen without the need for a destructive dissection. The μCT reveals a detailed picture of the surface as well as the innerts of the specimen, giving insight into the biomechanics. The segmented data of the μCT also allows for accurate models and holds the possibility for upscaling of these.

The beetle for μCT measurements was preserved and scanned in ethanol. A scan of the whole beetle as well as a detailed scan of one femoro-tibial joint was performed with the μCT. A specimen was scanned in 99 % ethanol at the IMAGE beamline of the Imaging Cluster at the KIT Light Source [49]. The beam produced by the superconducting wiggler was filtered by 2 mm pyrolytic graphite and monochromatized at 18 keV by a Double Multilayer Monochromator (DMM). We employed a fast indirect detector system consisting of a scintillator, visible light optics, a white beam microscope (Optique Peter) [50] and a 12-bit pco.dimax high-speed camera (Excelitas PCO GmbH) with 2016 $\times$ 2016 pixels of 11 μm physical size. We employed two scans at 2x magnification to capture the whole beetle, and a single scan of the femoro-tibial joint region at 10x magnification, resulting in effective pixel sizes of 2.44 μm and 1.22 μm, respectively. For each scan, we took 200 dark field images, 200 flat field images, and 3000 equiangularly spaced radiographic projections in a range of 180° with a frame rate of 100 fps (2x) and 70 fps (10x) . The control system concert [51] acquired the data automatically. Data processing (dark and flat field correction and phase retrieval) was performed by the UFO framework [52]. The final tomograms were reconstructed with tofu [53] and yielded phase and absorption contrast data sets, which were blended and converted into 8-bit volumes. The scans have been performed with the kind help and support of Thomas van de Kamp (KIT) and Jenny Hein (KIT).

3.6 Nano-computed tomography

Similar to the μCT, the nano-computed tomography (nanoCT) is a non-destrucitve method to gain insight into an opaque material. The resolution of the system is much higher than the μCT allowing for a detailed analysis of surface microstructures, structures within the material and structuring of the material [54].

Beetle joint samples were scanned using the lab-based nanoCT Zeiss Xradia 810 Ultra, which employs a chromium anode to produce a quasi-monochromatic X-ray beam with energy of 5.4 keV. A sequence of optics is used to achieve a pixel size of 128 nm or 256 nm within a 65 μm field of view. The samples were scanned using Zernike phase contrast mode with the number of projection and exposure time varying depending on the sample. 501, 901, 1001 or 1201 projections were acquired over 180°, with acquisition time per projection of 10 s to 40 s. The 2D projections were reconstructed into 3D data using the proprietary software Zeiss Scout and Scan Reconstructor version 13, a software based on filtered back projection algorithm.

Four samples of *O. sulcatus* were prepared in different ways for the scans with the nanoCT. Two samples have been airdried, one sample has been critical point dried with a EM CPD300 system (Leica Microsystems, Germany) and one sample has been chemically dried with 3M™ Novec™ 7100. The non-airdried samples have been stabilized in ethanol before the preparation with the CPD or Novec. The dried samples have been dissected to obtain the region of interest hosting the pores in sizes of about 100 μm to simplify the alignment

and reduce the scan time. Samples of correct size have been glued on pins for the scans in the nanoCT. The scans have been performed with the kind help and support of Rafaela Debastiani (KIT, now at Helmholtz Institute Freiberg for Resource Technology).

3.7 Focused ion beam

The focused ion beam (FIB) is almost exclusively available with a SEM to image the topography and monitor the progress. The FIB can be used both to fabricate intricate microstructures with material abrasion with ions as well as record a tomography, by alternating between destructively removing a thin slice of the sample and imaging the exposed cross-section.

To provide technical surfaces, showing comparable structures as those of the biological model surfaces, a FIB system (ZEISS Auriga 60) was used to prepare structured Si-surfaces. For this purpose, several areas with a saw tooth profile have been milled. The size of each of the field was ca. 70 μm x 70 μm, showing 12 (periodicity of 6 μm) or respectively 24 (periodicity of 3 μm) cavities. In order to optimize the surface quality of the structures, and to increase the milling speed, two different beam currents of the gallium ion beam (120 pA and 600 pA) have been used. In order to analyze the influence of the depth of the structures by AFM, different doses have been applied to the silicon substrate samples, resulting in a depth of the structures between 3 nm and 35 nm or 5 nm and 65 nm, respectively. The structures were analyzed afterwards using AFM and confocal microscope MarSurf3D CL select (Mahr, Germany).

In order to analyze and understand the 3D structure of the pores in the beetle joints, samples have been prepared and analyzed using focused ion beam (FIB) and scanning electron microscopy (SEM). The samples for the FIB have been airdried and fixed on a SEM aluminium stub with a carbon sticker. Afterwards the samples have been sputter coated with a thin gold layer in order to make the sample surface conductive to avoid charging of the samples during the SEM analysis. Afterwards the samples have been transferred to the FIB-SEM-system (TESCAN AMBER). In a first step, a trench has been milled using the Ga-Ion beam with an acceleration voltage of 30 kV and a beam current of 20 nA. Afterwards a tomography of the volume of interest (VOI) has been acquired. The data shown in this publication refers to three tomographies. In all cases an acceleration voltage of 30 kV and a beam current of 10 nA has been used to cut the slices. The thickness of each slices was 50-75 nm. The SEM images have been acquired using an an acceleration voltage of 5 kV and a beam current of 300 pA, and a pixel size of 50-75 nm. For the first tomography ca. 1600 slices have been acquired with a height of ca. 46 μm and a width of ca. 44 μm. The second tomography consists of ca. 1400 slices and a height of ca. 57 μm and a width of ca. 73 μm. The third tomography consists of ca. 1200 slices and a height of ca. 62 μm and a width of ca. 65 μm. For each tomography data of 3 different detector signals have been recorded,

while for the reconstruction of the 3D information mainly the ET detector signal (in chamber Everhart Thornley secondary electron detector) was used. The FIB measurements have been conducted with the kind help and support of Matthias Mail (KIT).

3.8 Post-processing of volumetric data

All volumetric data (μCT, nanoCT, FIB) was pre-segmented in Amira 2022.2 (every 10-20 slices depending on the contrast). The pre-segmented labels served as input for smart interpolation with the online tool biomedisa v24.7.1 (accesible through biomedisa.info) [55]. The results were imported back into Amira and minor errors were corrected. Afterwards the surface meshes were generated, which were smoothed, reduced and cut in Paraview 5.12 [56] before being imported, rendered, posed and animated in blender 4.4 [57].

In Figure 3.7 a rendering of the full body μCT scan is depicted. The process as described above was applied and the beetle was posed in blender according to the constraints of the respective joints to allow for a more animated depiction, since the beetle was scanned in its deceased curled up state.

Figure 3.7: The 3D-rendering of the low resolution full body μCT scan of the weevil *O. sulcatus*. The data was pre-segmented in Amira, completed with biomedisa before being colored, posed and rendered in blender. The green surface, on which the beetle is standing, has been modeled in blender. The researched parts of the legs, the femur and tibia have been colored green and red, respectively.

4 Evolution of the lubricant found in the joints of the examined beetles upon drying as imaged with the SEM

With the limited research concerning the lubricant in the joints of arthropods, the selection of a suitable research object was difficult. Therefore, the goal of this section is the discovery of lubricant in the beetles *C. aurata*, *O. sulcatus* and *O. salicicola* and characterizing the behavior of the lubricant after the death of the beetle with the help of the SEM.

This chapter includes research data already described in the publication:
Cornelia F Pichler, Richard Thelen, Thomas van de Kamp, and Hendrik Hölscher. Friction coefficient evolution of drying lubricant in the joints of beetles by friction force microscopy. Tribology Letters, 73(1):1-10, 2025.

4.1 The lubricant of *Coelorrhina aurata*

C. aurata was chosen as a potential comparison to previous studies and is the biggest beetle examined in this thesis with joints spanning almost one millimeter. Figure 4.1 a) displays SEM images of the tibia of the femoro-tibial joint of the beetle *C. aurata*. In the inset to the right, the pores extruding lubricant are highlighted with arrows. The pores are found in a deep crevice of the tibia lubricating the main frictional surface of the femoro-tibial joint. Since this geometry is not accessible with an AFM tip, the counterpart of the femoro-tibial joint was chosen as the study subject. The opened femur of the femoro-tibial joint is shown in Figure 4.1 b), where the lubricant is distributed naturally by the movement of the beetle's leg, transferring from the tibial concavity hosting the lubricant extruding pores to the femoral condyle and from there the lubricant is transported out of the joint over the microstructured surface shielding the joint from environmental impact and soiling. In the inset to the right, the lubricant patches (marked exemplary with arrows) on this surface can be observed, which were the basis for the friction force measurements. The lubricant undergoes no observable change as observed with the SEM (See Fig. 4.1 c)). To confirm this observation, the friction force measurements were conducted on three different samples in their air-dried state.

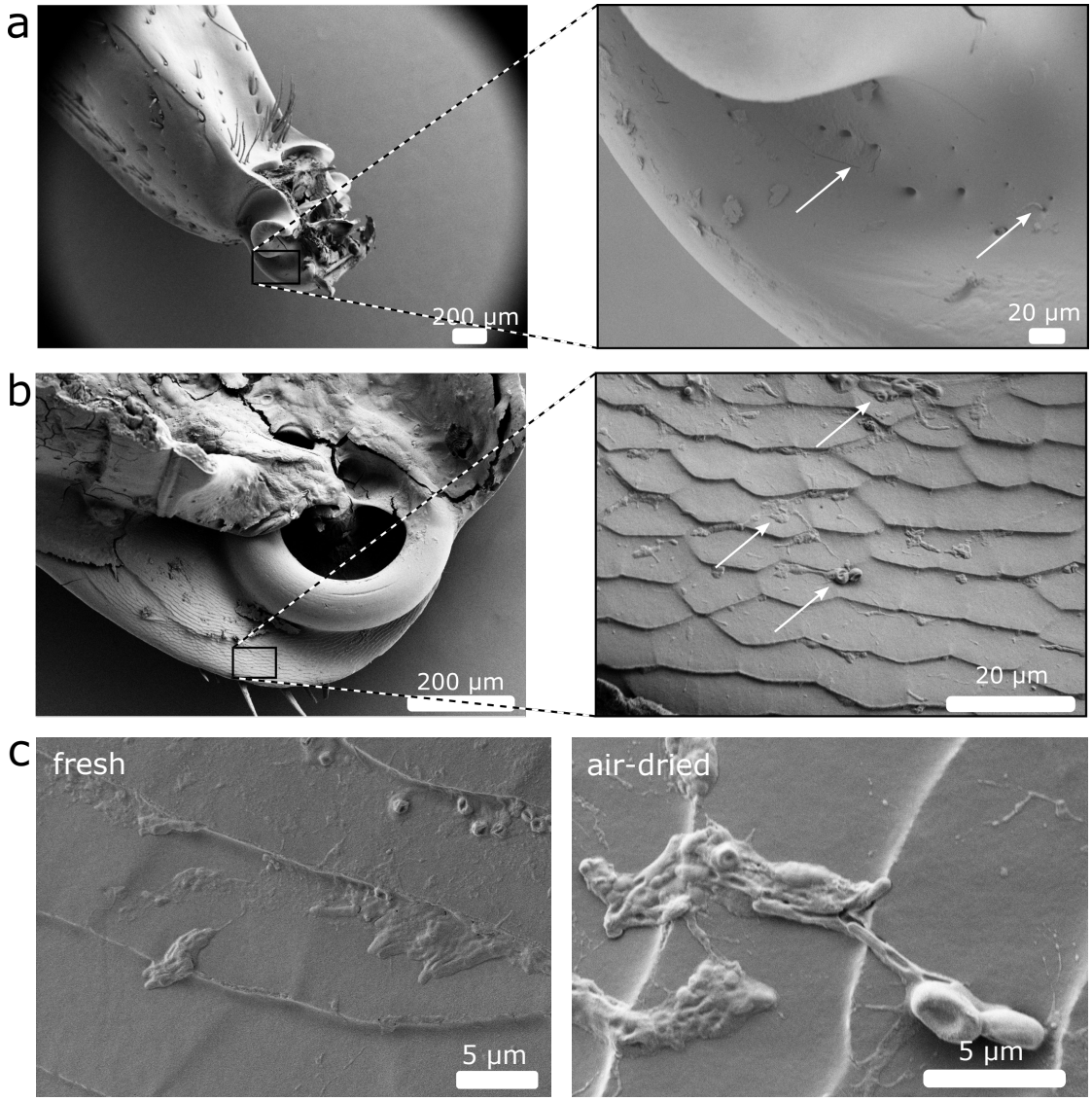

Figure 4.1: a) A SEM overview image of the tibia of the femoro-tibial joint of *C. aurata*. The joint was dissected shortly after the death of the beetle. The white arrows in the inset point exemplary to lubricant extruding from the pores in the tibial cavity of the femoro-tibial joint. b) A SEM overview image of the femur of the femoro-tibial joint of *C. aurata*, which is the counterpart to the tibia and the geometry is favorable for the AFM measurements. The white arrows in the inset point to residues of the lubricant. The inset also shows the hexagonal shingle-like microstructures found on the cuticle. c) Comparison of the lubricant of a fresh and an air-dried sample. There is no visible change detected with the SEM.

4.2 The lubricant of *Otiorhynchus sulcatus* and *Otiorhynchus salicicola*

The family of the weevil was chosen as a study object, due to its tight form closure in the joint. The very small gap between the joint partners invokes the hope of finding a water-based lubricant, due to the boundary regime conditions. The μCT data of the weevil *O. sulcatus* verifies the assumption of a very tight gap between the joint partners (see Fig. 4.2). Due to the similarity of *O. sulcatus* and *O. salicicola* and their joints (not depicted here), I suspect, that the joint partners of *O. salicicola* show a similar clearance.

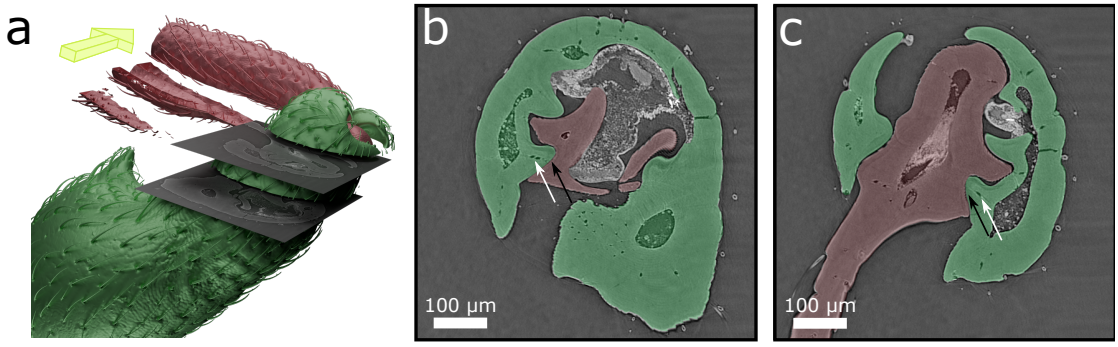

Figure 4.2: a) The 3D-rendering of the surface of femur (green) and tibia (red) of *O. sulcatus* has been cut at the respective positions of the μCT slices on the right. The cuts have been translated in the direction of the arrow to allow a less obstructed view into the cuts and µCT slices. b), c) Two slices of the µCT data showing the tight form fit in the area of the femoral surface hosting the pores. Black arrows point to the tight gap between the tibia (red) and femur (green). The difference between different cuticle types and structures are visible and the pores connecting the haemocoel and the frictional surface are indicated by white arrows.

In Figure 4.3 a) the frictional area, where the lubricant can be commonly found and where the friction force measurements were conducted is marked with a green crescent marker. The pores extruding the lubricant on an unstructured surface are enabling a multitude of measurements, for example friction force measurements, focused ion beam tomography and nanoCT. Some of these measurements would be impossible with the often very restricting geometries inside the beetle joints. Since there is a clear difference observable between the fresh sample (Fig. 4.3 b)) and the air-dried sample (Fig. 4.3 c)), a possible evaporation/aging of the lubricant was investigated as follows.

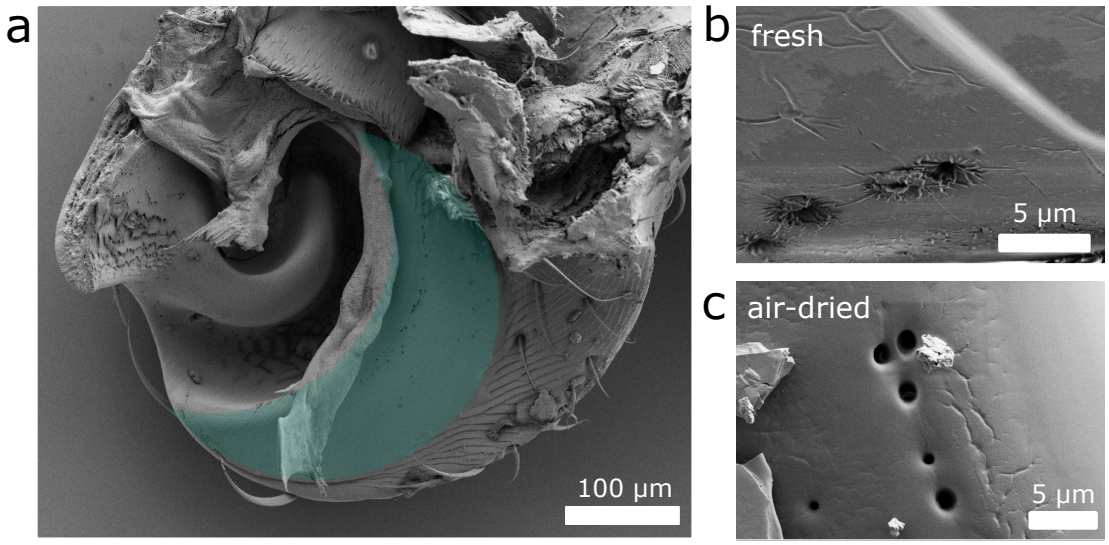

Figure 4.3: a) A SEM overview image of the dissected femur part of the femoro-tibial joint of *O. sulcatus*. All measurements conducted in this thesis have been enabled by the favorable flat structure of the frictional crescent area highlighted in this image. This represents the region of interest, where most of the pores – extruding lubricant – are located, allowing for the deployment of different analysis methods. To the right two SEM images of b) fresh pores with extruding lubricant and c) pores in the air-dried state (air-dried for a month) showing cracking in the cuticle and no traces of the lubricant on the femur part of the femoro-tibial joint of *O. sulcatus* are depicted. Despite the existence of pores in other areas of the femoro-tibial joint and other joints, the pores on the crescent region of this joint were analyzed, due to the geometrical constraints of the AFM. The femur of the femoro-tibial joint of *O. salicicola* show minor differences in size and density of the pores. Nevertheless it resembles the femur depicted here in its crucial parts, *The figure was adapted and already published in [58].*

In Figure 4.4 the evolution of the lubricant in the joints of the two weevils *O. sulcatus* and *O. salicicola* can be observed over a timeframe of 16 days. For this experiment two beetles of each genus were first anesthetized with CO_2 and then killed. The legs were removed from the body sequentially and stored in an airtight glass container till analysis. Directly after the beetle's death three legs in sum were removed (fore-, mid- and hindleg) from each beetle, to eliminate the possibility of different geometries or lubricants depending on the leg. After sputtering the opened legs with around 7 nm of silver and reviewing the legs with the SEM, no significant difference concerning geometry or lubricant was observed. The legs are therefore not distinguished for the rest of the thesis. The procedure of opening the legs, sputtering them with silver and examining them with the SEM was repeated 24 h, 48 h, 96 h, 192 h and 384 h after the beetle's death with a single leg, respectively, storing the

remaining beetle with attached legs, in the airtight container. The glass container showed light condensation on the walls since the water contained in the body of the beetle and the haemolymph evaporates after the death of the beetle. Figure 4.4 includes exemplary SEM images for each timestep showcasing the most common lubricant appearance. There is a clear change in the appearance of the lubricant between 24 h and 48 h. The lubricant changes the state of smooth, continuous and flowy in the first day, to crumbly and patchy observable from two days onward. Both the fresh lubricant and the 24 h air-dried lubricant flow in the direction of the slight tilt, in which the joint half was fixed. For the timesteps after that, the lubricant is mostly stuck in the pores or if there is a flow of the lubricant, it is not connected to any tilt.

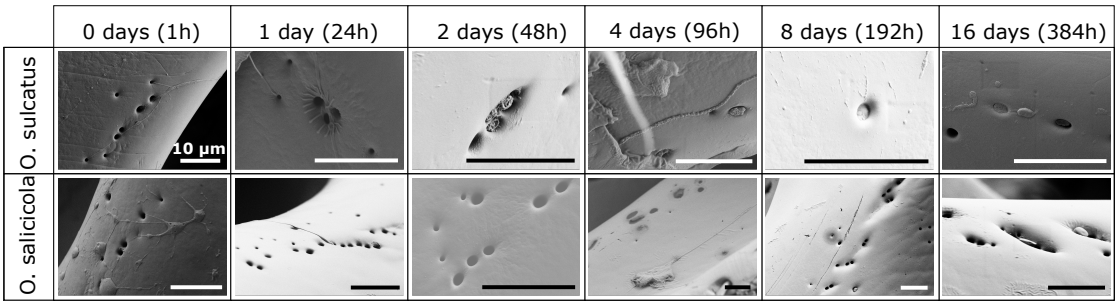

Figure 4.4: The evolution of the lubricant of *O. sulcatus* and *O. salicicola* under the SEM, showing a clear change of the lubricant, from a stream following the slope of the joint in the images including one day old samples, before cracking and wrinkling can be observed from two days onward. The scale bar in all images corresponds to 10 μm.

Additionally, a fresh joint of the weevil *O. salicicola* was examined in frozen condition with an Environmental SEM. The resulting images lead to an interesting hypothesis. In Figure 4.5 a broken seta – the hair found on beetles – can be observed. This seta is presumably obstructing the movement of the joint and can lead to damage of the frictional surfaces, if it is not expelled from the joint. The beginning of the process of the transport of the hair out of the joint is visible in the image: the lubricant is being extruded from the pore opening, engulving the seta to transport it out of the joint.

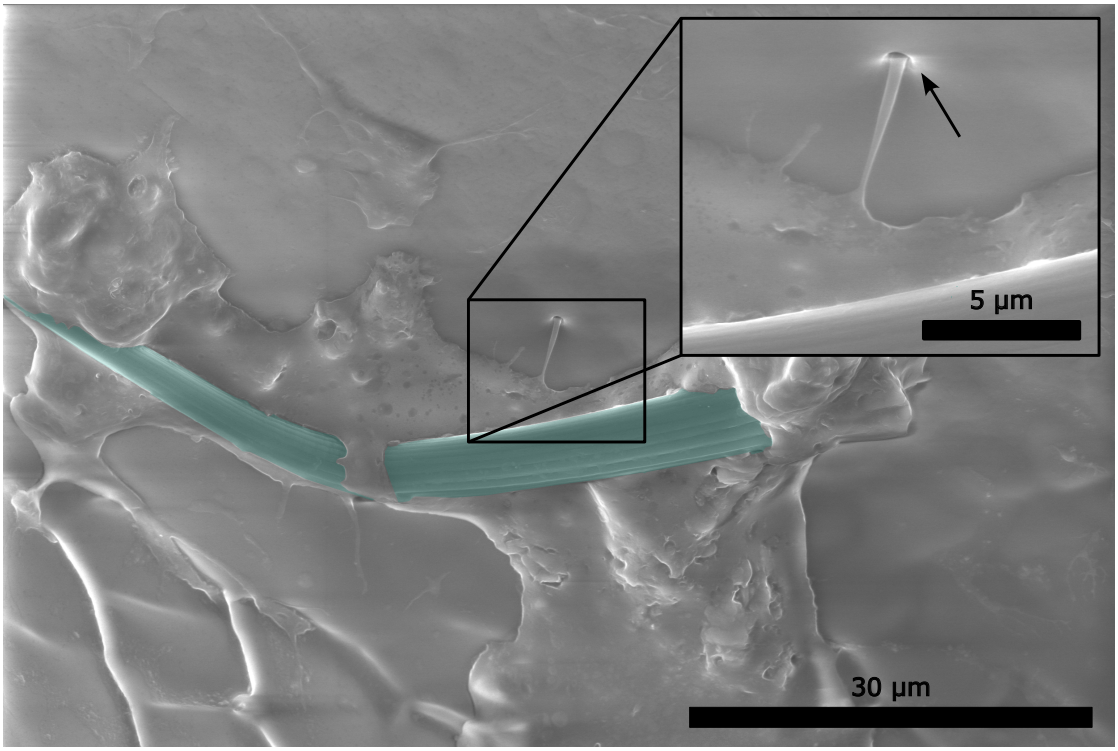

Figure 4.5: An SEM image taken with the Environmental SEM of the frozen lubricant of *O. salicicola* transporting out a broken seta (stained in the image in green). The inset shows a magnified pore (black arrow) extruding the lubricant.

These results reveal a clear difference between the lubricants of the two different beetle species. The lubricant of *C. aurata* undergoes no discernible change under the SEM. It is extruded from pores located in the tibial concavity, complicating further measurements. Therefore, the lubricant patches transferred to the femur of the femoro-tibial joint are the region of interest for measurements below.

On the other hand, the lubricant found in the two weevils changes over the time of just 48 hours, while being extruded from pores in a favorable position located on a flat surface on the femur of the femoro-tibial joint, facilitating the subsequent measurements (see Fig. 4.3).

5 Evolution of the coefficient of friction of the beetles *Coelorrhina aurata* and *Otiorhynchus sulcatus* acquired with the FFM in silicone oil

The previous chapter hinted at a change in the lubricant of the different beetle species and over time for the weevils. Unfortunately, the SEM images are only a snapshot recorded in vacuum of samples which have been sputtered with a thin layer of silver to stop the aging process. Naturally, this process can interfere with the consistency of the lubricant and the actual age of the samples. Nevertheless, there is a strong indication of a difference in appearance and aging of the lubricants or the lack thereof. To confirm this claim an experiment to discover the difference in the lubricants via the change of the COF was set up. Due to the time-consuming nature of AFM measurements, the goal was to find a clear indication for a change in the consistency of the lubricant for *O. sulcatus* and accordingly the missing change in *C. aurata*. I am not aiming for a determination of the instant of time, when the lubricant is changing with the help of the AFM. This is due to the possibilty of manipulation with the cantilever that renders the method simply unsuitable.

Parts of this chapter include research data already described in the publication:
Cornelia F Pichler, Richard Thelen, Thomas van de Kamp, and Hendrik Hölscher. Friction coefficient evolution of drying lubricant in the joints of beetles by friction force microscopy. Tribology Letters, 73(1):1-10, 2025.

5.1 Initial measurements on *Otiorhynchus sulcatus*

The first friction force measurements recorded of beetles's joints in this thesis have been made neither in silicone oil nor on the femoro-tibial joint. The first measurements had been made on the microstructured surface of the trochanter of the coxa-trochanteral joint. Unfortunately, the measurements were difficult and not rewarding. The navigation to record measurements on different position of the same trochanter was proving very difficult with mixed results and non-unified scan sizes and scan speeds. The lubricant trapped between the microstructures was hard to spot and required additional scans in tapping mode to get some indication of possible lubricant by the phase contrast, adding additional scan time. The convex surface of the trochanter eventually leads to lift-off of the cantilever and is therefore limiting the scan size and the number of positions on the same trochanter, increasing the need to sacrifice more beetles for little reward. The convex surface and complicated microstructure also leads to a increased cross talk hindering the reliable acquisition of frictional data. Despite the enticing nature of the screw and nut joint, I had to abandon this joint and move on to another. Fortunately, the femur part of the femoro-tibial joint was even more suited for my toolset of methods than I anticipated.

In Figure 5.1 a 3D-image of the scan obtained with the tapping mode in air of the frictional surface of the femoro-tibial joint of *O. sulcatus* is shown. It features five pores, four of which are hidden under lubricant and can only be noticed by the depression of the lubricant. The surface surrounding the pores is mostly flat with a slight roughness. This image has been obtained on a fresh sample and showed severe changes after a few scans, which convinced us to develop the intricate method of AFM measurements in silicone oil stabilizing the samples and measurement conditions.

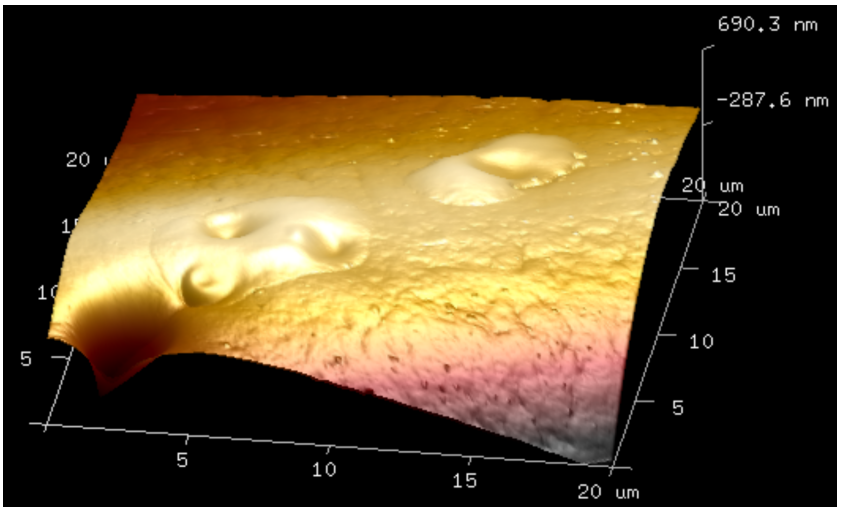

Figure 5.1: 3D-image of a tapping mode scan of the frictional surface of the fresh femur of the femoro-tibial joint of the weevil *O. sulcatus*. The scan shows five pores, four filled with lubricant and the flat surrounding frictional surface.

5.2 Friction force measurements of the femoro-tibial joint of *Coelorrhina aurata* and *Otiorhynchus sulcatus*

The femoro-tibial joints of the two beetles *C. aurata* and *O. sulcatus* were analysed by friction force measurements in different dryness states of the lubricant. Due to the results presented in Section 4 the difference in lubricant and its frictional properties were of interest for this chapter. Due to the missing visual change of the lubricant in *C. aurata* three different dryness states of the lubricant were picked: fresh, two weeks and eleven months air-dried. For the weevil *O. sulcatus* the quick drying period makes a longer analysis with different timesteps unnecessary, so only a fresh and an air-dried sample were analysed. All samples were immersed in silicone oil after the death of the beetle corresponding to the dryness state and measured in silicone oil with the AFM as explained in Section 3.4. This way the long measurement times do not interfere with the purpose of the measurements. With the quick drying of the weevil lubricant this was a serious concern with each measurement taking up to half an hour and at least three measurements needed, the lubricant might change between and during measurements. Even though the change over one single scan might be interest-

ing as well, it is impossible to guarantee that a scan including lubricant can be performed in a short amount of time. The process of finding a suitable position including lubricant as well as interesting features takes time and skill. The fact of working with a biological sample with difficult geometries and differences in a small area further impede the measurements. The changes detected over one scan with the AFM may not be due to the drying of the lubricant, but a mutation or mixing of different components. Overall, the measurements in silicone oil just ease the process and promise more reliable and comparable measurements and sample conditions.

The COF obtained in these experiment are summarized in a bar plot and a table for each beetle respectively. The experiments overall confirmed my hypothesis of the stable lubricant for *C. aurata* and an evaporating lubricant for *O. sulcatus*. Since I performed the experiments directly on the joint of the beetle, this gives me the opportunity to obtain the COF for other surface features as well and to compare them with each other. Furthermore, I discussed them with respect to the results obtained by Nadein *et al.* [18] [19].

5.2.1 Coefficients of friction of the femoro-tibial joint of *Coelorrhina aurata*

The results of *C. aurata* confirm my hyothesis. In Figure 5.2 a) the COF of the different features of the femur of the femoro-tibial joint of the beetle *C. aurata* are combined in a bar plot. It includes all features as identified in Figure 5.2 b) as well as the COF of all features combined in the COF of all the scans and the COF of the sapphire half sphere used for the calibration of the cantilever used here as a control. The COF of the sapphire are almost identical as one would suspect for the same cantilever in the same conditions. The features, discernible in the 3D-image of the topography in Figure 5.2 b), are the lubricant forming rough patches, which change during the scans due to the abrasion with the cantilever; the structures, which are observed as steps; and the flat surface with no structure and lubricant included. The flat surface is the cuticular surface of the beetle joint and allows us to have a value for the COF of chitin, with as little topography crosstalk influence as possible. In Table 5.1 all COF measured for the femor-tibial joint of *C. aurata* are listed.

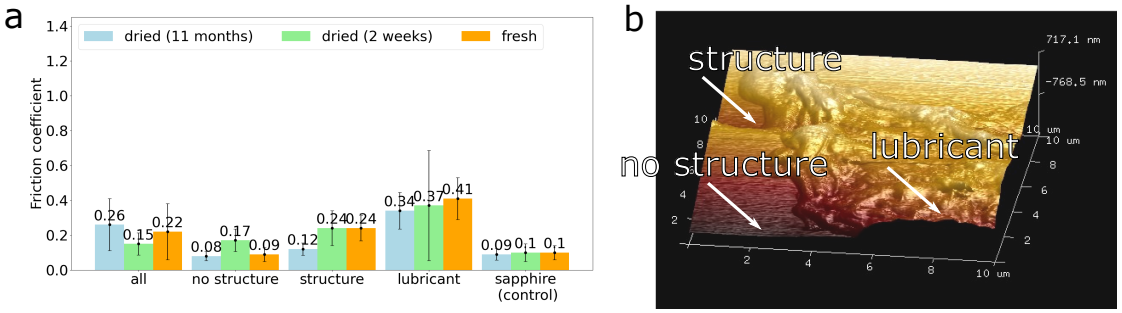

Figure 5.2: a) Bar plot comparing the COF for dried and fresh samples of *C. aurata* obtained by averaging several measurements as shown in Section 3.4.2. After dissecting a dead beetle *C. aurata*, the samples of the femur part of the joint between the femur and tibia were directly immersed in silicone oil for the fresh samples. This process was carried out as quickly as possible to prevent the lubricant from evaporating and keep the system as close to the living conditions as possible. The aged samples were air-dried in a closed container for either 2 weeks or 11 months and immersed in silicone oil directly before the measurements. The friction scans were performed with increasing deflection setpoint. The measurements were aborted as soon as the lubricant was no longer visible on the scans and has therefore dislodged. The friction scans were firstly analyzed including all regions and measurement points, titled in the bar plot as all. During the further process, the different interesting areas – namely flat surface (no structure), structure and lubricant – were extracted from the scans and analyzed. During the calibration procedure, a sapphire halfsphere was scanned and the COF of these measurements are included in this bar plot to highlight the comparability between the scans. b) 3D image of the AFM topography of one position on the femur of the femoro-tibial joint of *C. aurata* measured in silicone oil in contact mode (scan size: 10 μm x 10 μm). The regions of interest for the COF analysis were identified as labeled above: (1) no structure (2) structure (3) lubricant.

The COF of *C. aurata* reveals no immediate surprise. The lubricant being a soft material being subject to change and force has a COF higher than the flat hard surface of the chitin. The structures experience some crosstalk due to the steps and therefore show a higher COF compared to the unstructured surface. Overall there is no significant change of the COF in the different features as all COF lie within the error margin of each other.

Table 5.1: The detailed COF for the measured features on the frictional surface of the femur of the femoro-tibial joint of *C. aurata*

C. aurata	**all**	**no structure**	**structure**	**lubricant**	**sapphire**
11 months	0.26±0.15	0.08±0.03	0.12±0.04	0.34±0.11	0.09±0.03
2 weeks	0.15±0.06	0.17±0.06	0.24±0.11	0.37±0.32	0.10±0.05
fresh	0.22±0.16	0.09±0.04	0.24±0.07	0.41±0.12	0.10±0.04

5.2.2 Coefficients of friction of the femoro-tibial joint of *Otiorhynchus sulcatus*

The results of the lubricant of *O. sulcatus* show a very interesting behavior. In Figure 5.3 a) the COF of the different features of the femur of the femoro-tibial joint of the beetle *O. sulcatus* are combined in a bar plot. It includes all features as identified in Figure 5.3 b) as well as the COF of all features combined in the COF of all the scans and the COF of the sapphire half sphere used for the calibration of the cantilever used here as a control. The bar plot is constructed in an identical manner as the bar plot in Figure 5.2 a) to allow the reader an immediate comparison. However, it includes one more feature: the pores. The COF of the sapphire are almost identical as one would suspect for the same cantilever for the same conditions. The features discernible in the 3D-image of the topography in Figure 5.3 b) are the pores; the lubricant getting trapped in the pores or forming streams and puddles; the structures, which are mostly observed as cracks in the surface; and the flat surface with no structure and lubricant included. The lubricant changes during the scans due to the abrasion caused by the tip-sample contact. The flat surface is the cuticular surface of the beetle joint and allows us to have a value for the COF of chitin, with as little topography crosstalk influence as possible. The cracks, which are included in the category of the structures form mostly in the aged samples. During the air-drying process the water in the cuticle of the beetles evaporates. This leads to shrinkage of the overall beetle and tension in the surface, which can result in cracks. Additionally, cracks or grooves can also be the result of damage and wear within the joints, caused by trapped sharp particles. In Table 5.2 all COF of *O. sulcatus* are listed.

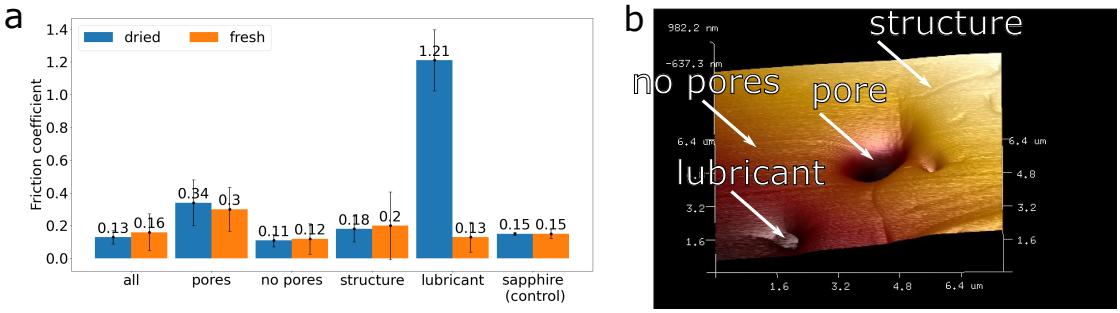

Figure 5.3: a) Bar plot comparing the COF for dried and fresh samples. After dissecting a specimen of *O. sulcatus*, the samples of the femur part of the joint between the femur and tibia were directly immersed in silicone oil for fresh samples in order to prevent the lubricant from evaporating and keep the system as close to the living conditions as possible. Other specimen were air-dried in a closed container for 6 months and after dissecting the femur samples were immersed in silicone oil directly before the measurements. The friction scans were performed at increasing deflection setpoints. The measurements were aborted as soon as the lubricant was no longer visible on the scans and has therefore dislodged. The friction scans were firstly analyzed considering all regions and measurement points. These are titled in the bar plot as "all". Subsequently, different interesting areas – namely flat surface (no pores), pores, structure, and lubricant – were extracted from the scans and analyzed. For the calibration, a sapphire half-sphere was scanned, and the COF of these measurements are included in this bar plot to highlight the comparability between the scans. The lubricant is increasing in adhesion and friction over time. For the fresh sample, the flat surface (no pores) and the lubricant are comparable, which leads us to the assumption, that the surface was covered with a thin layer of lubricant. b) 3D-image of the AFM topography of a position on the femur of the femoro-tibial joint of *O. sulcatus* measured in silicone oil in contact mode (scan size: 7.5 μm x 7.5 μm). The regions of interest for the COF analysis were identified as imaged above: (1) no pores (2) pore (3) structure (4) lubricant.

The COF of *O. sulcatus* needs more explanation than the COF of *C. aurata*. The first feature, that stands out, is the high COF of the dried lubricant of 1.21±0.19 compared to the low COF of the fresh lubricant of 0.13±0.09. This is another indication for the evaporation and definitive change of the lubricant upon aging. The COF of the fresh lubricant is also strikingly similar to the COF of the flat cuticular surface. This supports the assumption, that the lubricant might cover the entire frictional surface, indiscernible to the AFM. That the structures and pores feature higher COF is not surprising due to the topography crosstalk and the trapped lubricant inside the pores leading to increased COF. The error of the COF of

the fresh structured surface is based on the fact, that the cracks form during the evaporation of the sample, which has not yet taken place in the fresh sample. This leads for a reduced data set for the structured category in the fresh samples, which leads to an increased error.

Table 5.2: The detailed COF for the measured features on the frictional surface of the femur of the femoro-tibial joint of *O. sulcatus*

O.sulcatus	**all**	**pores**	**no pores**	**structure**	**lubricant**	**sapphire**
dried	0.13±0.04	0.34±0.14	0.11±0.04	0.18±0.08	1.21±0.19	0.15±0.01
fresh	0.16±0.11	0.30±0.14	0.12±0.09	0.20±0.21	0.13±0.09	0.15±0.03

5.2.3 Discussion of the coefficients of friction

The data being derived with the same cantilever under the same conditions allows us a hassle-free comparison of the features and beetles. A very nice connection of the datasets of the two beetles is the COF for the flat surface, the chitin. The COF are within limits of each other, reducing to an average COF of 0.11 for chitin. The structures are also comparable despite their differences, while the lubricant could not be more different. The lubricant found in the beetle *C. aurata* has the highest COF of all, being only topped by the dried lubricant of *O. sulcatus*, which increased over a tenfold during the evaporation process from a COF comparable to the one of chitin. A fact still puzzling is the closeness of the COF of the fresh lubricant of *O. sulcatus* to the COF of the cuticular surface of the dried joint as well as the high COF of the lubricant of *C. aurata*. This outcome leads us to the assumption, that lubricant might not be necessary to enhance the tribological properties concerning the reduction of the friction. Nevertheless, lubricant might have additional advantages and purposes, which might be still applicable to the joint of the beetle. Furthermore, the system as researched here is of course vastly different from the complete system as can be found in living beetles. Naturally, I tried to manipulate the system as little as possible and work as quickly as possible to preserve the natural features as good as possible, but the conditions in a lab will always compare poorly to the conditions in nature and a living subject.

If I compare our derived COF with the values from literature there are some similarities as well as differences. The first COF of the lubricant of *Z. morio* has been measured in a tribological setup between two glass slides, resulting in a COF of 0.13 [18]. Of course the setup of Nadein *et al.* and my intricate setup of friction force measurements in silicone oil are vastly different and make a direct comparison difficult. Nevertheless, my COF of the fresh lubricant of *O. sulcatus* averaged to the same value. This is however not what we expected. *C. aurata* was specifically chosen to allow me the comparison with older studies, being similar in size with both *Z. morio* and *P. marginata*. My COF of the lubricant in *C. aurata* averages to 0.37 being almost three times higher than the COF published in the previous study. If one considers the updated study of 2024 [19] the COF derived for the full femoro-tibial

joint of the two beetles lies at 0.00474 for *Z. morio*, which is unattainable with my COF even for *O. sulcatus*, the COF of *P. marginata* at 0.1055 is closer to my results, the overall scans of *C. aurata* average for the COF to roughly twice this value, while the ones for *O. sulcatus* exceed the value only slightly. The COF derived for the system of the femoral and tibial condyle with values for the COF below 0.03 are unfortunately again impossible to relate to my results, which I hoped to relate to the results of the COF for the chitin. It is important to emphasize the difficulty of the comparison of results derived with the AFM to the ones derived with the tribometer, due to the vast differences in force, contact area and velocity. The setup of my measurements in silicone oil further complicates this comparison and therefore the only viable comparison is between the results derived in this work.

6 Microstructures found on the coxa-trochanteral and femoro-tibial joints of *Otiorhynchus sulcatus* and their frictional anisotropic properties and functionality

A multitude of structures is presented in the figures of the beetle joints till this point. This chapter is dedicated to the detailed description of these structures. Multiple experiments were conducted to reveal the purpose of the structures.

This chapter includes research data which has been submitted for publication on June 4th, 2025:
Cornelia F. Pichler, Rafaela Debastiani, Matthias Mail, Jenny Hein, Elias Hamann, Tilo Baumbach, Hendrik Hölscher, and Thomas van de Kamp. *Multimodal characterisation of the femoro-tibial joint of the black vine weevil (*Otiorhynchus sulcatus*)*. Journal of the Royal Society Interface, 2025.

6.1 Microstructures found on the coxa and trochanter of the coxa-trochanteral joint of *Otiorhynchus sulcatus*

Structures are not only found in the so far described femoro-tibial joint of O. sulcatus, but in all other joints as well. Due to the intriguing morphological geometry of the coxa-trochanteral joint, it shall have its own section. In Figure 6.1 the coxa-trochanteral joint is shown. Figure 6.1 a) shows the screw and nut system, which is depicted in its natural and manipulation free state as observed with the μCT. A virtual cut was placed to remove half of the coxa to show the mechanics of the joint. The trochanter in yellow represents the screw, fitting tightly into the counterpart – the coxa (in pink) – with the help of a thread and a pocket keeping the tip of the screw in place. The tight fit should guarantee a reduced loss of haemolymph and lubricant as well as a reduced risk of contamination. In Figures 6.1 b)-d) the deconstructed parts of the coxa-trochanteral joint can be seen. Despite the tight fit of the system, the parts can sometimes be deconstructed without damage, which suggests that the material allows some elasticity to prevent damage and wear in at least one partner of the system. Figure 6.1 b) shows a SEM image of the coxa, showing the thread including microstructures like bristles, sawtooths, shingles and pores. Figure 6.1 c) shows a focus-stacking image of the trochanter recorded with the light microscope (Axioscope 7, Zeiss, Germany). Figure 6.1 d) shows a trochanter as seen with the SEM. The insets show the microstructures found on the trochanter: sawtooths in the thread and shingles on the convex surface.

The sawtooth structures, which are arranged in a shingle fashion (visible in the inset in Fig. 6.1 d)) have been used as the basis for the 3D-printed test structures as described in Section 3.2. Their functional properties will be discussed below.

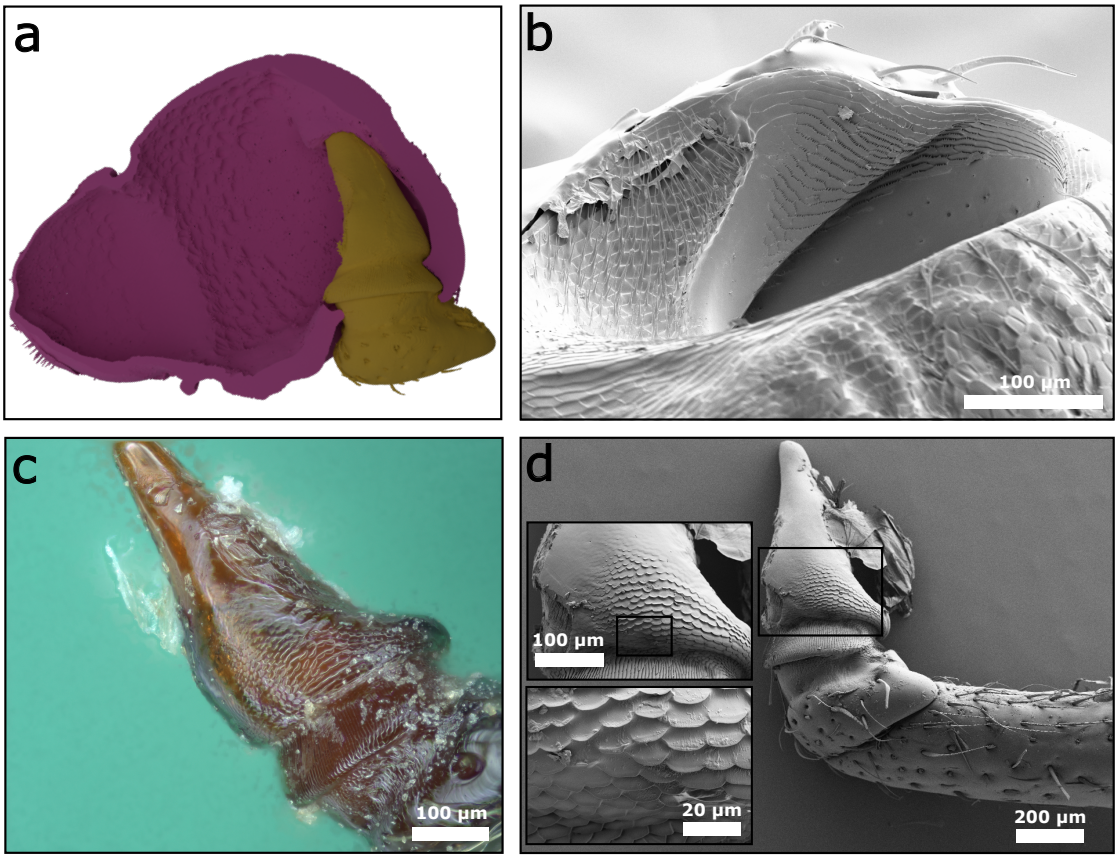

Figure 6.1: a) A 3D-rendering of the coxa-trochanteral joint of *O. sulcatus* scanned in detail with the μCT. A strategic virtual cut opens up the coxa (in pink) to showcase the fascinating screw and nut morphology of the joint. The screw part of this system is the trochanter (in yellow), while the coxa shows a form closure around the trochanter reminiscent of a nut. The tip of the trochanter screw is sunk-in into a pocket formed by the coxa and the thread of the screw is tightly covered by the coxa, allowing for a reduced loss of haemolymph and lubricant. b) An SEM image showing the inside of the thread of a coxa. Microstructures include bristles, shingle-like structures and pores. c) A microscopic image of the trochanter obtained with focusstacking. d) A SEM image of the trochanter. The insets show the microstructures found on the trochanter. Sawtooth structures are covering the thread and shingle-like structures are on the convex surface of the screw. The shingle-like structures found are used as a basis for the 3D-printed structures with the Nanoscribe System.

6.2 Microstructures found on the femur and tibia of the femoro-tibial joint of *Otiorhynchus sulcatus*

I observed a variety of different microstructures on the cuticular surface within the femoro-tibial joints of the examined beetles. In Figure 6.2 SEM images of the dissected femur of the femoro-tibial joint of *O. sulcatus* are shown. The overview image in the middle is surrounded by zoomed-in images showing the microstructures in more detail. The image to the left shows a simple cuticular structure based on sawtooth structures in a hexagonal and parallel arrangement next to the flat area hosting the pores. The sawteeth merge at different points, which are called anastomoses [59]. To the right two similar structures are presented. Both show an imbricate sawtooth structure with denticles on concave surfaces, but the arrangement of the structures varies. The structures in the upper right are arranged in a parallel fashion while the lower right shows the structures arranged as scales in an almost isodiametric fashion. The location of the most accessible pores on the femur of the femoro-tibial joint are marked with a green crescent. In the marked area, FIB and nanoCT measurements were performed on separate samples since the FIB is a destructive method and the nanoCT requires a smaller sample area and therefore has to be cut beforehand.

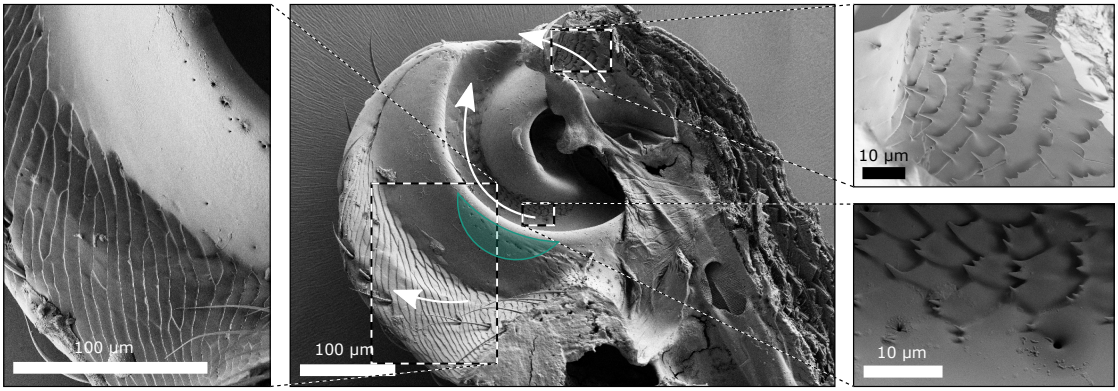

Figure 6.2: In the middle, an overview image with the SEM of the dissected femur of *O. sulcatus* is plotted, the zoom-ins to the left and right show different cuticular structures found in the femur. To the left a simple slightly imbricate sawtooth structure with anastomoses is depicted next to the flat and unstructured main frictional surface. To the right two similar structures on a concave surface are shown. Both are based on the sawtooth structure and show denticles. The upper right structures are parallelly aligned, while the lower right structures are formed into an arrangement similar to isodiametric scales. The green crescent highlights the pores found on the flat surface on the femur. The white arrows in the overview picture indicate the path trapped particles would take, assuming a frictional anisotropy of the structures. The arrows point in the direction of the lower coefficient of friction.

The tibia part of the femoro-tibial joint exhibits a multitude of cuticular surface microstructures (Fig. 6.3), covering all surfaces. The surface, which is found if you turn the tibia as depicted in the overview image in the middle by 90° from the left to the right, is covered by a structure reminiscent to the one found on the femur (Fig. 6.2 lower right): an imbricate scale-like structure with denticles on a slightly concave surface (Fig. 6.3 upper left). A similar pattern can also be found in the lower right corner, where it is covering a convex surface. The convex surface transitions into a concave surface towards the middle, where the denticles of the structures evolve into longer bristles in a hand-like fashion. The remaining surfaces are covered by sawtooth structures with anastomoses on a convex (lower left) and flat (upper right) surface, respectively.

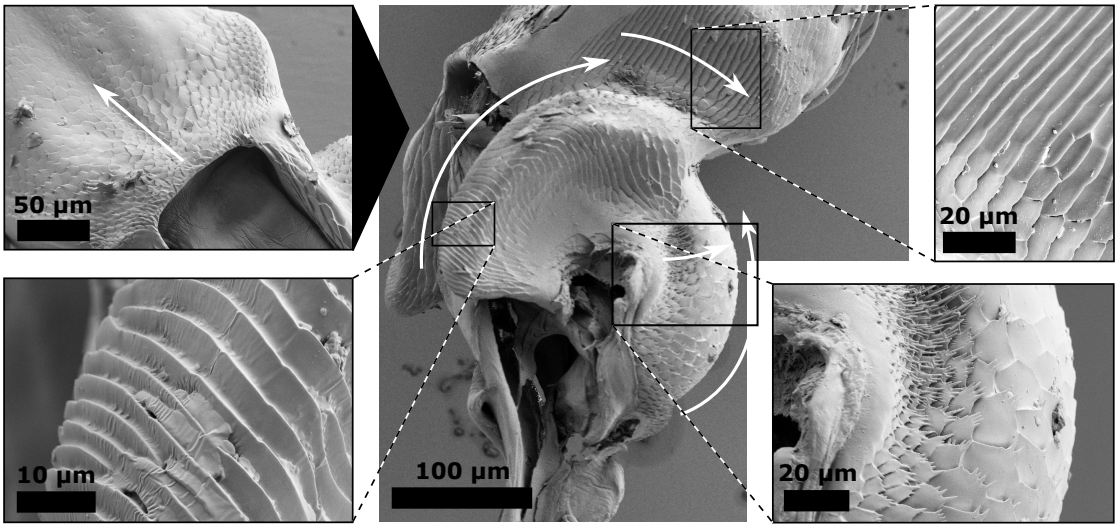

Figure 6.3: In the middle an overview image with the SEM of the tibia of *O. sulcatus* is depicted. The Zoom-ins show the structures, which are present in the tibia. The upper left corner is occupied by the structures which can be found on the side of the tibia as depicted in the overview image. The image in the upper left can be obtained, by turning the tibia 90° from the left to the right. The structures are reminiscent of the structures found in Figure 6.2 in the lower right corner. The denticles on a scale-like slightly imbricate structure based on sawtooth structures presumably lead the particles in the direction of the white arrow. The lower left image as well as the upper right image show a simple sawtooth structure with anastomoses. While the lower left structure is located on a convex surface, the upper right surface hosting the sawtooth structure is flat or slightly concave. The lower right image shows the most interesting structure.The denticles in a scale arrangement based on sawtooth structures found on the convex surfaces evolve into longer bristles reminiscent of hands in the concave area. The white arrows in the overview picture are guides to the eye pointing in the direction the particle would travel based on the lower coefficient of friction assuming frictional anisotropy.

Due to the interlocking fashion of the joint, different structured surfaces are in contact with each other. The parallelly arranged sawtooth structure with denticles of the femur (Fig. 6.2 upper right) is in constant contact with the imbricate sawtooth structures in a isodiametric fashion as scales with denticles of the tibia (Fig. 6.3 lower right). The latter structures found also in the femoral concavity (Fig. 6.2 lower right) are in constant contact with the structures of the tibial condyle, which hooks into the femoral concavity. The tibial condyle is covered in a basic sawtooth structure with anastomoses (Fig. 6.3 lower left). The unstructured main frictional surface of the femur hosting the high density arrangment of the pores is in contact with the flat tibial frictional surface covered with a basic sawtooth

structure with anastomoses of the tibia (Fig. 6.3 upper right). The sawtooth structures on the outer rim of the crescent surface of the femoral frictional surface (Fig. 6.2 left) are in contact with the exocuticular surface of the tibia, not being part of the joint system. The hand-like structures in the tibial concavity (Fig. 6.3 lower right) are in contact with the unstructured femoral condyle. The slightly imbricate scale-like sawtooth structures with denticles on the tibia (Fig. 6.3 upper left) are in contact with the hair on the femur found closest to the body of the beetle.

6.3 Anisotropy of selected microstructures as found on the trochanter of the coxa-trochanteral joint of *Otiorhynchus sulcatus* with FFM

The most commonly found microstructures in arthropods are polygonal/isodiametric structuring, which can be flat or imbricate acting as scales or scutes [59] [60] [61] [62] [63] [64]. These structures may specialize [59] [65] [66]. The purpose of cuticular microstructures is widespread, reaching from surface coloration to body cleaning to friction-related purposes [9] [38] [67] [68] [69]. Adherent to the cuticular microstructures described in the review of Watson, Watson and Cribb [70], our structures fit best in the category of "Wear and friction control/food grinding/sound generation/body cleaning (mechanical gears)" represented in the review by scales. The structures can develop from sawtooth structures to denticles to bristles [61] [65] [67] , which can also be seen in stridulatory organs on the cuticula of for example leaf beetles [66] [71] [72].

With the sawtooth structures uniting all found structures as the most common feature, the purpose of these structures seems quite clear. Sawtooth structures are known to show frictional anisotropy. The common feature of the sawtooth structure resembles the much smaller similar structuring of the scales of the well-researched sandfish (*Scincus scincus*), where it is associated with frictional anisotropy [73] [74]. The sandfish is showcasing fascinating attributes based on the sawtooth microstructures on its scales and the unidirectional transport of particles due to the frictional anisotropy, meaning a lower friction in the direction of the sawteeth and a higher friction against the structure.

As frictional anisotropy is a reoccurring effect often present in nature also known from ants and snakes [75] [76] [77] [78], I assume a similar functionality in my studied system. The sawtooth structures found on the scales of some snakes and the sandfish are of sub-μm height, while the structures described in this study have a height of 1-2 μm. The simple sawtooth structures described above are closer to the structures found on the sandfish, which are simple gradient steps with frayed edges. The sawtooth structures decorated with denticles and small hand-like structures are more reminiscent of the structures found for example on the Chinese cobra (*Naja atra*), which form small finger-like structures on sawtooths. The increased height of the presented structures may be required to ensure the functionality of the particle transport between two moving structured surfaces.

If one indicates the direction of the lower COF in the Figures 6.2 and 6.3 with arrows, one can imagine the path of trapped particles out of the joint. Nevertheless, the first step is to clarify the frictional anisotropy of those structures.

My first samples of simple sawtooth structures were fabricated with the FIB as described in Section 3.7, showing various heights between ten to one hundred nm and two different periods of three and six μm. For readers following closely along this thesis, a clear problem becomes apparent quickly. The sawtooth structures resemble the wedge described in Section 2.1 and used in the calibration method described in Section 3.4.1. The offset arising from the angle of the slope the cantilever has to climb makes it impossible to arrive at a consistent and reliable analysis.

Due to the convex and concave geometries of the joint a frictional analysis on the microstructuring of the beetle joints was prone to crosstalk and manipulation. Therefore, I recreated the simple structure found on the different joints of the beetles on a flat surface and fabricated them with the Nanoscribe system (Sec. 3.2). The shingle structures on the convex surface in Figure 6.1 d) have been used for the design of the 3D-printed test samples, showing the common sawtooth structures being the basis for all microstructures in the joint and combining the scale-like and parallel arrangement of many structures. The bristles are difficult to fabricate and are prone to damage the cantilever or take damage in the friction force measurements. Therefore, I did not replicate any microstructures with denticles. In order to see the evolution of the structures and maybe improve the structures, I introduced small variations in periodicity of the sawtoothstep (constant or increasing period), width of the scales (constant or increasing width) and shift of the scales for each sawtoothstep (See Fig. 6.4 and Tab. 6.1). Due to the possible shift in the scales, the actual periodicity and width of the steps is difficult to measure without confusion so I only marked the two options in the table to highlight the variances for a better comparability.

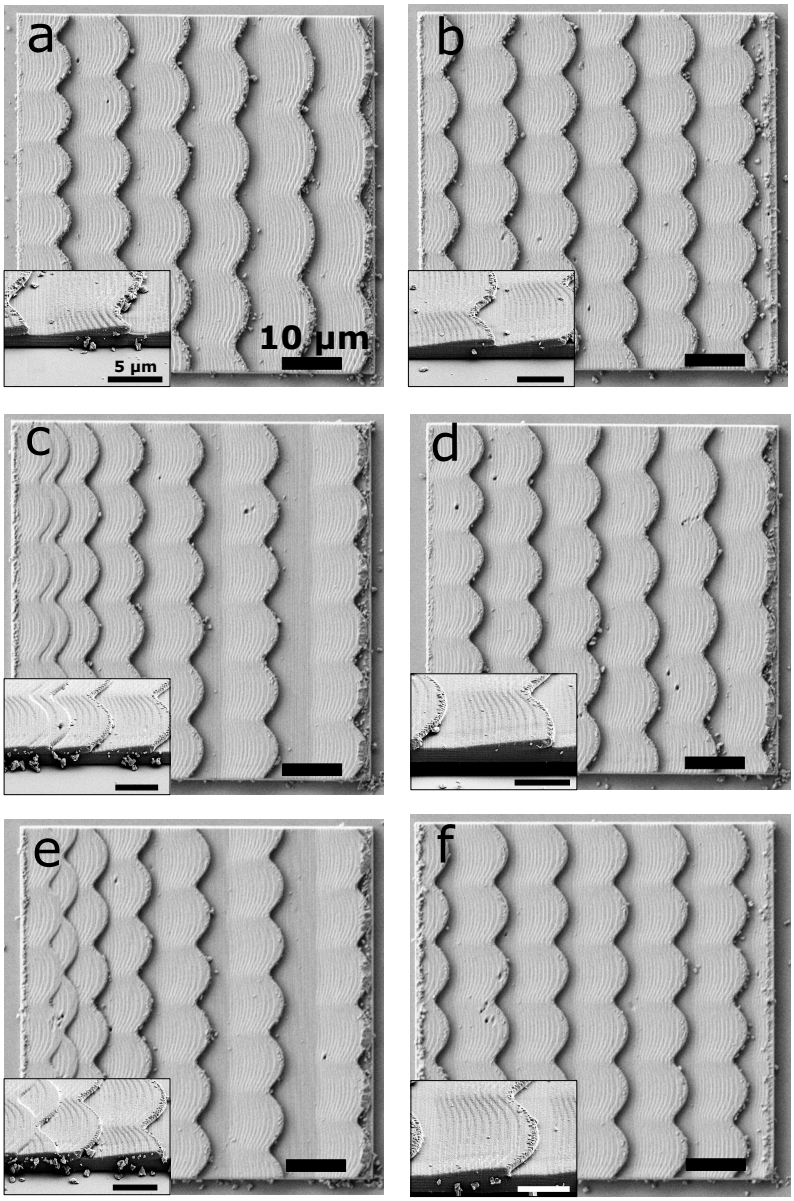

Figure 6.4: The six 3D-printed test structures inspired by the structures found in the joint of the beetle *O. sulcatus*. The letters correspond to the labeling in the measurements. The insets show the side profile of the structures. The scale bars of the images are 10 μm, while the ones in the insets are 5 μm

The COF recorded with the FlexFM of the structures show no big surprises. The COF recorded with the colloidal probe are higher than the one with the sharp tip, due to the difference in the size of the contact surface. The smallest COF can be seen in test structure **e** with the sharp tip, while the highest COF can be recorded for test structure **f** with the colloidal

tip. Interestingly test structure **a**, which is most closely modeled after the structures found on the trochanter, show the highest COF of all structures when measured with the sharp tip, while it also shows the lowest COF when measured with the colloidal probe.

Table 6.1: The six 3D-printed test structures inspired by the structures found in the coxa-trochanteral joint of the beetle *O. sulcatus* with their properties and COF measured with a sharp tip and colloidal tip (diameter of the glass sphere was approximately 20 μm). The letters correspond to the labels in Figure 6.4.

	a	**b**	**c**	**d**	**e**	**f**
periodicity	constant	constant	gradient	constant	gradient	constant
width	gradient	constant	constant	gradient	constant	constant
shift	no	yes	no	yes	yes	no
sharp tip	0.26±0.01	0.23±0.01	0.21±0.004	0.21±0.01	0.19±0.01	0.21±0.02
colloidal tip	0.52±0.03	0.58±0.04	0.56±0.02	0.55±0.02	0.55±0.02	0.59±0.03

Despite the visual friction loops of anisotropic structures on samples being quite clear (see Fig. 6.5), the actual analysis proves difficult. For structures measured with colloidal probes the frictional anistropy is even visually hard to make out, here a clear analysis to determine if the anisotropy is still apparent for colloidal probes would be needed. The friction loop is most of the time disturbed by an offset and never centered accurately around the origin. Our first approach to solve this problem was to include a flat surface in the measurements of the structures. The mean of the part of the friction loop of the flat surface could then be used as a reference, showing a clear frictional anisotropy.

The difficulties described above aries in the more complex structures of the roof shindles as well. In Figure 6.5 a) the topography of test structure **a** as scanned with a sharp tip can be seen. In this image, two arrows are included indicating the direction of trace (blue) and retrace (orange) and the corresponding friction loop of this line is depicted below. The peaks of the retrace in orange of the cantilever moving against the sawtooth structure are higher than the peaks of the trace in blue. This would be a clear sign for frictional anisotropy, which we can discern quite intuitively. If one scans the same structure with a colloidal probe with an increased contact surface, simulating a system more closely related to the particles and opposing frictional surface in the joint system of the beetle, the image changes. Naturally, the topography as scanned with the colloidal probe (Fig. 6.5 b)) shows some influence from the geometry of the cantilever tip. The sphere attached to the cantilever does not reach the valleys of the structures and stays in contact with the edges of the structure for longer due to the spherical nature "rolling" over the edge. This gives the topography a bubbly appearance. The friction loop as seen below also changes its appearance. The frictional anisotropy is not intuitively clear anymore and we would need a new analysis method to decide, if there still is a frictional anisotropy present. Our initial idea of scanning a flat surface next to the

sample to counterfeit the instrument specific offset, leads to a problem. In the friction loop of Figure 6.5 b) the mean of the flat surface is plotted with a dashed line. Using this line as a reference to determine the friction of the two directions, would lead to negative friction for the retrace data, due to the crossings of the line. For smaller load, this line can lie entirely above the friction loop of the structure, making a determination of COF for the separate directions inconclusive. This method therefore is not applicable to determine the frictional anisotropy of microstructures in a semi-automated analytical way.

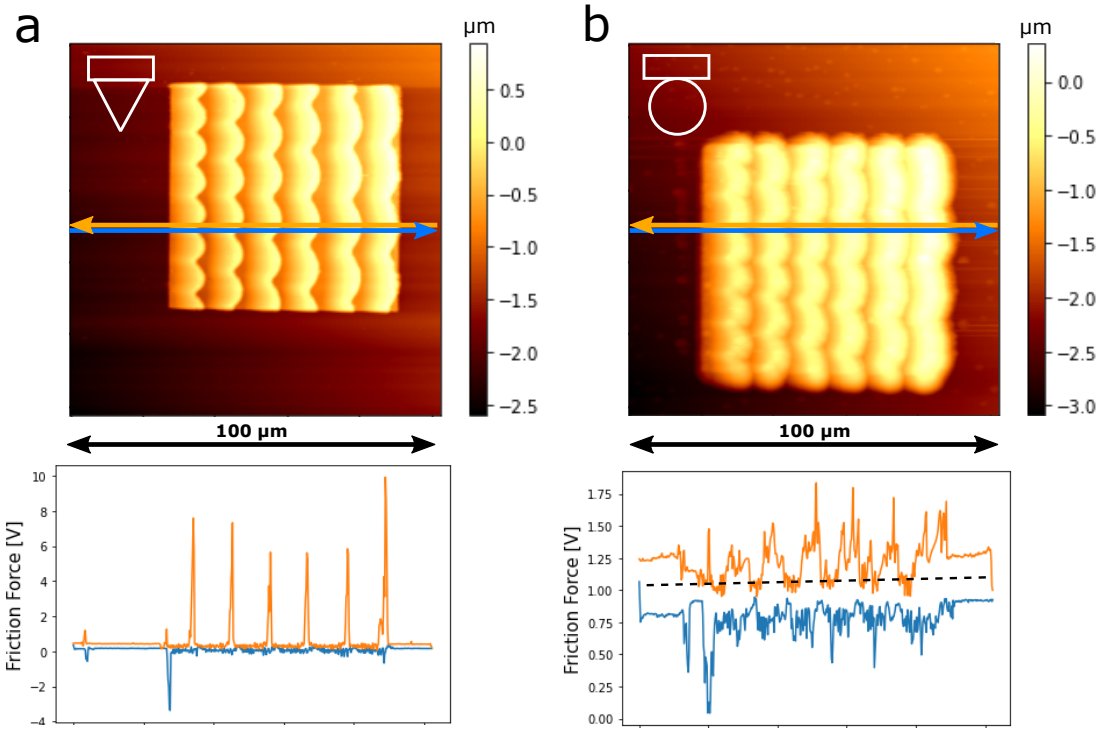

Figure 6.5: a) The AFM topography image of the 3D-printed sample **a** with a sharp tip and a friction loop at a deflection setpoint of 5 V below showing a striking frictional anisotropy. b) The AFM topography image of the 3D-printed sample **a** with a colloidal tip and a friction loop at a deflection setpoint of 5 V below making the problematic offset, being attributed to the wedge like structures, apparent. If one imagines a line indicating the mean of trace and retrace of the surrounding flat surface, the retrace of the structures would show negative friction. For smaller loads this line can lie entirely above the friction loop, making an analysis of seperate COF for the directions inconclusive.

6.4 Selfcleaning of the femoro-tibial joint of *Otiorhynchus sulcatus* by particle transport according to the anisotropy of the microstructures

Despite my unsucessful attempts above to analyze the anisotropy of the beetle structures with a sharp and colloidal tip in a reliable analytical way, the peaks in the measurements with the sharp tip argue for an existing anisotropy. This anisotropy would affect small dirt particles in the joint, while the missing anisotropy in the measurements with the colloidal tip should be favorable to the movement of the beetle. The beetle would struggle to move smoothly and would risk damage to its joints if the anisotropy would be noticeable for the large joint partners. Additionally, the previously discussed studies are showing anisotropy on natural sawtooth structure to further support our next claims.

With the supported claim of frictional anisotropy, white arrows, pointing in the direction of the lower COF, were added to the overview picture of the tibia (Fig. 6.3) and femur (Fig. 6.2). All arrows point in the same direction, especially on opposing surfaces highlighting the path a trapped particle in the joint would take. The structures are supposedly guiding the trapped particles to the outside, while also preventing the particles to move towards the delicate entrails of the beetle. The movement of the legs enables the particle transport in the intended direction by the structures and it might need multiple cycles for the particle to leave the joint. The same process also supposedly distributes the lubricant from the pores to the rest of the joint explaining the high density of the pore openings towards the body together with the tight fit of this specific frictional surface.

In order to visualize the procedure, I created an animation based on μCT data describing the direction of the particle transport [2] and two further animations show the putative path of the particles leaving the joint at the bottom [3] and at the top [4].

In three theoretical studies contradicting results are presented, one of them [24] claiming the semi-solid lubricant forming cylindrical logs functioning as a rolling bearing due to the microstructures, while the other two [25] [26] contradict these findings by claiming the formation of lubricant clots. Due to the tight fit of the two opposing surfaces, our hypothesis of an even distribution of the lubricant through the microstructures fits better with later results.

In one study [22], an anti-wear nature of the lubricant is hypothesized, engulfing sharp-edged particles before transporting them outside. This mentioned transport would fit well to the alignment of the structures, and would also explain the transport of the lubricant to the particles encasing the particles during the movement of the beetle, while already transporting the particle to the outside.

[2] https://doi.org/10.5445/IR/1000183064
[3] https://doi.org/10.5445/IR/1000183065
[4] https://doi.org/10.5445/IR/1000183066

As mentioned in the introduction, arthropods and technology share the challenges, which come with the use of an open system. The mechanical labyrinth seal in technology, which is using structures to restrain the lubricant (to the inside of the bearing), shows some similarities to microstructures found in the joint of insects [4]. These seals might be improved with the information gathered here.

7 The network supplying the lubricant to the frictional surface in the femoro-tibial joint of *Otiorhynchus sulcatus*

The thesis has presented so far the aging, the tribological properties and the distribution of the lubricant in *O. sulcatus*. This section provides a look into the origin of the lubricant, which has been made possible with complementing methods, since the dimensions of the pore canals are at the limits of multiple techniques – too narrow for the μCT and too long for the nanoCT and FIB.

This chapter includes research data which has been submitted for publication on June 4th, 2025:
Cornelia F. Pichler, Rafaela Debastiani, Matthias Mail, Jenny Hein, Elias Hamann, Tilo Baumbach, Hendrik Hölscher, and Thomas van de Kamp. *Multimodal characterisation of the femoro-tibial joint of the black vine weevil (*Otiorhynchus sulcatus*)*. Journal of the Royal Society Interface, 2025.

7.1 The discovery of two types of pore canals ending in the frictional surface of the femoro-tibial joint

The μCT data of the femoro-tibial joint shows two types of pore canals[5] connecting the haemocoel to the frictional surfaces of the joint. Bigger canals (Fig. 7.1 a)), indicated with white arrows) presumably do not open into the joint. The smaller canals (Fig. 7.1 b)), indicated with a white arrow) are at the limit of the resolution of the μCT and can therefore only be faintly recognized (Fig. 7.1 c)). Both types of canals are located only in the femur part of the joint. The structures described in the previous section can also be adumbrated in Figure 7.1 a), indicated with black arrows.

[5]The author of this work is aware that the term pore canal has a very specific biological definition needing to fulfill certain criteria. Nevertheless, for the sake of clarity and lack of a better denotation, the discovered network beneath the frictional surface is described with the generic meaning of the term “pore canal”, describing in this work the simple combination of a pore opening and a canal of varied thickness. In this fashion an unbiased description is possible without deciding the function of the found pore canal.

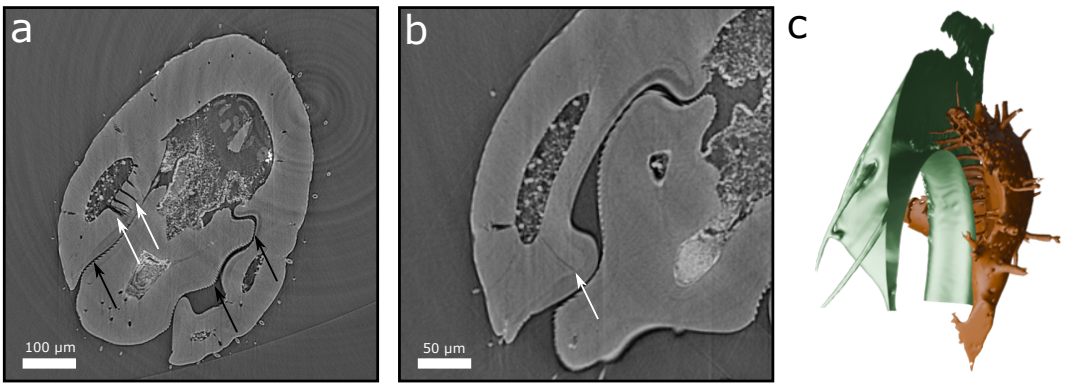

Figure 7.1: µCT images showcasing a) bigger and b) narrow pore canals connecting the frictional surface in the femur (white arrows) to the haemocoel as well as the microstructures described above indicated with black arrows c) a 3D-rendering of the frictional surface of the femur (green) and the haemocoel with connected pore canals (brown), the chitin matrix material is transparent in this image in order to not obstruct the view of the pore canals.

In order to get a clearer picture of the inner workings and the different kind of pore canals some additional high-resolution measurements were performed with the FIB and nanoCT. Both FIB and nanoCT show comparable data (Fig. 7.2, 7.3). Clearly observable are two kinds of pore canals. Bottleneck pore canals (bpc) are thicker pore canals originating from the haemocoel and ending in a bottleneck shape on the frictional surface. Narrow pore canals (npc) are very narrow pore canals ending in the frictional surface with the origin extending outside of the reasonably examinable volume of FIB and nanoCT measurements.

The nanoCT data of a chemically dried sample shows two bpc (Fig. 7.2 a)) ending in the frictional surface of the femur in the femoro-tibial joint. Below the clear opening to the surface, a white feature is seen. This is the beginning of the discontinuity between the pore opening and the wider pore canal, which is bridged by a collection of white holes or voids. The nanoCT data also showcases a npc (Fig. 7.2 b)), ending in the frictional surface of the femur. In the FIB data (Fig. 7.2 c), d)) the bpc are located next to the npc. The bpc are again composed of a pore opening in the frictional surface surrounded by voids connected over an extended duct canal with the haemocoel. The 3D-renderings (Fig. 7.3) of the full segmentation surface data in both nanoCT and FIB scans showcase the disordered arrangement of the network of the pore canals. The npc can be found both closer and further to the femoral concavity as well as in line with and located directly next to the bpc, making it impossible to differentiate between them from the outside. The green material represents the frictional surface, while the brown one shows the walls of the pore canals, haemocoel, and voids. For better visibility of the pore canals, this representation was chosen to not obstruct the view by the cuticle. Figure 7.3 a) shows the 3D-renderings of two combined

data sets of the chemically dried sample. The CPD sample is shown as a 3D-rendering of four combined data sets in Figure 7.3 b). Figures 7.3 d), e) and f) show 3D-renderings of three separate FIB datasets.

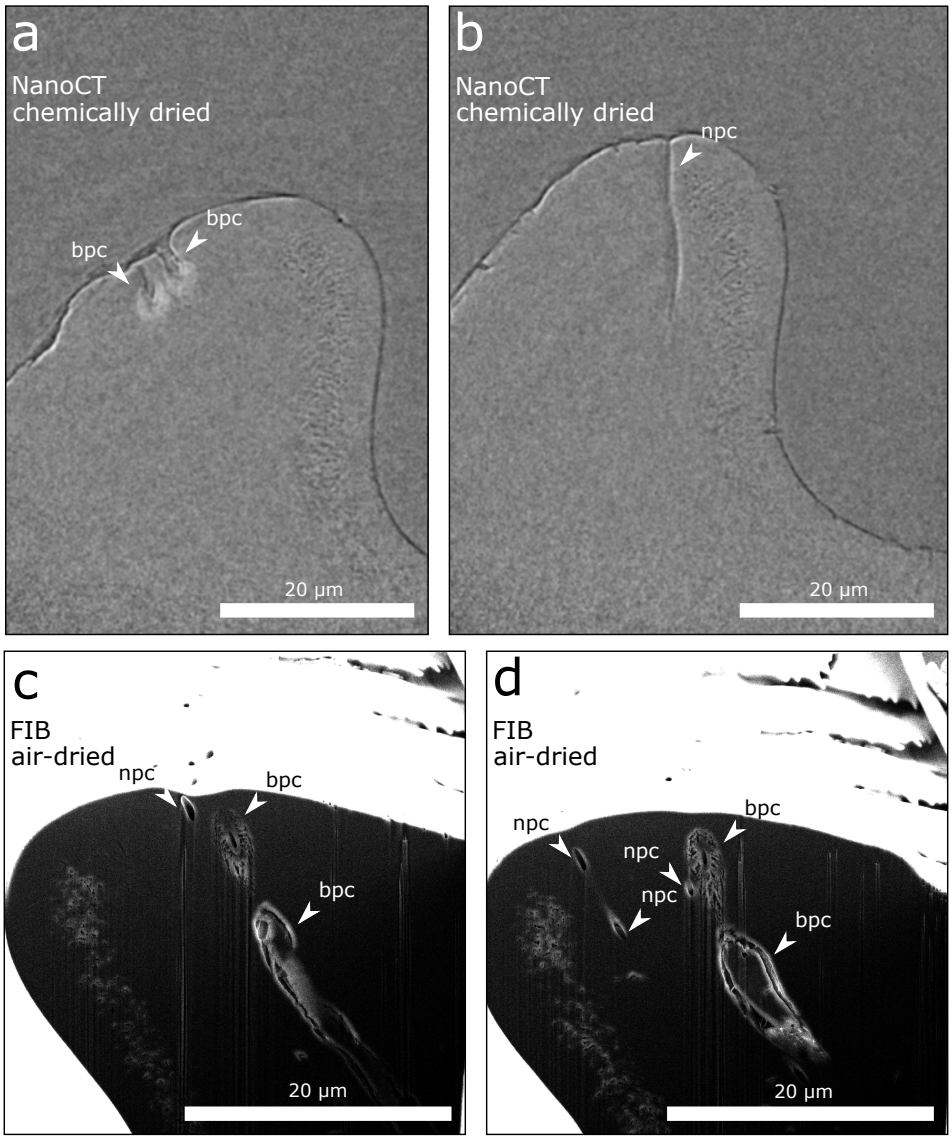

Figure 7.2: Comparison of nanoCT (chemically dried sample) and FIB Slices (air-dried sample) a) nanoCT slice of two bpc ending in the frictional surface of the femur b) nanoCT slice of a npc ending in the frictional surface of the femur c) FIB slice of a combination of a bpc and a npc. The pore canal below the frictional surface of the femur is surrounded by a collection of voids, which might have been occupied before the air-drying process. d) FIB slice with a longer npc as well as the collection of the voids around the bpc connecting to the haemocoel. bpc – bottleneck pore canals; npc – narrow pore canals

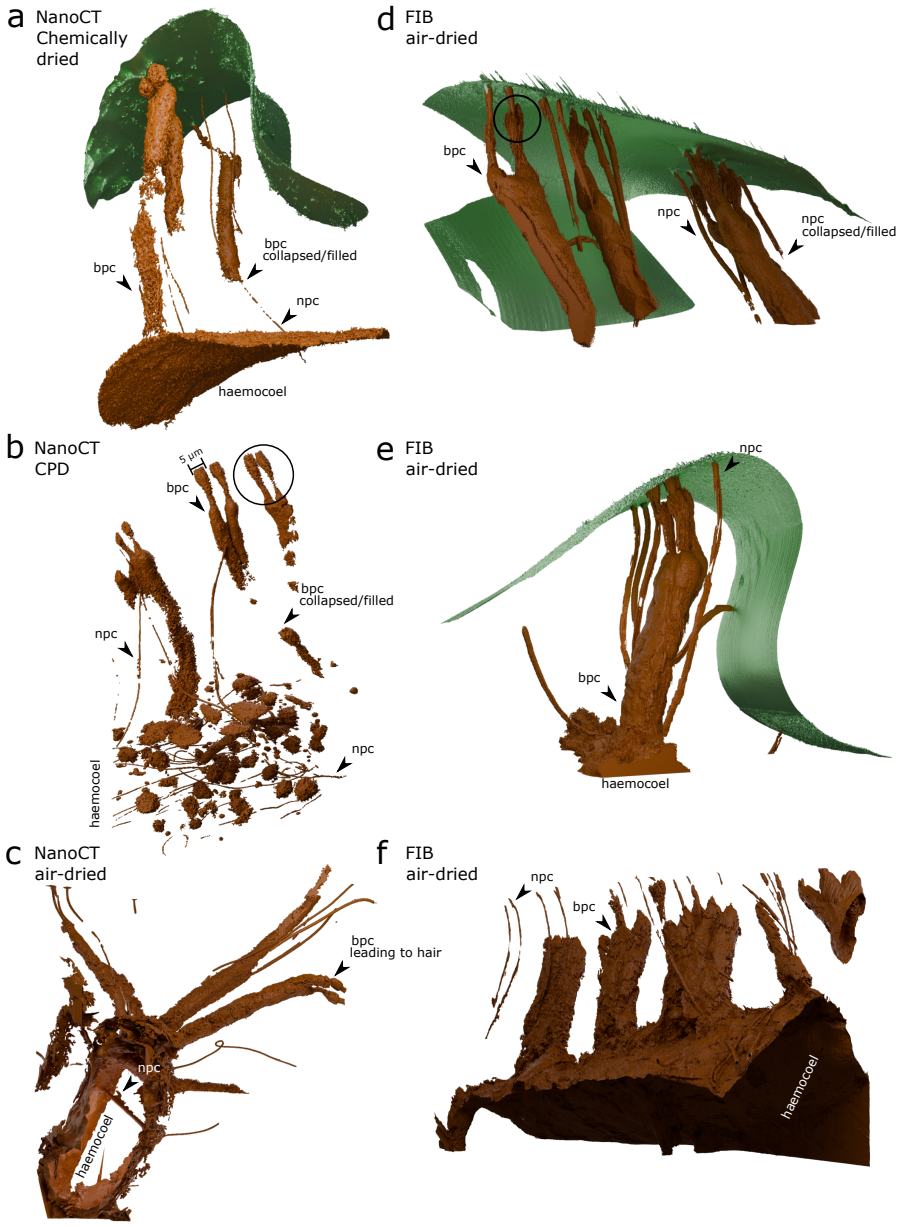

Figure 7.3: Comparison of the 3D-renderings (perspective view) of the nanoCT and FIB data sets. a) nanoCT data of chemically dried sample including the frictional surface b) nanoCT data of CPD sample excluding the frictional surface and walls of the haemocoel c) nanoCT data set of the air-dried sample with a collection of bpc and npc, the highlights being the looping in one of the npc, as well as the free-standing npc crossing through the haemocoel d) FIB data with many pore canals but incomplete frictional surface e) second FIB data set with complete frictional surface e) third FIB data set without frictional surface but haemocoel. bpc – bottleneck pore canal; npc – narrow pore canal

In Figure 7.3 b), the wall of the haemocoel and the frictional surface was removed, to facilitate the view of the network of pore canals through the haemocoel as well as the remaining collection of voids.

The nanoCT dataset of the air-dried sample features some peculiarities. Figure 7.3 c) shows the 3D-rendering of five combined datasets of the air-dried sample. Multiple npc run parallel to and on the outside of the haemocoel, but do not merge with it. Another interesting feature visible is the looping of one of the npc. Another curiosity is the crossing of a npc through the haemocoel. Due to the destructive nature of the method, crossings like this were not observable with the FIB. This dataset also includes a seta found on the exterior of the beetle, which is also connected to the haemocoel by a bpc splitting into three seperate bottlenecks opening up to the outside at two points around the seta and one connecting to the seta. To focus on the pore canals the frictional surface and the seta were virtually removed.

7.2 Discussion of the purpose of the discovered pore canals

Pore canals and dermal gland ducts can be found throughout the exoskeleton of arthropods [60] [67] [79] [80] [81] [82] [83] [64] [84] [85] [86] [87] [88]. Sometimes these pores are modified for a special purpose [89] or host a mechanoreceptor connected to sensilla [90] [91] [92]. A pore network throughout the joints of insects supplying lubricant has been first mentioned in [9] and [38]. Pore canals extruding wax on the surface of the insect host wax filaments [64] [85].

Neither the npc nor the bpc show a helical nature as wax canals do (Fig. 7.2, 7.3, 7.4). The FIB data of helical wax canals in the planthopper *N. lugens* reported by Li *et al.* [84] bear no resemblance to the data of our pore canals, I therefore conclude that neither of my presented pores are wax canals. While the npc show resemblance to the single pore canal of *Z. morio* showcased in the original publication of Nadein *et al.* [18], the bpc show some resemblance to the FIB tomographies of the mechanosensitive cells surrounding the setulae found on the hemelytra of *Notonecta glauca* and *maculata* [92]. Even though no hair can be found on the frictional surface close to the pores, the resemblance to a sensory duct is given. The classification of the two discovered pore canals proves difficult. In general, the lubrication of insect's joints is attributed to an uncontrolled release, set free slow and continuous [82]. In the case of the bpc being a mechanoreceptor, I assume that this release behavior would change.

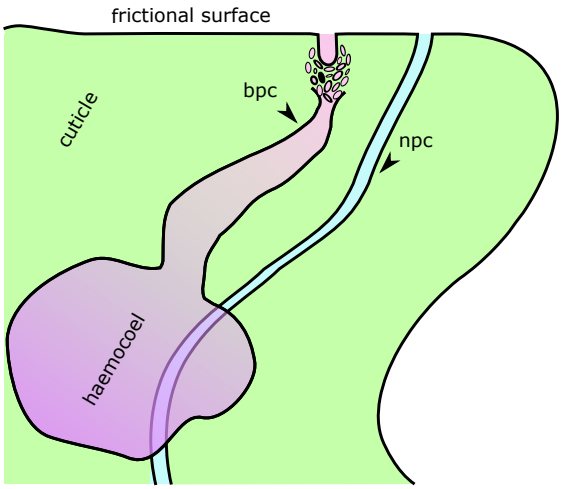

Figure 7.4: Drawing of the two pore canals in a cross section of the cuticle below the frictional surface of the femur of the femoro-tibial joint. bpc – bottleneck pore canal; npc – narrow pore canal

The npc is undivided with very limited change in the diameter crossing through the haemocoel or running along the haemocoel. Their origin is so far unknown. The npc are apparently not connected with each other. The bpc originate in the haemocoel reduce in size towards the surface, sometimes splitting in multiple pore canals never reaching the surface directly. The pores associated to the bpc are separated from them by a series of small voids. It is likely that these were originally inhabited by cell clusters, which are lost in the drying process. The details of the missing connection of the npc and the separation of the bpc to their pores by cell/air inclusions can only be seen with the nanoCT and FIB. The purpose of the pore canals, or rather, the pore canal responsible for the lubricant production and distribution is still not fully understood.

A serious drawback of both techniques is the inability to analyse samples in fluid. For the FIB, I used an air-dried sample sputtered with gold in the hopes of finding lubricant traces in order to assign a purpose to the pore canals. As described above the lubricant dries out in a short amount of time and cannot be found on older air-dried samples. The next drawback of the FIB is the destruction of the sample and any freestanding structures without preparing the sample accordingly.

Due to the preparation method of drying the samples for the nanoCT in different ways and cutting manually with a scalpel, many of the npc as well as some of the bpc have collapsed, preventing us to distinguish them from the surrounding cuticle material. Therefore, none of the samples show the same levels of preservation as obtained with an in ethanol scanned sample in the μCT. Currently, these are the only methods suitable for these samples in this resolution. Nevertheless, the combination of these three techniques gives us a well-rounded picture of the two types of pore canals, which can be found below the frictional surface in the femur of the femoro-tibial joint.

The canals discovered by nanoCT and FIB measurements are not part of the tracheal system, as the obtained μCT data of the leg of *O. sulcatus* clearly shows tracheae and bigger tracheoles in the rest of the femur and tibia with no connection to the area of the pore canal network below the frictional surface of the joint (See Fig. 7.5). The μCT and synchrotron X-ray imaging have been chosen as suitable technologies in earlier studies to determine the tracheal system for a multitude of insect specimen [93] [94] [95] [96] [97].

Figure 7.5: The segmented tracheae in the leg of the weevil *O. sulcatus* determined by the μCT data. The tracheae and tracheoles thread the whole beetle to supply every component with oxygen. The tracheae and bigger tracheoles found inside the leg have been segmented and plotted in black. This work shows the missing connection between the pores found in the femur ending in the femoro-tibial joint and the tracheal system. This reveals the interplay of the pores with the oxygen supply. As can be seen in this image, the network of tracheoles end far from the joint, allowing only one thick trachea to traverse the joint to supply oxygen to the tibia and beyond. The colorscheme is the same as in the previous images and all parts are cut open to allow an unobstructed view of the tracheal network.

The μCT images lead us to the assumption, that the pores might be supplied with haemolymph from the beetle. Consequently, it is likely that the lubricant is chemically based on or transported by hemolymph. This claim is supported by the fact, that some insects, such as ladybird beetles, extrude hemolymph from the femoro-tibial joint when attacked [65] [98].

8 Chemical analysis of the haemolymph and lubricant of *Otiorhynchus salicicola*

The only missing component to completely analyze the tribological lubrication system of the weevil *O. sulcatus* in this thesis is the composition of the lubricant. In order to give myself the best available starting conditions, I switched from *O. sulcatus* to *O. salicicola*, the slightly bigger beetle, to obtain more lubricant and haemolymph for analysis. This section is dedicated to the chemical analysis of the lubricant, complete with a successful analysis of the haemolymph and a roadmap to all applied techniques for a first rudimentary analysis of the lubricant.

As was already described in Section 2.2 a rudimentary analysis of the lubricant found in *Z. morio* was performed with an ATR-FTIR system. The detailed analysis spectrum can be found in [18]. Unfortunately, the only information Nadein and his colleagues read out of the spectrum is the fact, that the lubricant is protein-based.

8.1 Chemical analysis of the haemolymph of *Otiorhynchus salicicola*

Since our first assumption is, that *O. sulcatus* and *O. salicicola* reuse an already existing fluid in their body to lubricate their joints, we analyzed haemolymph with standard methods. To ensure the best comparison between the haemolymph composition and the lubricant composition, we analyzed the haemolymph with three methods, I hoped to use for the lubricant analysis. I extracted fresh haemolymph from anasthesized *O. salicicola* with a syringe. The haemolymph was analyzed (with the kind help and support of Patrick Hodapp (KIT)) pure directly after extraction with the ATR-FTIR and IR-Raman and diluted in destilled water with liquid chromatography high resolution mass spectrometry (LC-HRMS) (see Fig. 8.1). Comparing the ATR-FTIR spectra with the spectra of the dried lubricant in [18], the similarity is striking. Even more so, when one subtracts the spectrum of water. This leads to the assumption that the lubricant is haemolymph-based.

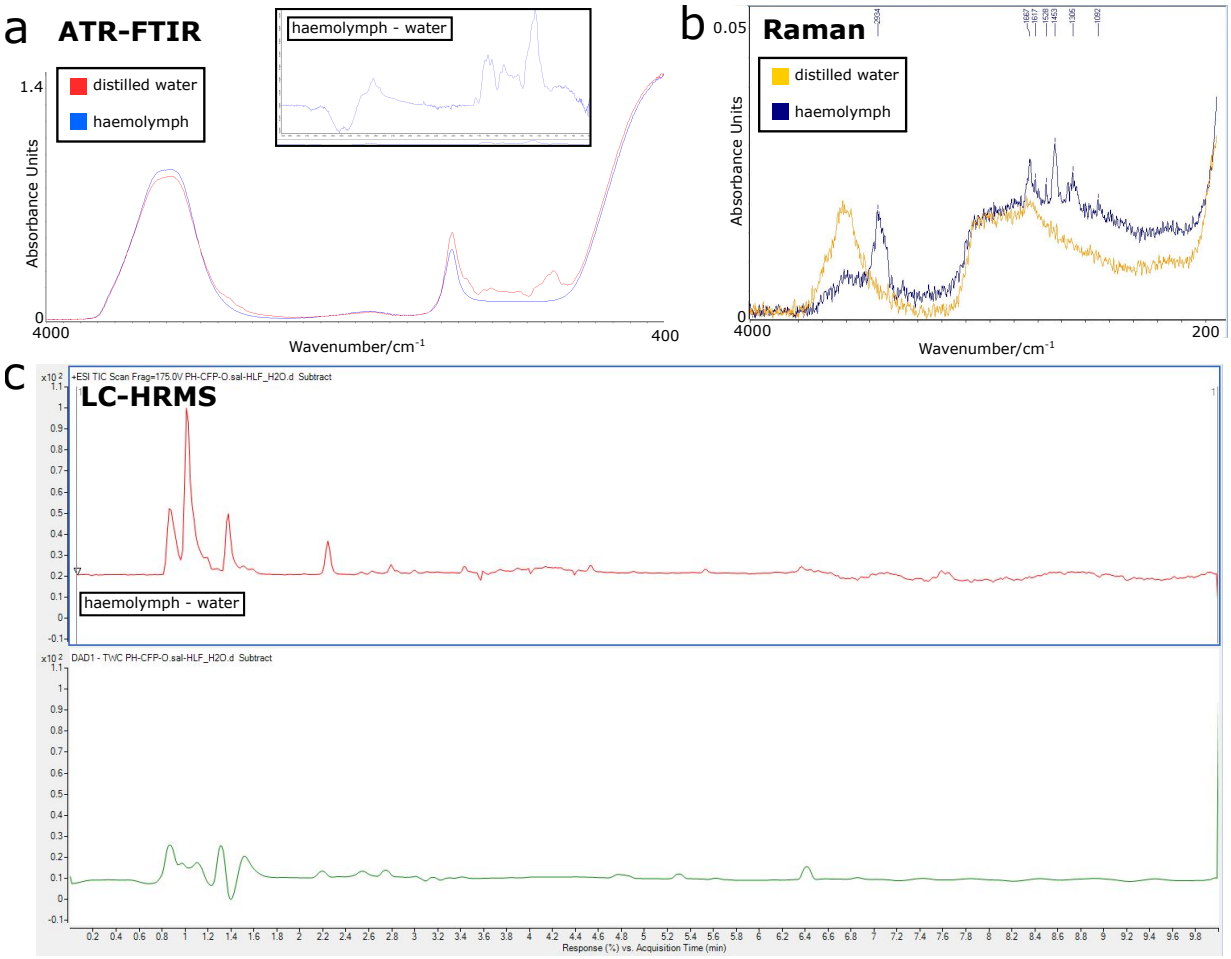

Figure 8.1: Haemolymph-analysis, a) ATR-FTIR, the inset shows the spectrum after subtraction of the signal for distilled water, b) IR-Raman, c) LC-HRMS

8.2 Chemical analysis of the lubricant of *Otiorhynchus salicicola*

The difficulty of obtaining a pure uncontaminated sample of the lubricant is a challenging problem. Due to the openness of the joint, the specimen will collect dust and dirt particles, which will mix with the lubricant. The same particles will lead to injuries and wear, resulting in cuticular wear debris within the joint. In injured beetles or opened joints, the haemolymph and other bodily fluids are almost indiscernible from the lubricant, further complicating the task. Furthermore, the limited quantities and quick evaporation of the lubricant pose more complex problems. Therefore, our efforts can be split in two parts: analyzing the lubricant directly in the system or extracting the lubricant immediately from the pores and analyzing it separately.

Since I did not want to overthink the task and exclude basic analysis methods, a first rudimentary analysis of an air-dried femur possibly including lubricant traces with the energy dispersive X-ray spectroscopy (EDX) system included in the SEM at IMT was conducted and

showed – as expected for a biological sample – a comprehensive occurrence of nitrogen (**N**), carbon (**C**) and oxygen (**O**). Unfortunately, the areas possibly including lubricant traces, did not differ from the rest of the femur.

Many methods are not suitable for the pursued analysis of the lubricant due to the amount needed for a successful analysis, i.e., nuclear magnetic resonance (NMR) needs at least one milliliter of sample material as communicated by the IMT specialists. I estimate a maximum volume of lubricant in the joints of a beetle in the dimension of femto- to picoliter. Other methods were not suitable because they require a vacuum, arising the need for dried samples. From the SEM analysis (see Sec. 4) of the drying of the samples, I learned, that the lubricant dries out and vanishes over time as can be seen under the SEM. Nevertheless, we analyzed a dried sample with the time-of-flight secondary ion mass spectrometry (TOF-SIMS), hoping for traces, which are possible to be analyzed, without any luck. The last point to consider is the spotsize of the method. The pores of the beetles have a diameter of approximately a micron and therefore the lubricant itself, which can be found in and around the samples, shows a spread of a few micrometers. This makes many methods, i.e., near ambient pressure X-ray photoelectron spectroscopy (NAP-XPS) with spotsizes in the range of half a millimeter or hundreds of micrometers or an increased depth unsuitable for an analysis. Keeping all of this in mind, I tried multiple methods.

For the lubricant which can be found on the frictional surface multiple methods were used in an attempt to analyze the lubricant. The Raman microscope showed the most potential with spotsizes in the same dimension as the pores. Unfortunately, the chitin around and below the lubricant showed a high auto-fluorescence making a separation of the signals impossible. This was not dependent on the wavelength as we have tried several commercially available systems. In order to get in closer contact with the lubricant, we tried AFM-IR. Unfortunately, in order to find the lubricant with the AFM we need to scan in tapping or contact mode and have not been able to find any lubricant in the found pores. I suspect, as is described in the brochures of the system, that the tip of the cantilever as well as the sample heats up under the IR-Laser, evaporating the lubricant and preventing me to find the lubricant while scanning.

For my second effort, I attempted to remove the lubricant from the joint in order to analyze it without interference. Due to the openness of the joint the simple process of flushing the lubricant out is not possible, in addition to the fact, that the solubility is unknown. The flushing of the joint would lead to a solution contaminated by particles from the environment as well as by the beetle's own materials for example haemolymph and chitin. I found two alleged solutions.

Since the joint is readily accessible with the AFM, the FluidFM was a suitable solution. The possibility of immersing the fresh joint in silicone oil allows for longer processing times and the hollow cantilever allows for scans to find the pores and precise injection and extraction. Unfortunately the system is designed for thin transparent biological samples and

mounted on an inverted microscope. Since the joints of beetles are not transparent, the included topview camera has to be used. Due to the limited resolution of the camera and distortion from the fluid a safe navigation of the challenging geometries of the beetle joint is impossible. After many unsuccessful attempts, this idea has been abandoned to prevent unnecessary risk of damaging the system.

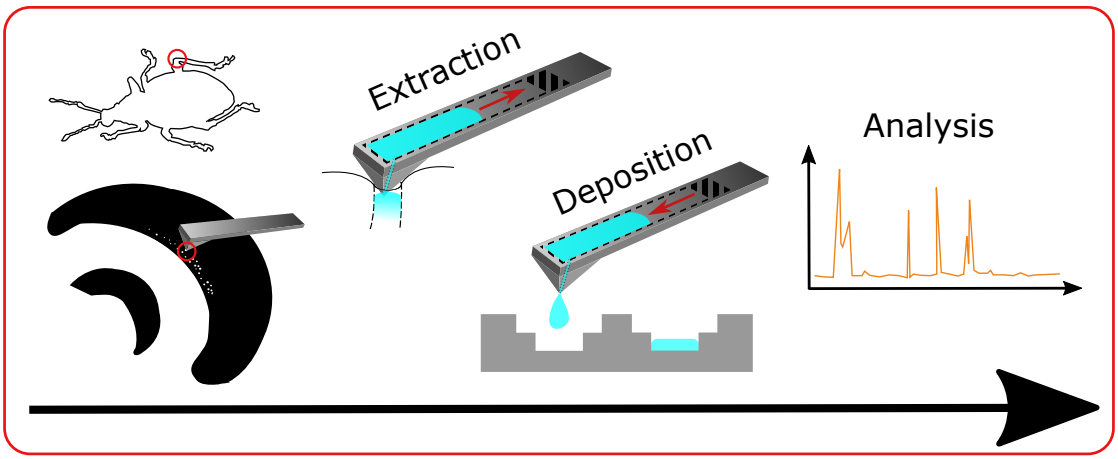

Figure 8.2: Flowchart FluidFM: Extraction of the lubricant with the hollow cantilever directly from the pores of the joint of the beetle before depositing the lubricant in 3D-printed containers to contain and locate them for the analysis methods

The second idea to obtain a pure sample of the lubricant is based on the assumption that the lubricant is water-based. This assumption rests upon the appearance of the lubricant in its fresh and dried state as observed with the SEM. The water inside the lubricant should expand upon freezing, pushing out from the pores as cylinders. The FIB system equipped with a cryo-stage as well as a nanomanipulator was our tool of choice in order to use this behavior to our advantage. Removing the frozen lubricant from the joint surface and transferring it onto a specified surface, the lubricant would be separated from the cuticular surface and pure, ready to be transported frozen to a Raman microscope for a subsequent analysis. Unfortunately, the untreated joint immediately charges up under the electron beam, not only distorting the image but also making it impossible to navigate with the nanomanipulator.

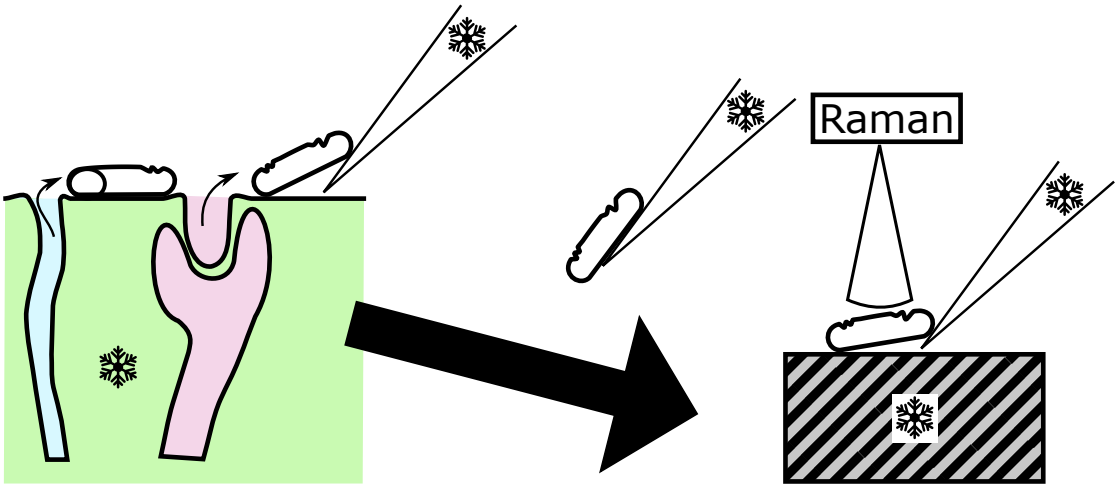

Figure 8.3: Flowchart Cryo-FIB: Extraction of the lubricant by freezing the joint, before manipulating the frozen lubricant with a cold nano-manipulator inside the FIB to transfer it to a frozen surface for a safe transport to the analysis system

First information towards the composition of the lubricant, excluding the obvious occurence of carbon (**C**), nitrogen (**N**), and oxygen (**O**), was obtained using the more sensitive EDX system integrated in the Environmental SEM, where cryogenically frozen fresh samples of dissected femurs were analyzed (with the kind help and support of Alexei Kiselev (KIT)). Areas of the frozen lubricant were compared to the frictional cuticular surface of the femur. In four scans (one representative scan is depicted in Fig. 8.4 a) and its EDX spectra in Fig. 8.4 b)) there was a clear increased amount of phosphor (**P**) and sodium (**Na**) and a slight increase compared to the cuticle in magnesium (**Mg**), sulfur (**S**), chloride (**Cl**) and kalium (**K**). Unfortunately in the scan executed in the area of the detached seta (see Fig. 8.4 c)) visible in Figure 4.5, this difference in composition of lubricant and cuticle is not given anymore. As can be seen in Figure 8.4 d) the spectra are almost identical to each other, with a slight increase in kalium for the lubricant and a surprising decrease in nitrogen.

Possible occurences of aluminium (**Al**) arises from the aluminium stub, of silver (**Ag**) from the silver lacquer used to fix the sample on the aluminium stub and of copper (**Cu**) and gold (**Au**) from the gold-platted copper mounting block. Even though metals have been found in the cuticle of arthropods, especially in intruding fortified organs like the ovipositor of a cicada or the stinger of a scorpion [99], I suspect, that the majority of the occurence of the metals is due to the preparation and not found directly in the cuticle in the area of the joint.

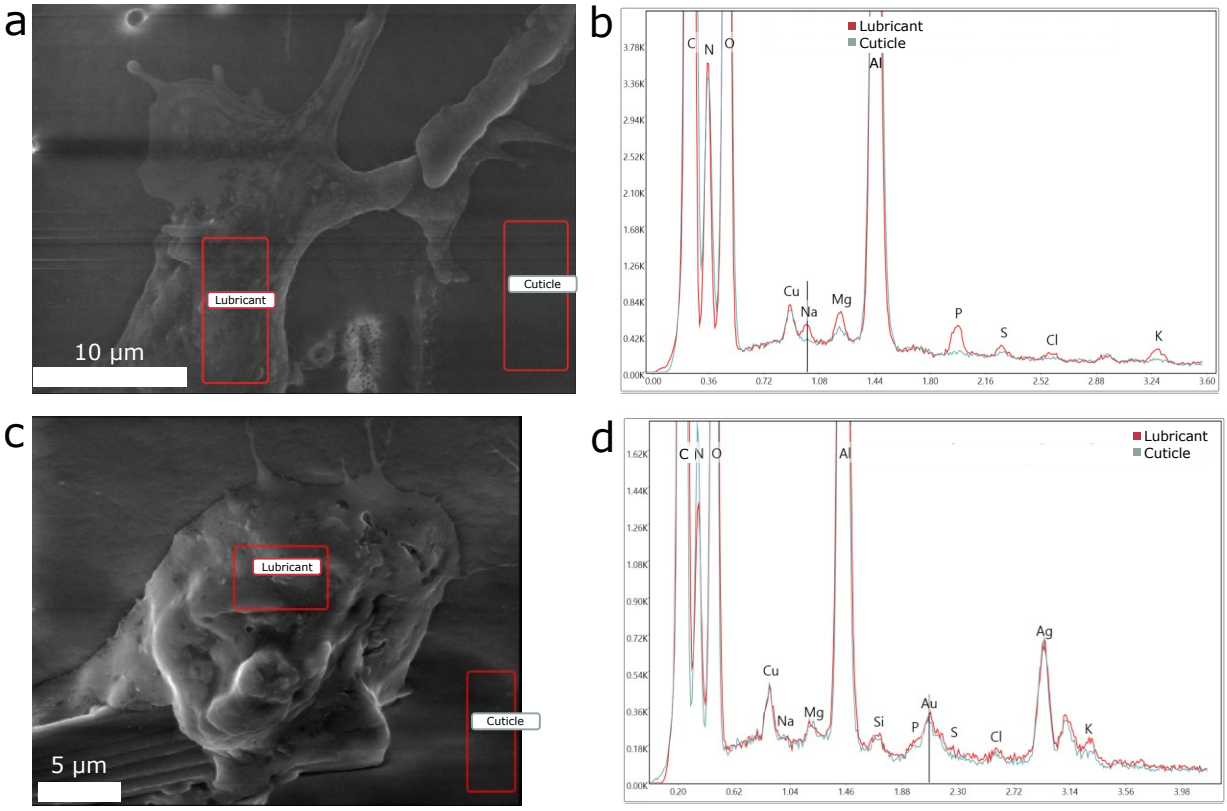

Figure 8.4: a) Area of interest as imaged with the ESEM, with the areas marked for the EDX analysis of the lubricant and cuticle composition. b) EDX spectra of the two areas marked in a) showing an increased occurence in sodium (**Na**), magnesium (**Mg**), phosphor (**P**), sulfur (**S**), chloride (**Cl**) and kalium (**K**) in the lubricant compared to the cuticle. This was observable for four different scans in a similar way. c) Area of interest as imaged with the ESEM, with the areas marked for the EDX analysis of the lubricant and cuticle composition. The overview of this area can be seen in Figure 4.5. d) EDX spectra of the two areas marked in c) showing no difference in sodium (**Na**), magnesium (**Mg**), phosphor (**P**), sulfur (**S**) and chloride (**Cl**) and only a slight increase in occurence in kalium (**K**) as well as a surprising decrease in nitrogen (**N**) in the lubricant compared to the cuticle.

The here summarized results and attempts imply on one hand a lubricant composition based on haemolymph, while the results obtained with the EDX of the frozen sample imply on the other hand, the possibilty of two different lubricants in the same joint with different purposes. Here the assumption would be, that one fluid is used to lubricate the frictional surfaces, while the other one is used to cover sharp edges to prevent extensive damage to the joint. The lubricant component of this system is possibly based on the haemolymph, while the protection might be more closely related to the waxes of the beetle. Unfortunately, this remains a mystery until further research is conducted.

9 Conclusion and Outlook

The aim of this thesis was to highlight a promising system for technological development inspired by nature. The joint of a beetle shows many similarities to technical joints and bearings and could – if understood completely – revolutionize the industry in its quest for a green future. The multitude of insects show the needed variety to have inspiration for nearly all known systems of humankind, laying groundwork in geometry, structuring, and lubrication. Since this topic is missing a basic understanding of the joint system in its morphological and tribological aspects, I do not complicate things with special geometries or properties and focus on a simple and common system of a limited number of individuals.

The femoro-tibial joint of the beetles *Coelorrhina aurata*, *Otiorhynchus sulcatus* and *Otiorhynchus salicicola* is a nearly symmetrical hinge joint. For *C. aurata* the lubricant extruding pores can be found on the tibia, while for the two *Otiorhynchini* species the pores can be mostly found on the femur. This is not the only surprising difference even though it might be connected: the two lubricants might be different. While the lubricant of *C. aurata* forms clumps and cylindrical structures, while also staying visually unchanged over different drying periods, the lubricant, which is formed by the pores of the *Otiorhynchini* seems to be covering the frictional surface in a thin layer and spreading evenly. Upon drying the lubricant forms a netlike structure before it wrinkles and vanishes as can be observed with the SEM. This process takes less than 48 hours. Understandably, different sizes of beetles need different lubricants since they are confronted with different challenges. Another explanation for this difference could be the inability of *O. sulcatus* and *salicicola* to fly compared to *C. aurata*.

The airdrying of the lubricant leads to different tribological behaviour. During my measurements with the AFM, I discovered that the lubricant of *C. aurata* shows almost no change in the coefficient of friction over the time of eleven months, while the coefficient of friction of the lubricant of *O. sulcatus* increases in just six months over a tenfold. In order to obtain these results, an intricate method of conducting the measurements in silicone oil, to prevent changes in the samples over the duration of the measurements, was developed. The lubricant was measured directly in the system, which allowed me to also measure and compare the coefficients of friction of the cuticular surface and the structures found on the frictional surfaces.

The microstructures found on the surface of the joint are based on sawtooth structures, reminiscent to the ones found in nature for example in snake- and sandfish-scales. This structure is well researched and is known to cause frictional anisotropy. Nevertheless, most of the microstructures found in the beetle's joints are decorated and formed in different ways in addition to the size being one dimension bigger than the sawtooth structures in snakes and sandfish. I therefore conducted a study working my way from a simple sawtooth structure with nanometer-high steps up to the simple shingle-like structure on 3D-printed models to prevent interference from the concave or convex surfaces on which the microstructures are

placed in the joints. Based on my findings, we can follow the path particles, trapped in the open joints of *O. sulcatus*, take to leave the joint, without harming the beetle. The structures might also spread and transport the lubricant from the pores over the whole frictional area. This is made possible by the volumetric scans with the μCT and the SEM images of the structures, showing the opposing structures and the direction of the structures, leading to a comprehensive understanding of the movement of the joints, particles and lubricant.

Expanding the data from the μCT with the nanoCT and FIB gives us a deeper insight into the network hidden below the frictional surfaces, supplying lubricant. I was able to find two different kind of pore canals with the nanoCT and FIB ending on the frictional surface. One of those is responsible for the extrusion of the lubricant in the relevant areas. Unfortunately, the purpose of the other pore canal as well as the assignment of the pore canals is still unknown. The pore canals connect to and thread through or along the haemocoel, respectively.

The last mystery to solve was the composition of the lubricant itself. Unfortunately despite my best efforts and multiple applied techniques, an analysis of the very limited material was not conclusive and will need further research. First measurements with an EDX system on a cryogenically frozen sample in an Environmental SEM hint at two different lubricants for different tasks further complicating this endeavor. This would fit well together with the discovery of two different kinds of pore canals, composing the lubricant supplying network.

While this work aimed for an improved complete understanding of the tribological system of the lubricated and structured femoro-tibial joint of the weevil *O. sulcatus*, each sucessful investigation posed more open questions. This shows the incredible complexity of natural systems and the associated research of these, where every carefully gained additional information is an essential step towards a thorough analysis.

This thesis only focused on one single joint of three beetles. With more joints in a leg, in a beetle, in beetles, in insects and a multitude of unused methods, a universe of new discoveries awaits.

Finally, I encourage biologists to not shy away from new technical engineering methods and engineers to take inspiration from existing solutions in nature. Interdisciplinarity is the key for a successful green future.

Acknowledgments

Thank you to my supervisor for all the freedom and letting me follow my wildest research dreams. This work wouldn't have been the same with you.

Thank you to Christian Greiner for sharing his team, instruments and scarf with me and for accompanying me to the end of my PhD as my Korreferent.

Thank you for Thomas van de Kamp to consult me throughout my PhD endeavors and to stand up for me, when I needed it most.

Thank you to the IPS/LAS family, who welcomed me warmly in their midst.

I want to thank Nikolay Zagainov, Stefan Hengsbach, Celine Deutschbein, Ajeya Simha, and Dario Mager for their help with 3D-printing in all its forms and glory.

I want to acknowledge my PhD colleagues Patrick Weiser, Patrick Schwaab, George Matthew, Hans Gunstheimer, Gowtham Arivanandhan, Roxane Lung, Ronja Pappenberger, Luisa Borgmann, Samaun Reza, Janes Oder, Jenny Hein and Max Kabbe, sometimes you just need to whine to others and let them whine back, to not feel all alone.

My deepest gratitude goes out to all the amazing colleagues, who where willing to hear me out, brainstorm with me, refer me to other colleagues, go beyond the limits of their instruments and simply give it a try. Without you and your openness I would have nothing to present. I am honored to work with such talented people and very privileged to get to know so many techniques. You are the reason that science and discovery is possible and humanity isn't lost in academia. Special thanks go out to Alexei Kiselev, Torsten Scherer, Matthias Mail, Michael Hirtz, Alexander Welle, Stefan Heissler, Krassimir Garbev, Patrick Hodapp, Alban Muslija, Julia Marzi, Reiner Mönig, and Rafaela Debastiani.

A big thank you to Richard Thelen, without you, I would have ended my PhD multiple times. Thank you for always encouraging us students.

I want to acknowledge the animal shelter "Tierheim Karlsruhe", without their amazing work and their amazing animals, with whom I had the opportunity and privilege to work with every weekend, I would have lost perspective. If you have the opportunity to donate your time or resources, I encourage you to do so and if you consider finding a friend for life, adopt one of their absolutely gorgeous and big hearted animals.

I want to acknowledge my family in Austria for letting me fly free. I know it was not easy to let me go for a more and more extended time. I am coming home soon.

Last but definitely not least, I want to thank my partner for allowing me to share this adventure with him.

List of Publications

Articles

Cornelia F. Pichler, Richard Thelen, Thomas van de Kamp, and Hendrik Hölscher. *Friction coefficient evolution of drying lubricant in the joints of beetles by friction force microscopy*. Tribology Letters, 73(1):1-10, 2025.

Cornelia F. Pichler, Rafaela Debastiani, Matthias Mail, Jenny Hein, Elias Hamann, Tilo Baumbach, Hendrik Hölscher, and Thomas van de Kamp. *Multimodal characterisation of the femorotibial joint of the black vine weevil (*Otiorhynchus sulcatus*)*. Journal of the Royal Society Interface, 2025. *Submitted*

Conference contributions

Cornelia F. Pichler, Richard Thelen, and Hendrik Hölscher. *Well lubricated in Nature – An Interplay of Structure and Lubricant in the Joints of Beetles*. Symposium Nano-BW 2022, Bad Herrenalb, Germany, December 5-7 2022. *Poster*

Cornelia F. Pichler, Richard Thelen, Thomas van de Kamp, and Hendrik Hölscher. *Screw like beetle joints and their tribological features*. DPG-Frühjahrstagung der Sektion Kondensierte Materie 2023, Dresden, Germany, March 26 - 31 2023. *Oral Presentation*

Cornelia F. Pichler, Richard Thelen, Matthias Mail, Thomas van de Kamp, and Hendrik Hölscher. *It just takes a little bit of elbow grease – Lubricants in the joints of beetles*. Symposium Nano-BW 2023, Bad Herrenalb, Germany, December 4-6 2023. *Poster*

Cornelia F. Pichler, Richard Thelen, Matthias Mail, Thomas van de Kamp, and Hendrik Hölscher. *Lubricants in the joints of beetles and their significance for biomimetics*. Global Young Scientists Summit 2024, Singapore, Singapore, January 8 - 13 2024. *Poster*

Cornelia F. Pichler, Richard Thelen, Matthias Mail, Thomas van de Kamp, Jenny Hein, and Hendrik Hölscher. *Well lubricated in Nature – An Interplay of Structure and Lubricant in Beetle Joints*. 5^{th} Young Researcher Meeting Morphology 2024, Darmstadt, Germany, February 22 - 24 2024. *Oral Presentation*

Weibin Wu, KM Samaun Reza, Patrick Weiser, Cornelia F. Pichler, Richard Thelen, and Hendrik Hölscher. *Anisotropic Friction of Snake Scales Analyzed by AFM – From Fundamentals to Applications*. 87. Jahrestagung der DPG und DPG-Frühjahrstagung der Sektion Kondensierte Materie, Berlin, Germany, March 17 - 22 2024. *Oral Presentation*

Cornelia F. Pichler, Richard Thelen, Matthias Mail, Thomas van de Kamp, and Hendrik Hölscher. *Well lubricated in Nature –An Interplay of Structure and Lubricant in Beetle Joints*. 87. Jahrestagung der DPG und DPG-Frühjahrstagung der Sektion Kondensierte Materie, Berlin, Germany, March 17 - 22 2024. *Oral Presentation*

Cornelia F. Pichler, Richard Thelen, Matthias Mail, Thomas van de Kamp, and Hendrik Hölscher. *Analyzing the tribological combination of microstructure and lubricant in beetle joints for the development of environmentally friendly lubricants*. The 1st International Online Conference on Biomimetics, Online, May 15-17 2024. *Poster*

Cornelia F. Pichler, Richard Thelen, Thomas van de Kamp, and Hendrik Hölscher. *Analyzing the tribological combination of microstructure and lubricant in beetle joints*. Gordon Research Seminar on Tribology, Lewiston, United States, June 22 - 23 2024. *Poster*

Cornelia F. Pichler, Richard Thelen, Thomas van de Kamp, and Hendrik Hölscher. *Analyzing the tribological combination of microstructure and lubricant in beetle joints*. Gordon Research Seminar and Conference on Tribology, Lewiston, United States, June 22 - 28 2024. *Poster*

Cornelia F. Pichler, Matthias Mail, Hendrik Hölscher, and Torsten Scherer. *Development of a cryo-workflow for the preparation of the lubricated hinge-joints of beetles and other intricate biological samples*. Microscopy Conference 2025, Karlsruhe, Germany, August 31 - September 4 2025. *Poster*

List of Figures

List of Tables

References

[1] Jeff Tollefson. Earth breaches 1.5° C climate limit for the first time: what does it mean? *Nature*, 637(8047):769–770, 2025.

[2] Emanuele Bevacqua, Carl-Friedrich Schleussner, and Jakob Zscheischler. A year above 1.5° C signals that Earth is most probably within the 20-year period that will reach the Paris Agreement limit. *Nature Climate Change*, 15(3):262–265, 2025.

[3] C. Mathew Mate. *Tribology on the Small Scale - A Bottom Up Approach to Friction, Lubrication, and Wear*. OUP Oxford, New York, London, 2008. ISBN 978-0-198-52678-0.

[4] Michael M. Khonsari and E. Richard Booser. *Applied Tribology - Bearing Design and Lubrication*. John Wiley & Sons, New York, 2017. ISBN 978-1-118-63724-1.

[5] Rafael Vazquez-Duhalt. Environmental impact of used motor oil. *Science of The Total Environment*, 79(1):1–23, 1989.

[6] Emmanuel O Aluyor and Mudiakeoghene Ori-Jesu. Biodegradation of mineral oils–A review. *African Journal of Biotechnology*, 8(6), 2009.

[7] Ivo Shodji Tamada, Paulo Renato Matos Lopes, Renato Nallin Montagnolli, and Ederio Dino Bidoia. Biodegradation and toxicological evaluation of lubricant oils. *Brazilian Archives of Biology and Technology*, 55:951–956, 2012.

[8] Kenneth Holmberg and Ali Erdemir. Influence of tribology on global energy consumption, costs and emissions. *Friction*, 5:263–284, 2017.

[9] Matthias Scherge and Stanislav S. N. Gorb. *Biological Micro- and Nanotribology - Nature's Solutions*. Springer Science & Business Media, Berlin Heidelberg, 2001. ISBN 978-3-662-04431-5.

[10] Werner Nachtigall. *Bionik als Wissenschaft - Erkennen - Abstrahieren - Umsetzen*. Springer-Verlag, Berlin Heidelberg New York, 2010. ISBN 978-3-642-10320-9.

[11] Zhongmin Jin and Duncan Dowson. Bio-friction. *Friction*, 1:100–113, 2013.

[12] Haoming An, Yubo Liu, Jiafeng Yi, Hongbin Xie, Chao Li, Xing Wang, and Wei Chai. Research progress of cartilage lubrication and biomimetic cartilage lubrication materials. *Frontiers in Bioengineering and Biotechnology*, 10:1012653, 2022.

[13] Y Merkher, S Sivan, I Etsion, A Maroudas, G Halperin, and A Yosef. A rational human joint friction test using a human cartilage-on-cartilage arrangement. *Tribology Letters*, 22:29–36, 2006.

[14] Nigel E Stork. How many species of insects and other terrestrial arthropods are there on Earth? *Annual Review of Entomology*, 63(2018):31–45, 2018.

[15] Konstantin Nadein and Stanislav Gorb. Principal design of the femoro-tibial joint in the main groups of arthropoda and possible implications for robotics limbs. *Zoomorphology*, 144(1):1–17, 2025.

[16] Malcolm Burrows and Gregory Sutton. Interacting gears synchronize propulsive leg movements in a jumping insect. *Science*, 341(6151):1254–1256, 2013.

[17] Thomas van de Kamp, Patrik Vagovič, Tilo Baumbach, and Alexander Riedel. A biological screw in a beetle's leg. *Science*, 333(6038):52–52, 2011.

[18] Konstantin Nadein, Alexander Kovalev, Jan Thøgersen, Tobias Weidner, and Stanislav Gorb. Insects use lubricants to minimize friction and wear in leg joints. *Proceedings of the Royal Society B*, 288(1954):20211065, 2021.

[19] Konstantin Nadein, Alexander Kovalev, and Stanislav N Gorb. Tribological properties of the beetle leg joints. *Friction*, 12(12):2791–2807, 2024.

[20] Thomas van de Kamp, Tomy dos Santos Rolo, Patrik Vagovič, Tilo Baumbach, and Alexander Riedel. Three-dimensional reconstructions come to life–interactive 3D PDF animations in functional morphology. *PLoS One*, 9(7):e102355, 2014.

[21] K Nadein and S Gorb. Lubrication in the joints of insects (arthropoda: Insecta). *Journal of Zoology*, 316(1):24–39, 2022.

[22] Konstantin Nadein and Stanislav N Gorb. Abrasive Wear in The Leg Joints of Insects. *Advanced Materials Interfaces*, 11(2):2300743, 2024.

[23] Konstantin Nadein and Stanislav Gorb. Smart joints: auto-cleaning mechanism in the legs of beetles. *Communications Biology*, 5(1):1030, 2022.

[24] Alexander E Filippov, Konstantin Nadein, Stanislav N Gorb, and Alexander Kovalev. Bio-bearings: Numerical Model of the Solid Lubricant in the Leg Joints of Insects. *Tribology Letters*, 72(1):11, 2024.

[25] Alexander E Filippov, Konstantin Nadein, Stanislav N Gorb, and Alexander Kovalev. Large-scale numerical simulation of the solid lubricant behavior in the leg joints of insects. *Advanced Theory and Simulations*, 7(6):2301236, 2024.

[26] Alexander E Filippov, Konstantin Nadein, Stanislav N Gorb, and Alexander Kovalev. Solid lubricant in the insect leg joints: Numerical simulation of tribological properties. *Advanced Theory and Simulations*, 7(7):2400348, 2024.

[27] Enrico Gnecco and Ernst Meyer. *Fundamentals of Friction and Wear on the Nanoscale -*. Springer Nature, Singapore, 2024. ISBN 978-3-031-63065-1.

[28] Valentin L. Popov. *Kontaktmechanik und Reibung - Von der Nanotribologie bis zur Erdbebendynamik*. Springer-Verlag, Berlin Heidelberg New York, 2016. ISBN 978-3-662-45975-1.

[29] Horst Czichos and Karl-Heinz Habig. *Tribologie-Handbuch - Tribometrie, Tribomaterialien, Tribotechnik*. Springer-Verlag, Berlin Heidelberg New York, 2015. ISBN 978-3-834-82236-9.

[30] Bharat Bhushan. *Nanotribology and Nanomechanics - An Introduction*. Springer, Berlin, Heidelberg, 2017. ISBN 978-3-319-51433-8.

[31] Wolfgang Demtröder. *Experimentalphysik 1 - Mechanik und Wärme*. Springer Berlin Heidelberg, Wiesbaden, 2021. ISBN 978-3-662-62727-3.

[32] Roy M. Mortier, Malcolm F. Fox, and Stefan Orszulik. *Chemistry and Technology of Lubricants*. Springer Science & Business Media, Berlin Heidelberg, 3 edition, 2010. ISBN 978-1-402-08662-5.

[33] Wesley C. Sanders. *Atomic Force Microscopy - Fundamental Concepts and Laboratory Investigations*. CRC Press, Boca Raton, Fla, 2019. ISBN 978-1-000-70794-6.

[34] Ernst Meyer, Roland Bennewitz, and Hans J. Hug. *Scanning Probe Microscopy - The Lab on a Tip*. Springer Nature, Singapore, 2021. ISBN 978-3-030-37089-3.

[35] V. J. Morris, A. R. Kirby, and A. P. Gunning. *Atomic Force Microscopy for Biologists -*. Imperial College Press, London, 2010. ISBN 978-1-848-16467-3.

[36] Bert Voigtländer. *Atomic Force Microscopy*. Springer, Berlin, Heidelberg, 2019. ISBN 978-3-030-13654-3.

[37] J. Paulo Davim. *Progress in Green Tribology - Green and Conventional Techniques*. Walter de Gruyter GmbH & Co KG, Berlin, 2017. ISBN 978-3-110-39252-4.

[38] Stanislav N Gorb and Elena V Gorb. Aquatic insects as a source for biomimetics. In *Aquatic Insects: Behavior and Ecology*, pages 401–426. Springer, 2019.

[39] Jun Kyun Oh, Spencer T Behmer, Richelle Marquess, Cengiz Yegin, Ethan A Scholar, and Mustafa Akbulut. Structural, tribological, and mechanical properties of the hind leg joint of a jumping insect: using katydids to inform bioinspired lubrication systems. *Acta Biomaterialia*, 62:284–292, 2017.

[40] M Sreejith, S Prashant, Sonu Benny, and TP Aneesh. Preparation of biological samples for SEM: Techniques and procedures. In *Microscopic Techniques for the Non-Expert*, pages 227–241. Springer, 2022.

[41] DF Ogletree, Robert W Carpick, and Miguel Salmeron. Calibration of frictional forces in atomic force microscopy. *Review of Scientific Instruments*, 67(9):3298–3306, 1996.

[42] M Varenberg, I Etsion, and G Halperin. An improved wedge calibration method for lateral force in atomic force microscopy. *Review of scientific instruments*, 74(7):3362–3367, 2003.

[43] Huabin Wang and Michelle L Gee. AFM lateral force calibration for an integrated probe using a calibration grating. *Ultramicroscopy*, 136:193–200, 2014.

[44] Martin Munz. Force calibration in lateral force microscopy: a review of the experimental methods. *Journal of Physics D: Applied Physics*, 43(6):063001, 2010.

[45] Evan V. Anderson, Saonti Chakraborty, Taylor Esformes, Derek Eggiman, Colin DeGraf, Keeley M. Stevens, Deli Liu, and Nancy A. Burnham. Shape-Independent Lateral Force Calibration. *ACS Applied Materials & Interfaces*, 3(9):3256–3260, 2011. PMID: 21854001.

[46] UD Schwarz, W Allers, G Gensterblum, and R Wiesendanger. Low-load friction behavior of epitaxial c 60 monolayers under Hertzian contact. *Physical Review B*, 52(20): 14976, 1995.

[47] M Enachescu, RJA Van Den Oetelaar, Robert W Carpick, DF Ogletree, CFJ Flipse, and Miguel Salmeron. Atomic force microscopy study of an ideally hard contact: the diamond (111)/tungsten carbide interface. *Physical Review Letters*, 81(9):1877, 1998.

[48] André Schirmeisen, Lars Jansen, Hendrik Hölscher, and Harald Fuchs. Temperature dependence of point contact friction on silicon. *Applied Physics Letters*, 88(12), 2006.

[49] Angelica Cecilia, Rolf Simon, Elias Hamann, Marcus Zuber, Tomáš Faragó, Daniel Haenschke, Mathias Hurst, Thomas van de Kamp, Sondes Bauer, Rebecca Spiecker, et al. The IMAGE beamline at the KIT Light Source. *Synchrotron Radiation*, 32(4), 2025.

[50] P.-A. Douissard, A. Cecilia, X. Rochet, X. Chapel, T. Martin, T. van de Kamp, L. Helfen, T. Baumbach, L. Luquot, X. Xiao, et al. A versatile indirect detector design for hard X-ray microimaging. *Journal of Instrumentation*, 7(09):P09016, 2012.

[51] Matthias Vogelgesang, Tomas Farago, Thilo F. Morgeneyer, Lukas Helfen, Tomy dos Santos Rolo, Anton Myagotin, and Tilo Baumbach. Real-time image-content-based beamline control for smart 4D X-ray imaging. *Journal of synchrotron radiation*, 23(5): 1254–1263, 2016.

[52] Matthias Vogelgesang, Suren Chilingaryan, Tomy dos Santos Rolo, and Andreas Kopmann. UFO: a scalable GPU-based image processing framework for on-line monitoring. In *2012 IEEE 14th International Conference on High Performance Computing and Communication & 2012 IEEE 9th International Conference on Embedded Software and Systems*, pages 824–829. IEEE, 2012.

[53] Tomáš Faragó, Petr Mikulík, Alexey Ershov, Matthias Vogelgesang, Daniel Hänschke, and Tilo Baumbach. Syris: a flexible and efficient framework for X-ray imaging experiments simulation. *Journal of Synchrotron Radiation*, 24(6):1283–1295, 2017.

[54] Rafaela Debastiani, Chantal Miriam Kurpiers, Enrico Domenico Lemma, Ben Breitung, Martin Bastmeyer, Ruth Schwaiger, and Peter Gumbsch. Dealing with missing angular sections in nanoCT reconstructions of low contrast polymeric samples employing a mechanical in situ loading stage. *Microscopy research and technique*, 88(3):832–838, 2025.

[55] Philipp D. Lösel, Thomas van de Kamp, Alejandra Jayme, Alexey Ershov, Tomáš Faragó, Olaf Pichler, Nicholas Tan Jerome, Narendar Aadepu, Sabine Bremer, Suren A Chilingaryan, et al. Introducing Biomedisa as an open-source online platform for biomedical image segmentation. *Nature Communications*, 11(1):5577, 2020.

[56] James Ahrens, Berk Geveci, and Charles Law. *ParaView: An End-User Tool for Large Data Visualization*, pages 717–731. Elsevier Inc., Burlington, MA, USA, 2005.

[57] Blender Online Community. *Blender - a 3D modelling and rendering package*. Blender Foundation, Stichting Blender Foundation, Amsterdam, 2018.

[58] Cornelia F Pichler, Richard Thelen, Thomas van de Kamp, and Hendrik Hölscher. Friction Coefficient Evolution of Drying Lubricant in the Joints of Beetles by Friction Force Microscopy. *Tribology Letters*, 73(1):1–10, 2025.

[59] RT Allen and GE Ball. Synopsis of Mexican taxa of the Loxandrus series (Coleoptera: Carabidae: Pterostichini). *Transactions of the American Entomological Society*, pages 481–575, 1979.

[60] Giuseppe Fusco, Carlo Brena, Alessandro Minelli, et al. Cellular processes in the growth of lithobiomorph centipedes (Chilopoda: Lithobiomorpha). A cuticular view. *Zoologischer Anzeiger*, 239(1):91–102, 2000.

[61] Frank-Thorsten Krell. Phylogenetic and taxonomic considerations on the variability of cuticular surface micromorphology within one species, Aphodius (Nialus) varians Duftschmid (Insecta: Coleoptera: Scarabaeidae: Aphodiinae). 1994.

[62] Alessandro Minelli, Diego Maruzzo, and Giuseppe Fusco. Multi-scale relationships between numbers and size in the evolution of arthropod body features. *Arthropod Structure & Development*, 39(6):468–477, 2010.

[63] Marco Moretto, Alessandro Minelli, and Giuseppe Fusco. Cell size versus body size in geophilomorph centipedes. *The Science of Nature*, 102:1–9, 2015.

[64] Anthony Charles Neville. *Biology of the arthropod cuticle*, volume 4. Springer Science & Business Media, 1975.

[65] Michael Schmitt. *Insektenwunderwelt - Einstieg in die Entomologie*. Springer Berlin Heidelberg, Wiesbaden, 2022. ISBN 978-3-662-64076-0.

[66] Michael Schmitt. The position of the Megalopodinae and Zeugophorinae in a phylogenetic system of the Chrysomeloidea (Insecta: Coleoptera). In *Proceedings of the third international symposium on the Chrysomelidae, Beijing*, pages 38–44, 1994.

[67] Thomas BH Schroeder, Jared Houghtaling, Bodo D Wilts, and Michael Mayer. It's not a bug, it's a feature: functional materials in insects. *Advanced Materials*, 30(19): 1705322, 2018.

[68] HE Hinton. Some structures of insects as seen with the scanning electron microscope. *Micron (1969)*, 1(2):84–108, 1969.

[69] Halvor T Tramsen, Stanislav N Gorb, Hao Zhang, Poramate Manoonpong, Zhendong Dai, and Lars Heepe. Inversion of friction anisotropy in a bio-inspired asymmetrically structured surface. *Journal of the Royal Society Interface*, 15(138):20170629, 2018.

[70] Gregory S Watson, Jolanta A Watson, and Bronwen W Cribb. Diversity of cuticular micro-and nanostructures on insects: properties, functions, and potential applications. *Annual Review of Entomology*, 62(1):185–205, 2017.

[71] Michael Schmitt. Stridulatory devices of leaf beetles (Chrysomelidae) and other Coleoptera. *Advances in Coleopterology*, pages 263–280, 1992.

[72] Michael Schmitt. Stridulaton in leaf beetles (Coleoptera, Chrysomelidae). In *Novel aspects of the biology of Chrysomelidae*, pages 319–325. Springer, 1994.

[73] Weibin Wu, Christian Lutz, Simon Mersch, Richard Thelen, Christian Greiner, Guillaume Gomard, and Hendrik Hölscher. Characterization of the microscopic tribological properties of sandfish (Scincus scincus) scales by atomic force microscopy. *Beilstein Journal of Nanotechnology*, 9(1):2618–2627, 2018.

[74] Weibin Wu, Shudong Yu, Paul Schreiber, Antje Dollmann, Christian Lutz, Guillaume Gomard, Christian Greiner, and Hendrik Hölscher. Variation of the frictional anisotropy on ventral scales of snakes caused by nanoscale steps. *Bioinspiration & Biomimetics*, 15 (5):056014, 2020.

[75] Alexander Filippov and Stanislav N Gorb. Frictional-anisotropy-based systems in biology: structural diversity and numerical model. *Scientific Reports*, 3(1):1240, 2013.

[76] Weibin Wu, Markus Guttmann, Marc Schneider, Richard Thelen, Matthias Worgull, Guillaume Gomard, and Hendrik Hölscher. Snake-Inspired, Nano-Stepped Surface with Tunable Frictional Anisotropy Made from a Shape-Memory Polymer for Unidirectional Transport of Microparticles. *Advanced Functional Materials*, 31(19):2009611, 2021.

[77] Christian Greiner and Michael Schäfer. Bio-inspired scale-like surface textures and their tribological properties. *Bioinspiration & Biomimetics*, 10(4):044001, 2015.

[78] Alexander E Filippov and Stanislav N Gorb. Modelling of the frictional behaviour of the snake skin covered by anisotropic surface nanostructures. *Scientific Reports*, 6(1): 23539, 2016.

[79] Neil F Hadley. The arthropod cuticle. *Scientific American*, 255(1):104–113, 1986.

[80] Charles Noirot and André Quennedey. Fine structure of insect epidermal glands. *Annual Review of Entomology*, 19(1):61–80, 1974.

[81] Imre Foldi. The wax glands in scale insects: comparative ultrastructure, secretion, function and evolution (Homoptera: Coccoidea). In *Annales de la Societe entomologique de France (NS)*, volume 27, pages 163–188. Taylor & Francis, 1991.

[82] Stephen P Foster and Jérôme Casas. How insect exocrine glands work. *Annual Review of Entomology*, 70, 2024.

[83] Stanislav N. Gorb. Porous channels in the cuticle of the head-arrester system in dragon/damselflies (Insecta: Odonata). *Microscopy Research and Technique*, 37(5-6): 583–591, 1997.

[84] Dan-Ting Li, Jian-Sheng Guo, Xin-Qiu Wang, Bernard Moussian, and Chuan-Xi Zhang. Three-dimensional reconstruction of pore canals in the cuticle of the brown planthopper. *Science China Life Sciences*, 64(11), 2021.

[85] Michael Locke. Pore canals and related structures in insect cuticle. *The Journal of Cell Biology*, 10(4):589–618, 1961.

[86] Donald Lococo and Erwin Huebner. The ultrastructure of the female accessory gland, the cement gland, in the insect Rhodnius prolixus. *Tissue and Cell*, 12(3):557–580, 1980.

[87] Sukhum Ruangchai, Christian Reisecker, Sabine Hild, and Andreas Ziegler. The architecture of the joint head cuticle and its transition to the arthrodial membrane in the terrestrial crustacean Porcellio scaber. *Journal of Structural Biology*, 182(1):22–35, 2013.

[88] Andy Sombke and Carsten HG Müller. When SEM becomes a deceptive tool of analysis: the unexpected discovery of epidermal glands with stalked ducts on the ultimate legs of geophilomorph centipedes. *Frontiers in Zoology*, 18:1–19, 2021.

[89] Kevin Halcrow. Modified pore canals in the cuticle of Gammarus (Crustacea: Amphipoda); a study by scanning and transmission electron microscopy. *Tissue and Cell*, 10(4):659–670, 1978.

[90] Jian-Sheng Guo, Xin-Qiu Wang, Dan-Ting Li, Dan-Dan Song, and Chuan-Xi Zhang. Three-dimensional architecture of a mechanoreceptor in the brown planthopper, Nilaparvata lugens, revealed by FIB-SEM. *Cell and Tissue Research*, 379:487–495, 2020.

[91] Rudolf Alexander Steinbrecht. Pore structures in insect olfactory sensilla: a review of data and concepts. *International Journal of Insect Morphology and Embryology*, 26 (3-4):229–245, 1997.

[92] Matthias Mail, Adrian Klein, Horst Bleckmann, Anke Schmitz, Torsten Scherer, Peter T. Rühr, Goran Lovric, Robin Fröhlingsdorf, Stanislav N. Gorb, and Wilhelm Barthlott. A new bioinspired method for pressure and flow sensing based on the underwater air-retaining surface of the backswimmer Notonecta. *Beilstein Journal of Nanotechnology*, 9:3039–3047, 2018.

[93] Mark W Westneat, Oliver Betz, Richard W Blob, Kamel Fezzaa, W James Cooper, and Wah-Keat Lee. Tracheal respiration in insects visualized with synchrotron X-ray imaging. *Science*, 299(5606):558–560, 2003.

[94] Mark Greco, Duncan Bell, Lewis Woolnough, Stephen Laycock, Nick Corps, David Mortimore, and Diana Hudson. 3-D visualisation, printing, and volume determination of the tracheal respiratory system in the adult desert locust, Schistocerca gregaria. *Entomologia Experimentalis et Applicata*, 152(1):42–51, 2014.

[95] Dariusz Iwan, Marcin Jan Kamiński, and Marcin Raś. The Last Breath: A μCT-based method for investigating the tracheal system in Hexapoda. *Arthropod Structure & Development*, 44(3):218–227, 2015.

[96] Philipp Lehmann, Marion Javal, Anton Du Plessis, and John S Terblanche. Using μct in live larvae of a large wood-boring beetle to study tracheal oxygen supply during development. *Journal of Insect Physiology*, 130:104199, 2021.

[97] Rajib Krishna Shaha, Jessica Ruth Vogt, Chung-Souk Han, and Michael E Dillon. A micro-CT approach for determination of insect respiratory volume. *Arthropod Structure & Development*, 42(5):437–442, 2013.

[98] Michal Knapp, Pavel Dobeš, Michal Řeřicha, and Pavel Hyršl. Puncture vs. reflex bleeding: Haemolymph composition reveals significant differences among ladybird species (Coleoptera: Coccinellidae), but not between sampling methods. *European Journal of Entomology*, 115, 2018.

[99] Matthew S. Lehnert. Invertebrates are heavy metal: An overview of armor, weapons, and other cuticular adaptations of diverse lineages. In Matthew S. Lehnert, editor, *Metals and their Functional Role in the Structures of Invertebrates*, pages 1–25. Springer International Publishing, Cham, 2024. ISBN 978-3-031-68486-9.